

Flight Controller Design for Quad Tilt Wing Ariel Vehicle Using Structured H_∞ Synthesis and Particle Swarm Optimization

by

Chiramathe NAMI
Student ID Number: 1188003

A dissertation submitted to the
Engineering Course, Department of Engineering,
Graduate School of Engineering,
Kochi University of Technology,
Kochi, Japan

in partial fulfillment of the requirements for the degree of
Doctor of Engineering

Assessment Committee:

Supervisor:	Koichi OKA
Co-Supervisor:	Akinori HARADA
Co-Supervisor:	Shuoyu WANG
Committee Member's Name:	Motomichi SONOBE
Committee Member's Name:	Masataka TAKAGI

March 2018

Abstract

Unmanned Aerial Vehicle (UAV) has gained much attention among researchers and widely researched since the last two decades. It is expected that the application of UAVs will keep expanding and the market grows dramatically within the decade. Existing fixed-wing and helicopter UAVs can be applied to meet the demands of these missions, However, these have inherent operational disadvantages. Fixed-wing UAVs generally offers good cruise performance but require runways or special launch and recovery equipment such as catapult launchers, parachutes or nets. Helicopter UAVs can take off and land without runways but have poor cruise and payload carrying performance compared to Fixed-wing UAVs. Vertical Takeoff and Landing (VTOL) UAVs are one means to overcome these disadvantages. They can take off and land without runways like a helicopter, and cruise at high speed like a fixed-wing vehicle.

In particular, Quad-Tilt-Wing Unmanned Aerial Vehicle (QTW-UAV), which contains a combination between VTOL in helicopter mode as well as high-speed cruise capabilities in Fixed-wing airplane mode, has particularly been considered. This is considered as a possible tool for numerous fields of applications, e.g. surveillance, monitoring and scientific measurement. Japan Aerospace Exploration Agency (JAXA) has thus designed and developed a series of QTW-UAVs (McART2, AKITSU, and McART3). The aircrafts contain the ability to tilt its wing starting from vertical to horizontal position. By rotating its tilt wings, the McART3 offers an ability to smoothly shift from vertical take-off to landing while the aircraft retains its flight attitude and satisfies the trim speed requirements. The preset tilt angles are commanded through a radio control transmission operated by ground pilot. The aircraft configurations are consisted of three major modes including helicopter, conversion and

airplane modes. Pitch and roll can be controlled in longitudinal and lateral-directional motion using CAS controller. In helicopter mode, pitching moment is generated by differential thrust between forward and aft propellers, rolling moment is generated by differential thrust between left and right propellers, and yawing moment is generated by aerodynamic forces on the flaperons due to propeller slipstream. In airplane mode, pitching moment is generated by deflections of forward and aft flaperons, rolling moment is generated by opposite deflections of left and right flaperons, and yawing moment is generated by the rudder and differential thrust between left and right propellers. During conversion between helicopter and airplane modes, interpolation between the helicopter and airplane control schemes. To verify the aircrafts feasibility, the flight test of AKITSU was conducted with practically sized QTW-UAV in outdoor environments. It successfully flied from helicopter mode to airplane mode, and vice versa; however, oscillatory motions were found in both longitudinal and lateral-directional motions. Likewise, for AKITSU; similar motions were found during the flight test of McART3. In particular, the oscillatory motion in the lateral-directional motions was sometimes large which increase pilot workloads to control the aircraft, and hence it should be suppressed for flight safety.

For this reason, on the one hand, this dissertation aims to tackle the previous drawbacks in McART3 flight controller design method. A design method with frequency domain constraints via reduced computational complexity for the optimization is proposed; that is, controller gains are designed by loop shaping technique within H_∞ framework, and Particle Swarm Optimization (PSO) method which is one of oriented search algorithms is used as an alternative to the brute-force method, i.e., gridding method, with small computational complexity. In particular, that PSO does not require the smoothness of the cost function with respect to design variables, nonlinear constraints, such as, admissible intervals for design variables, discontinuous cost functions, can be easily incorporated by defining modified cost

functions. PSO has been applied to various design problems, e.g., non-convex optimization problems, equality/ inequality constraints optimization problems, structured controller design problem.

On the other hand, in this research, QTW-UAV prototype is developed in both hardware as well as its unique flight firmware. In attempt to design the QTW-UAV. The airplane is able to tilt both wings from 0 to 90-degree tilt angles to operate in three different configuration modes, that is; airplane, helicopter and transition modes. The aircraft parts are particularly design to meets the specific aircraft requirements. Size of the aircraft is decided by the limited length of the wind tunnel cross section area. Such that, the wing span is designed within those ranges. Therefore, the front wing span is design to be 800 mm. and the rare wing is design to be 840 mm as a canard configuration. The weight of the aircraft is approximately 6.5 kg. The propulsion system uses four high power electric motors. The flight control frameworks are designed based on the requirements of multitasking inflight process. The designed firmware is divided into four major parts; ground station, central flight controller, mechanism driver and actuators. In ground control part, two modes are available for pilot to control the airplane. i.e., direct input keyboard using Wi-Fi or long-range remote controller using radio frequency modes. The signal form ground station is sent to onboard central flight control unit. In particular, in QTW-UAV control, flaps and motors are required to separately operate in real-time as much as they can. Therefore, kernel based Operating System (OS) is required for multi-tasking process. The central flight control received commands from pilot and calculate the different flight operating condition for each actuator.

This dissertation consists of six chapters as follows;

Chapter 1 offers a short introduction to UAV, QTW-UAV and McART3 QTW-UAV which is used as a based model in this research. The next section, research problem and

hypothesis, covers an existing CAS controller problems. Last the research objective is given as the strategy to solve those previous CAS controllers designed drawbacks.

Chapter 2 provides McART3 dynamical model configuration in both longitudinal as well as lateral-directional motions. In particular, CAS controller is given as a fixed-structure controller consists of only two control gains (proportional and integral gains). Hence, the derivation of McART3 model with fixed-structured controller framework is demonstrated. The next section covers fundamental theories regarding to H_∞ control combines with weighted sensitivity function with classical loop shaping technique. Last, Particle Swarm Optimization (PSO) is derived as an optimizer for proposed CAS controller design.

Chapter 3 proposes a method for CAS design in nominal model with the application of PSO. To address the drawbacks in existing design methods for Quad Tilt Wing Unmanned Aerial Vehicle (QTW- UAV), i.e., oscillatory motions and a large numerical complexity in controller gain design. Alternative design requirements are given in frequency domain which is different from existing controller design as the previously published reports from JAXA. Weighted sensitivity function from attitude command to attitude error is demanded to satisfy an H_∞ norm constraint. The applicability of proposed method is verified by CAS design for McART3 in which the target sensitivity function is given by using the gains in an existing paper. Then, as an extension, we address oscillatory suppressing CAS design. In exchange for slightly slow responses, oscillatory sup-pressing CAS gains are obtained in the latter problem.

Chapter 4 complements Chapter 3. The proposed design CAS gains are enhanced to satisfy the robust performance. To realize robust control performance of the design CAS gains against possible plant modeling errors, “multiple models approach” is applied as the same manner as the previously published reports from JAXA; however, in contrast to the previously used method, this chapter has two main contributions. The applicability of our method is first

confirmed by designing common CAS gains which guarantee the robust performances of all candidate models, CAS gains that suppress oscillatory motions, which is one of the drawbacks of the previously designed CAS gains, are designed using the proposed method. The applicability of the designed CAS gains is examined by faithful nonlinear flight simulations under no gust and wind gust conditions. It is confirmed that the designed CAS gains worked well throughout the flight simulation. McART3 can fly safely in helicopter mode, airplane mode, and transition in nominal conditions as well as slightly off-nominal conditions. In particular, roll angle faithfully follows their commands in all tilt angles which represent good tracking performance in both with and without wind gust conditions. The oscillations motions are barely found in roll angles as expected and slightly slow responses are apparently found. This confirms the applicability of our designed gains which are consistent. In addition, the improvement of the performance of nominal models are further investigated when the probability density functions for the nominal models and the perturbed models are given a priori and the latter is less than the former.

Chapter 5 demonstrate the QTW-UAV prototype. In attempt to construct QTW-UAV, the overall aircraft design process is firstly implement through series of simulations e.g. airfoil, wings, fuselage, rudder, tilting mechanism. Next section covers overall manufacturing as well as aircraft assembling process. The flight control unit are developed through raspberry PI with C++ programing language. Furthermore, full system flight test is conducted in order to verify the aircraft feasibility.

Acknowledgements

First of all, the author is most grateful to Prof. Kochi Oka for his assistances and encouragements during the study. Appreciation and deepest gratitude for the help and support are extended to following persons;

Prof Akinori Harada. for his sharing knowledge, suggestion in this work and remarkable inspiration.

Masayuki Sato for many academic, professional commitments and research supports. His wisdom, knowledge and commitment to the highest standard inspired and motivate me.

Prof. Toshiharu Sugie for his sharing knowledge, comprehensive advice until this work came to existence.

I would like to acknowledge the people who mean world to me, my parent for showing faith in me and giving me liberty to choose what I desired. I consider myself the luckiest in the world to have such a supportive family, standing behind me with their love and support.

Mr. Bundhit Suksiri, my youngest brother, for the work presented in this thesis. His motivation and support drive me to give my best. I take this opportunity to acknowledge him for encouraging me to discover the magic world of elegance coding as well as being my first instructor on UNIX operating system.

All Thai peoples in Kochi for their immeasurable goodwill.

All mechanical and aerospace control systems laboratory members for their useful technical knowledge.

Finally, the author is also thankful to Kochi University of Technology for a great opportunity of Master course program and especially financial supports.

Table of Contents

	Pages
Title Page	i
Abstract	ii
Acknowledgements	vii
Table of Contents	ix
Lists of Figures	xii
Lists of Tables	xvii
Chapter 1 Introduction	1
Chapter Overview	1
1.1. UAV	1
1.2. McART3 QTW-UAV	4
1.3. Research Problem and Hypothesis	6
1.4. Research Objective	8
1.5. References	8
Chapter 2 Background	9
Chapter Overview	9
2.1. McART3 configurations	9
2.2. McART3 with fixed-structure controller framework	13
2.3. H_∞ Control via loop shaping	17
2.3.1. H_∞ Terms	17
2.3.2. Weighted sensitivity	18
2.4. Particle Swarm Optimization	20
2.5. References	24

Chapter 3 H_∞ Control Based CAS Design of QTW-UAV Using Particle Swarm Optimization **25**

Chapter Overview	25
3.1. Chapter Introduction	25
3.2. Design Problem and Method	27
3.2.1. Loop-shaping technique	27
3.2.2. Particle swarm optimization	28
3.3. Results	28
3.3.1. Basic design	29
3.3.2. Extension to oscillatory suppressing CAS	29
3.4. Chapter summary	34
3.5. References	34

Chapter 4 H_∞ Control Based CAS Design for QTW-UAV via Multiple Model Approach with Particle Swarm Optimization **36**

Chapter Overview	36
4.1. Chapter Introduction	37
4.2. Design Problem and Method	40
4.2.1. Loop-shaping Technique	43
4.2.2. Particle swarm optimization	43
4.3. Results	44
4.3.1. Basic design (Robust CAS gains design)	44
4.3.2. Extension to oscillatory suppressing CAS	45
4.3.3. Extension to parametric study for control improvement when the probability function is given	46
4.3.4. Nonlinear Flight Simulation	54
4.4. Chapter summary	57
4.5. References	58

Chapter 5 Hardware Implementation **59**

Chapter Overview	59
5.1. Structure design process	60

5.1.1. Airfoils design	61
5.1.2. Wing structure design	63
5.1.3. Plain flap	64
5.1.4. Vertical tail design (Rudder)	64
5.1.5. Fuselage and Gearboxes design	65
5.1.6. Engines	67
5.2. Manufacturing process	68
5.2.1. Mold making for control surface	68
5.2.2. Control surface using carbon-fiber	69
5.3. Flight control design process and firmware design strategy	72
5.3.1. Flight control implementation	73
Chapter 6 Conclusion	77
List of Publications	79
APPENDIX A	81
APPENDIX B	95

Lists of Figures

	Pages
Fig. 1.1. Fixed-wing UAV1.1) (RQ-2B Pioneer).	2
Fig. 1.2. Boeing Q-18 Hummingbird ^{1.6)} .	3
Fig. 1.3. QTW-UAV flying profile ^{1.7)} .	3
Fig. 1.4. McART3 QTW VTOL prototype ^{1.8)} .	5
Fig. 1.5. The longitudinal motion control block diagram.	5
Fig. 1.6 Time history of McART3 full flight with JAXA flight controller	7
Fig. 2.1. The longitudinal motion control block diagram. ^{2.2)}	11
Fig. 2.2. The lateral-directional motion control block diagram. ^{2.2)}	11
Fig. 2.3. SISO Closed-loop system with SAS integrated.	13
Fig. 2.4. Generalized system framework for tuning fixed control structures.	14
Fig. 2.5. Linear fractional model system.	15
Fig. 2.6. General block diagram for analysis with no uncertainty.	16
Fig. 2.7. Case where $ S(s) $ exceed its bound $1/ W(s) $ resulting in $\ WS\ _{\infty} > 1$.	19
Fig. 2.8. Inverse of performance weight. Exact and asymptotic plot of $1/ W(s) $.	20
Fig. 2.9. Three fundamental elements for the PSO calculations	22
Fig. 3.1. Block diagram for fixed structured CAS in H_{∞} framework.	27
Fig. 3.2. Gain plots of sensitivity functions with CAS gains in 3.6), optimized gains in Table 3.1 (a) and (b), and $1/ W(s) $ (Close-loop figures at max peak gains are given in the boxes.) (a) $\tau_{\omega} = 15^{\circ}$ [lon. motion] (b) $\tau_{\omega} = 15^{\circ}$ [lat.-dir. motion].	32

Fig. 3.3. Gain plots of sensitivity functions with CAS gains in 3.6), optimized gains in Table 3.1 (c), and $1/ W(s) $ (Close-look figures around max peak gains are given in the boxes.) (a) $\tau_\omega = 15^\circ$ and (b) $\tau_\omega = 30^\circ$ [lat.-dir. motions].	33
Fig. 3.4. Step responses of ϕ at (a) $\tau_\omega = 15^\circ$ and (b) $\tau_\omega = 30^\circ$.	33
Fig. 4.1. Block diagram for robust fixed structured CAS in H_∞ framework.	40
Fig. 4.2. Gain plots of sensitivity functions with CAS gains in 4.6), optimized gains in Table 4.2 (a) and (b), and $1/ W(s) $ (Close-look are given in the boxes.) (a) $\tau_\omega = 30^\circ$ [lon. motion] (b) $\tau_\omega = 30^\circ$ [lat.-dir. motion].	51
Fig. 4.3. Gain plots of sensitivity functions with CAS gains in 4.6), optimized gains in Table 4.2 (c), and $1/ W(s) $ (Close-look figures around max peak gains are given in the boxes.) (a) $\tau_\omega = 30^\circ$ and (b) $\tau_\omega = 50^\circ$ [lat.-dir. motions].	52
Fig. 4.4. Step responses of using oscillatory suppression CAS gains in Table 4.2(c) at (a) $\tau_\omega = 30^\circ$ and (b) $\tau_\omega = 50^\circ$ [lat.-dir. motions].	53
Fig. 4.5. Step responses at clean configuration using CAS gains from parametric study in table 4.4 [lat.-dir. motions].	53
Fig. 4.6. Time history of full conversion flight under normal condition.	55
Fig. 4.7. Time history of full conversion flight under wind gust condition.	56
Fig. 5.1. QTW-UAV design prototype.	59
Fig. 5.2. QTW-UAV design (top-view).	60
Fig. 5.3. QTW-UAV design (side-view).	61
Fig. 5.4. NACA 0008 polar coordinate at $Re = 500,000$.	62
Fig. 5.5. Airfoil profile of NACA 0008 with Reynold number equal to 500,000.	62
Fig. 5.6. Wing design.	63
Fig. 5.7. Wing design.	65
Fig. 5.8. Vertical tail design.	65

Fig. 5.9. Fuselage and tilting mechanism design.	66
Fig. 5.10. Fuselage and tilting mechanism design.	67
Fig. 5.11. Engines and propellers.	68
Fig. 5.12. Mold making for surface design using 3D-printer.	69
Fig. 5.13. Carbon fiber surface manufacturing.	70
Fig. 5.14. Surface weight comparison.	71
Fig. 5.15. 3D printer parts.	71
Fig. 5.16. Final QTW-UAV porotype.	72
Fig. 5.17. QTW-UAV control schematic.	73
Fig. 5.18. RPI-3 schematic diagram.	74
Fig. 5.19. MPU6050 schematic diagram.	75
Fig. 5.20. RPI-3 and PCA 9685 schematic diagram.	76
Fig. 7.2. Step responses of θ with CAS gains in 3.6), optimized gains in Table 3.1(a) at $\tau_\omega = \text{cln [lon. motion]}$.	82
Fig. 7.4. Step responses of θ with CAS gains in 3.6), optimized gains in Table 3.1(a) at $\tau_\omega = 0^\circ$ [lon. motion].	83
Fig. 7.6. Step responses of θ with CAS gains in 3.6), optimized gains in Table 3.1 (a) at $\tau_\omega = 15^\circ$ [lon. motion].	84
Fig. 7.8. Step responses of θ with CAS gains in 3.6), optimized gains in Table 3.1 (a) at $\tau_\omega = 30^\circ$ [lon. motion].	85
Fig. 7.10. Step responses of θ with CAS gains in 3.6), optimized gains in Table 3.1 (a) at $\tau_\omega = 50^\circ$ [lon. motion].	86
Fig. 7.12. Step responses of θ with CAS gains in 3.6), optimized gains in Table 3.1 (a) at $\tau_\omega = 70^\circ$ [lon. motion].	87

Fig. 7.14. Step responses of ϕ with CAS gains in 3.6), optimized gains in Table 3.1 (b) at $\tau_\omega =$ cln [lat. motion].	88
Fig. 7.18. Step responses of ϕ with CAS gains in 3.6), optimized gains in Table 3.1 (b) at $\tau_\omega =$ 15° [lat. motion].	90
Fig. 7.20. Step responses of ϕ with CAS gains in 3.6), optimized gains in Table 3.1 (b) at $\tau_\omega =$ 30° [lat. motion].	91
Fig. 7.22. Step responses of ϕ with CAS gains in 3.6), optimized gains in Table 3.1 (b) at $\tau_\omega =$ 50° [lat. motion].	92
Fig. 7.24. Step responses of ϕ with CAS gains in 3.6), optimized gains in Table 3.1 (b) at $\tau_\omega =$ 70° [lat. motion].	93
Fig. 7.26. Step responses of ϕ with CAS gains in 3.6), optimized gains in Table 3.1 (b) at $\tau_\omega =$ 90° [lat. motion].	94
Fig. 7.28. Step responses of ϕ with CAS gains in 4.6), optimized gains in Table 4.2 (c) at $\tau_\omega =$ cln [lat. motion].	96
Fig. 7.30. Step responses of ϕ with CAS gains in 4.6), optimized gains in Table 4.2 (c) at $\tau_\omega =$ 0° [lat. motion].	97
Fig. 7.32. Step responses of ϕ with CAS gains in 4.6), optimized gains in Table 4.2 (c) at $\tau_\omega =$ 15° [lat. motion].	98
Fig. 7.34. Step responses of ϕ with CAS gains in 4.6), optimized gains in Table 4.2 (c) at $\tau_\omega =$ 30° [lat. motion].	99
Fig. 7.36. Step responses of ϕ with CAS gains in 4.6), optimized gains in Table 4.2 (c) at $\tau_\omega =$ 50° [lat. motion].	100
Fig. 7.38. Step responses of ϕ with CAS gains in 4.6), optimized gains in Table 4.2 (c) at $\tau_\omega =$ 70° [lat. motion].	101

Fig. 7.40. Step responses of ϕ with CAS gains in 4.6), optimized gains in Table 4.2 (c) at $\tau_\omega = 90^\circ$ [lat. motion].

102

Lists of Tables

	Pages
Table 1.1. QTW-UAV control configuration. ^{1.9)}	6
Table 2.1. McART3 flight parameters of Longitudinal motions ^{2.2)}	12
Table 2.2. McART3 flight parameters of lateral - directional motion ^{2.2)}	12
Table 2.3. The usage of McART3 feedback gains ^{2.2)} (“x” denotes use, “-”denotes disuse)	12
Table 2.4. The optimization results of SAS gains in longitudinal motions ^{2.2)} (“-” denotes disuse)	12
Table 2.5. Optimization results of SAS gains in lateral-directional motions ^{2.2)} (“-” denotes disuse)	12
Table 3.1. (a) Admissible CAS gain regions, CAS gains in 3.6), and optimized CAS controller gains using our method. [Basic design - longitudinal motion]	31
Table 3.1. (b) Admissible CAS gain regions, CAS gains in 3.6), and optimized CAS controller gains using our method. [Basic design - longitudinal motion]	31
Table 3.1. (c) Admissible CAS gain regions, CAS gains in 3.6), and optimized CAS controller gains using our method. [Extension design - lateral directional motion]	32
Table 4.1. McART3 nominal and the perturbed models represent the supposed plants modeling errors in 4.6)	41
Table 4.2. (a) Admissible CAS gain regions, CAS gains in 4.6), and optimized CAS controller gains using our method. [Basic design - lateral directional motion]	48
Table 4.2. (b) Admissible CAS gain regions, CAS gains in 4.6), and optimized CAS controller gains using our method. [Basic design - lateral directional motion]	48

Table 4.2. (c) Admissible CAS gain regions, CAS gains in 4.6), and optimized CAS controller gains using our method. [Extension design - lateral directional motion]	49
Table 4.3. McART3 given probability coefficients for parametric study	49
Table 4.4. CAS controller improvement using probability density coefficients	50

Chapter 1

Introduction

Chapter Overview

This chapter begins with a general overview of Unman Ariel Vehicle (UAV), Quad-Tilt-Wing Unmanned-Ariel-Vehicle (QTW-UAV) and McART3 QTW-UAV developed by Japanese Aerospace Exploration Agency (JAXA) which is used as a based model in this research. The next section, research problem and hypothesis, covers an existing problem in flight controller design. Last, research objective is clarified as a goal of this research.

1.1. UAV

Applications of the Unmanned Aerial Vehicle (UAV) are becoming popular based on rapid technological advances and growth in operational experience^{1.1-1.5}. Potential civil and commercial UAV applications include scientific research such as meteorology and earth science, environmental observation such as air sampling, vegetation survey, and wildlife tracking, law enforcement, disaster support, and industrial support such as crop dusting, fish finding and power line maintenance. Indeed, several UAVs have already been applied to border patrol, forest fire mapping and so on. It is expected that the application of UAVs will keep expanding and the market will grow dramatically within the decade. Existing fixed-wing and helicopter UAVs can be applied to meet the demands of these missions, but these have inherent operational disadvantages. Fixed-wing UAVs generally offers good cruise performance but require runways or special launch and recovery equipment such as catapult launchers,

parachutes or nets. Helicopter UAVs can take off and land without runways but have poor cruise and payload carrying performance compared to fixed-wing UAVs. Vertical Takeoff and Landing (VTOL) UAVs are one means to overcome these disadvantages. They can take off and land without runways like a helicopter, and cruise at high speed like a fixed-wing vehicle. Of the VTOL configurations, solution. With these considerations, the Japan Aerospace Exploration Agency (JAXA) has been developing a QTW VTOL UAV^{1.7)} as one of its research programs aimed at extending civil UAV operational capabilities and applications. The concept of the proposed QTW-UAV is shown in figure 1.3 to demonstrated in-flight configuration.



Fig. 1.1. Fixed-wing UAV1.1) (RQ-2B Pioneer).



Fig. 1.2. Boeing Q-18 Hummingbird^{1.6)}.

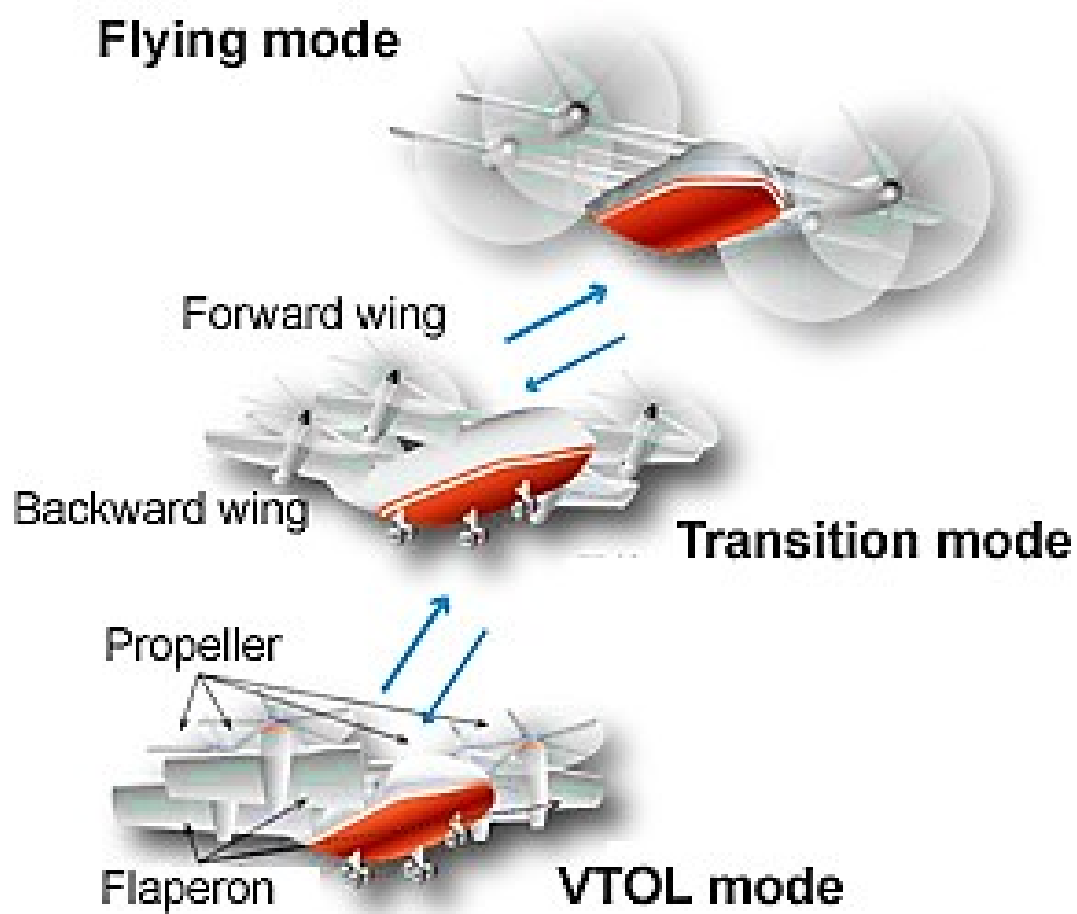


Fig. 1.3. QTW-UAV flying profile^{1.7)}.

1.2. McART3 QTW-UAV

This research employed one of JAXA QTW-UAVs name as McART3 as shown in Figure 1.4^{1,8)}. The dimension of the model has 1.1 m. length, width of 1.4 m, and weight of 4.6 kg. The vehicle takes off in VTOL mode with the leading edges of its wings directed vertically upwards. The vehicle climbs and then accelerates while rotating its wing gradually towards the horizontal. This flight phase is termed “accelerating transition” and the vehicle’s configuration during transition is said to be in a “conversion mode”. The McART3 cruises in “airplane mode” with the main wings fixed horizontally at a down stop. In the “decelerating transition” phase, the wings tilt back to the vertical, and the vehicle finally lands in VTOL mode. In the hover, the vehicle is controlled in pitch and roll via differential thrust. Yaw is controlled via flaperons surfaces on the front and rear main wings which are immersed in the propeller slipstream. In airplane mode, the vehicle is controlled in pitch via elevators (or flaperons), in roll via flaperons and in yaw via a rudder or differential thrust. Figure 1.5 illustrates the flight configuration for vertical take-off to landing of McART3. Based on the tandem wing configuration design, a prototype vehicle was constructed taking advantage of current RC technologies. Tilt units on the main wings driven by RC servo motors allowed the tilt angle to be varied between zero and 90 degrees. The vehicle was powered by four electric motors driving fixed pitch propellers. Actuators were provided for power control, the flaperons, elevator, rudder control surfaces, wing tilt angle, and nose wheel steering. A thrust mixing computer was developed to generate power command outputs to each motor by mixing average power and differential pitch and roll power-command inputs from the pilot through a radio remote control system. Table 1.1 shows the McART3 control configuration in longitudinal as well as lateral-directional motion.



Fig. 1.4. McART3 QTW VTOL prototype^{1,8)}.

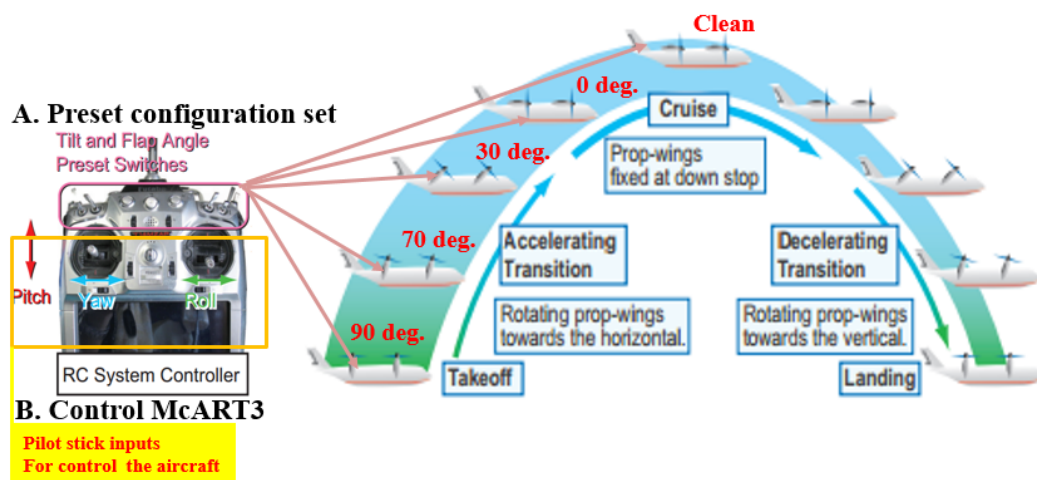
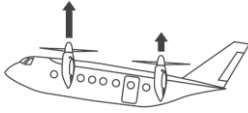
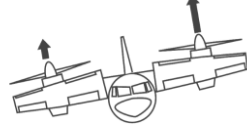
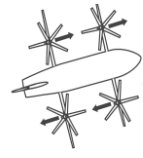
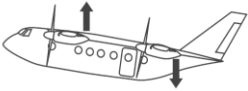

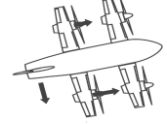


Fig. 1.5. The longitudinal motion control block diagram.

Table 1.1. QTW-UAV control configuration.^{1.9)}

	Pitch control	Roll control	Yaw control
Helicopter mode (vertical take-off and landing)	Differential thrust between fore/aft propellers 	Differential thrust between left/right propellers 	Flaperons (Propeller slipstream) 
Conversion mode	Combination of helicopter and airplane modes		
Airplane mode (level flight)	Flaperons 	Flaperons 	Differential thrust between left/right Propellers (Power rudder) 

1.3. Research Problem and Hypothesis

To clarify this drawback, JAXA McART3 flight result is shown in Fig. 1.6 This indicates that some oscillatory motions are found in roll control and pitch control. In particular, roll oscillations appear from 60[s] to 70[s] at wing tilt angle of 30-15[deg], and from 160[s] to 190[s] at wing tilt angle of 15-50[deg]. It should be suppressed for flight safety.

In the existing design, JAXA McART3 CAS controllers were optimized by using gridding algorithm approach. The optimized CAS controller gains were demanded to minimize the time responses of McART3 in each tilt angle configuration. The cost function $f_{cost}(\mathbf{k})$ is set in Eq.(1) as follows^{1.9)}:

$$f_{cost}(\mathbf{k}) = \int_0^{T_{eval}} (x_{com} - x)^2 dt \quad (1.1)$$

where x denotes the attitude angles (pitch and roll angles, respectively, for the longitudinal and lateral-directional motion), x_{com} denotes their commands given as step inputs,

and T_{eval} [s.] denotes a priori defined evaluation time. However, the problem of the optimized CAS controller gains can be addressed into two aspects.

(a). The closed-loop performance output responses using the optimized CAS controller's gains are found to be severely oscillated in most lateral directional motion because the performance output amplitude and oscillation reduction were not considered in Eq. (1)

(b). Gridding optimization approach required the values to be assigned and evaluated at all grid elements. Therefore, large computational time and memory is excessively required.

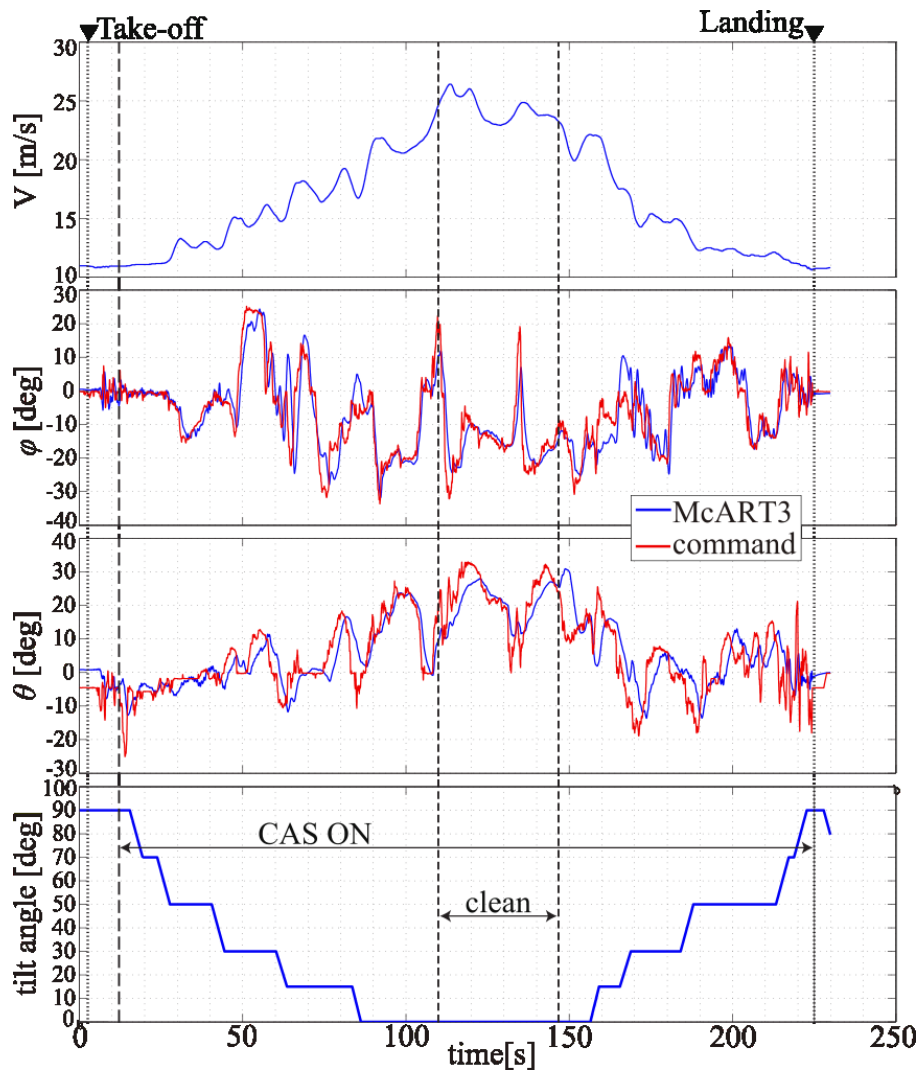


Fig. 1.6 Time history of McART3 full flight with JAXA flight controller

1.4. Research Objective

(a). An alternative potential method is proposed to design CAS controller using Particle Swarm Optimization (PSO) because of its oriented search algorithm over the large space within shorter calculation time than the gridding algorithm.

(b). H_∞ norm representation in frequency domain is considered instead of time domain constraints as the performance index for design CAS controller.

1.5. References

- 1.1) “Unmanned Aircraft Systems Roadmap: 2005–2030,” U.S. Dept. of Defense, Office of the Secretary of Defense, 2005, https://www.fas.org/irp/program/collect/uav_roadmap2005.
- 1.2) Daly, M., (ed.): Jane’s Unmanned Aerial Vehicles and Targets, International Helicopter Soc., Surrey, England, U.K., 2011.
- 1.3) Ahn, O. S., Kim, J. M., and Kim, C. H.: Smart UAV Research Program Status Update: Achievement of Tilt-Rotor Technology Development and Vision Ahead, ICAS 2010-6.2.1, Bonn, Germany, 2010.
- 1.4) Rutherford, J., and Bass, S.: Advanced Technology Tilt Wing Study, AIAA Aircraft Design Systems Meeting, AIAA Paper 1992-4237, SC, 1992.
- 1.5) “Unmanned Aircraft Systems Roadmap: 2005–2030,” U.S. Dept. of Defense, Office of the Secretary of Defense, 2005, https://www.fas.org/irp/program/collect/uav_roadmap2005.
- 1.6) <https://www.aviationsmilitaires.net/v2/base/view/Model/826.html>
- 1.7) <http://www.aero.jaxa.jp/eng/research/frontier/vtol/qtw/>
- 1.8) Muraoka, K., Okada, N., Kubo, D., and Sato, M.: Transition Flight of Quad Tilt Wing VTOL UAV, 28th International Congress of the Aeronautical Sciences, ICAS 2012-11.1.3, Bonn, Germany, 2012.
- 1.9) Sato, M. and Muraoka, K.: Flight Controller Design of Quad Tilt Wing Aircraft and Flight Tests -Basic Controller Using PID Control Scheme-, *the 52nd Aircraft Symposium*, 2014, JSASS-2014-5129.

Chapter 2

Background

Chapter Overview

This chapter describes McART3 QTW-UAV flight mechanism developed by JAXA which is used as a based model in this research. The next section covers an existing McART3 flight controller design as well as fundamental theories regarding to H_∞ control with loop shaping technique. Last, Particle Swarm Optimization is given as an. alternative potential method to optimize the propose controller.

2.1. McART3 configurations

The McART3 closed-loop dynamics consist of two feedback systems, Stability Augmentation System (SAS) and Control Augmentation System (CAS), as shown in Figure. 2.1 and 2.2. Table 2.1 and Table 2.2 shows McART3 longitudinal and lateral-directional motion flight parameters.

McART3 longitudinal motion dynamic is given as follow^{2.1}):

$$\begin{aligned} \dot{x} &= \text{nominal } x + B(\tau_w)u, \\ y &= Cx + Du, \end{aligned}$$

where

$$\begin{aligned} x &= [u, w, q, \theta, \delta_{flev}, \delta_{pwelv}, \delta_{th}]^T, \\ u &= [\delta_{flev_c}, \delta_{pwelv_c}, \delta_{th_c}]^T. \end{aligned} \tag{2.1}$$

The usage of longitudinal SAS gains is shown in Table 2.3. k_{flev} and k_{pwelv} are engaged in longitudinal nominal plant state space matrix. Therefore, McART3 closed-loop

dynamics are represented as SISO models in each tilt angle configurations. The optimized SAS gains are investigated by JAXA for longitudinal motions models as shown in Table 2.4.

McART3 lateral-directional motion dynamics are given as follow^{2.1)}:

$$\begin{aligned} \dot{x} &= A_M x + B_M(\tau_w)u, \\ y &= Cx + Du, \end{aligned}$$

where

$$\begin{aligned} x &= \begin{bmatrix} v & p & \phi & r & \delta_{fail} & \delta_{pwail} & \delta_{flrud} & \delta_{rud} & \delta_{pwrud} \end{bmatrix}^T, \\ u &= \begin{bmatrix} \delta_{flail_c} & \delta_{pwail_c} & \delta_{flrud_c} & \delta_{rud_c} & \delta_{pwrud_c} \end{bmatrix}^T. \end{aligned} \tag{2.2}$$

Lateral-directional motions with only SAS gains are implemented through this section. The SAS gains, k_{flail} , k_{pwail} , k_{flrud} , k_{rud} and k_{pwrud} , are engaged into nominal and the perturbed lateral-directional motion state space matrix. The usage of SAS gains and the optimized SAS gains under the controller ranges for lateral-directional motions are performed by JAXA as shown in Table 2.5. This research is primarily set all the inner loop SAS gains similar to JAXA in all tilt angle configurations in order to guarantee the primary stability of the McART3.

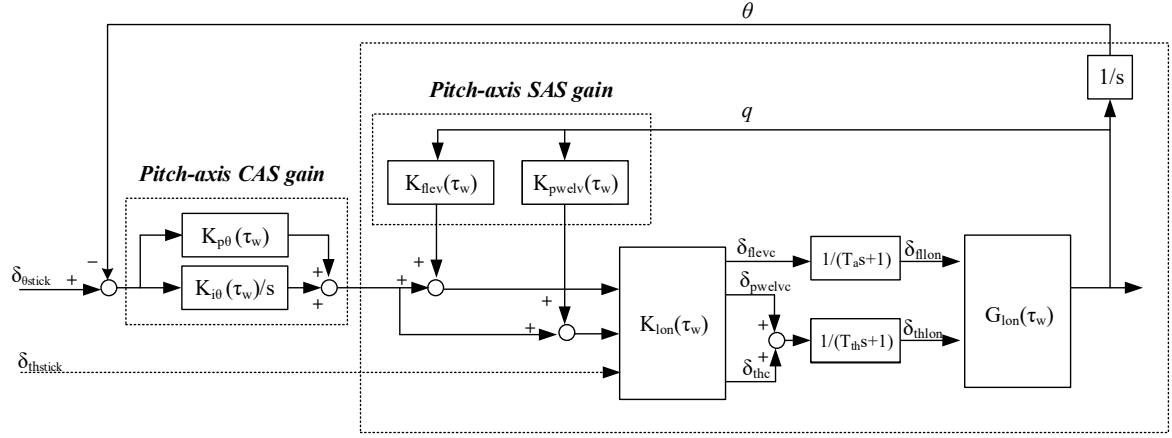


Fig. 2.1. The longitudinal motion control block diagram.^{2.2)}

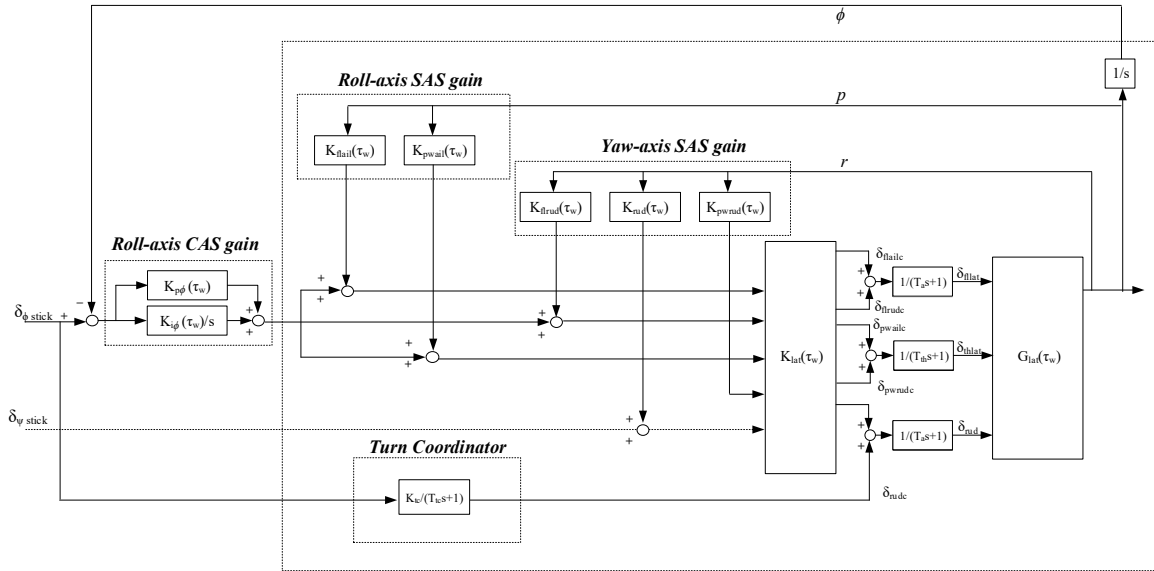


Fig. 2.2. The lateral-directional motion control block diagram.^{2.2)}

Table 2.1. McART3 flight parameters of Longitudinal motions^{2.2)}

Longitudinal Motion Flight Parameters		
Parameters	Parameter Names	Values
u, w	forward speed, vertical speed	state var.
q, θ	pitch rate, pitch angle	state var.
k_{flelv}	flap elevator gain	SAS gains
k_{pwelw}	power elevator gain	SAS gains
$K_{p\theta}$	K_p gain in each tilt angle	CAS gains
$K_{i\theta}$	K_i gain in each tilt angle	CAS gains
$\delta_{\theta Stick}$	pilot pitch stick input position	pilot input
δ_{flelv}	flap elevator command	command
δ_{pwelw}	power elevator command	command
$\delta_{th Stick}$	pilot throttle stick position	pilot input
$K_{lon}(\tau_w)$	longitudinal primary flight control	system
$G_{lon}(\tau_w)$	longitudinal linearized dynamic model	system
T_a, T_{th}	model actuator and model motor time constant	0.25,0.23
τ_w	tilt angle	angle index
$\delta_{fl,lon}$	flaperon angles for longitudinal motion	Flaperon. Angle(rad)
$\delta_{th,lon}$	throttle positions for longitudinal motion	Throttle positions

Table 2.2. McART3 flight parameters of lateral - directional motion^{2.2)}

Lateral - directional Motion Flight Parameters		
Parameters	Parameter Names	Values
v	lateral air speed	state var.
p	roll rates	state var.
ϕ, r	roll angle, yaw rate	state var.
δ_{flailc}	flap aileron command	command
δ_{pwailc}	power aileron command	command
δ_{flrudc}	flap rudder command	command
δ_{rudc}	rudder command	command
δ_{pwrudc}	power rudder command	command
k_{flail}	flap aileron gain	SAS gains
k_{pwail}	power aileron gain	SAS gains
k_{flrud}	flap rudder gain	SAS gains
k_{rud}	rudder gain	SAS gains
k_{pwrud}	power rudder gain	SAS gains
$\delta_{\phi stick}$	Roll stick input	pilot input
$\delta_{\psi Stick(c)}$	yaw stick input(command)	pilot input
$K_{lat}(\tau_w)$	primary flight control	system
$G_{lat}(\tau_w)$	linearized dynamic model	system
T_a, T_{th}	model actuator and model motor time constant	0.25,0.23
τ_w	tilt angle	angle index
k_{tc}	turn coordinator gain	TC gains
T_{tc}	Turn coordinator time constant	Time const.

Table 2.3. The usage of McART3 feedback gains^{2.2)}
 (“x” denotes use, “-”denotes disuse)

McART3 SAS gain engagement							
Tilt	k_{flelv}	k_{pwelw}	k_{flail}	k_{pwail}	k_{flrud}	k_{rud}	k_{pwrud}
Cln	x	-	x	-	-	x	x
0	x	-	x	-	-	x	x
15	x	x	x	x	x	x	-
30	x	x	x	x	x	x	-
50	x	x	x	x	x	x	-
70	x	x	x	x	x	x	-
90	-	x	-	x	x	-	-

Table 2.4. The optimization results of SAS gains in longitudinal motions^{2.2)}
 (“-” denotes disuse)

Tilt	SAS gain ranges		Optimized by JAXA	
	k_{flelv}	k_{pwelw}	k_{flelv}	k_{pwelw}
Cln	[0,74]	-	74	x
0	[0,57]	-	57	x
15	[0,86]	[0,69]	86	69
30	[0,86]	[0,69]	86	69
50	[0,86]	[0,69]	86	69
70	[0,86]	[0,69]	86	69
90	-	[0,69]	-	69

Table 2.5. Optimization results of SAS gains in lateral-directional motions^{2.2)}
 (“-” denotes disuse)

Tilt angle	SAS gains of lateral directional motion ranges					Optimized SAS gains of lateral directional motion				
	k_{flail}	k_{pwail}	k_{flrud}	k_{rud}	k_{pwrud}	k_{flail}	k_{pwail}	k_{flrud}	k_{rud}	k_{pwrud}
cln	[46,86]	-	-	[0,150]	[0,401]	46	-	-	150	45
0	[46,86]	-	-	[0,150]	[0,401]	46	-	-	150	86
15	[57,86]	[29,69]	[0,86]	[0,100]	-	67	33	86	150	-
30	[11,103]	[40,97]	[0,86]	[0,100]	-	83	40	86	100	-
50	[11,103]	[40,97]	[0,86]	[0,100]	-	103	40	86	100	-
70	[0,86]	[29,69]	[29,86]	[0,100]	-	0	29	86	100	-
90	-	[29,69]	[29,86]	-	-	-	29	86	-	-

2.2. McART3 with fixed-structure controller framework

McART3 in longitudinal and lateral-directional motion systems have been modified in order to satisfy the generalized system framework for tuning fixed control structures as a SISO model as shown in Figure 2.3.

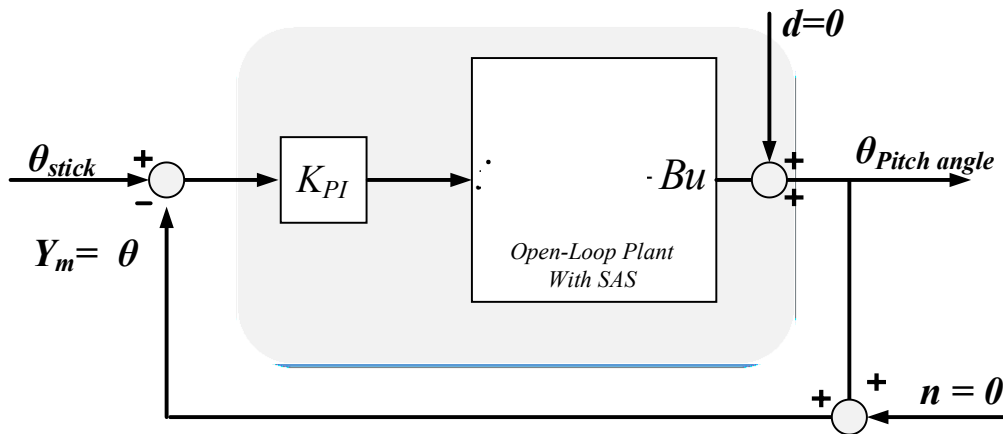


Fig. 2.3. SISO Closed-loop system with SAS integrated.

In general, the system architecture with fixed-structure controller block to tune is shown in figure 2.4. It is seen that the system consists of two main components:

(a) LTI model $\mathbf{P}(s)$ which combines all fixed, non- tunable, blocks in the control system.

(b) Structured controller $\mathbf{K}(s) = \text{diag} (K_1(s). . . K_N (s))$ which combines all tunable control elements. Each control element $K_i (s)$ is assumed to be linear time invariant.

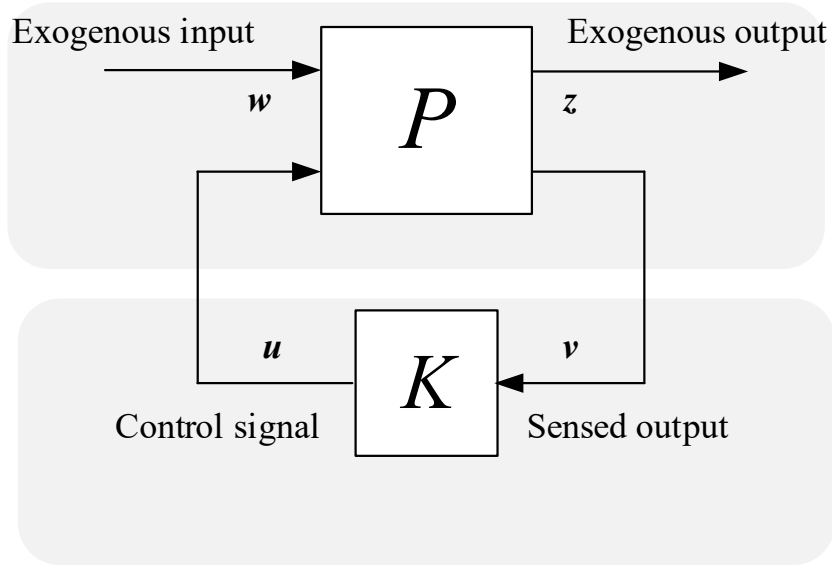


Fig. 2.4. Generalized system framework for tuning fixed control structures.

Where w is exogenous inputs: commandes, disturbance ,noise. z is exogenous outputs or “error” signals to be minimized. v is controller inputs for the general configuration. u is the control signals.

Typical close loop block diagram can be rearranged into such standard form by isolating the tunable blocks and collapsing the rest of the diagram into $\mathbf{P(s)}$. Sets of exogenous inputs to the system such as reference signals and disturbances are gathered in w and performance-related outputs such as error signals are gathered in z . For CAS controller synthesis, the model transformation can be formed as follows,

Cast Exogenous input: w

$$w = \begin{bmatrix} w_1 \\ w_2 \\ w_3 \end{bmatrix} = \begin{bmatrix} d \\ r \\ n \end{bmatrix} = \begin{bmatrix} 0 \\ \theta_{stick} \\ 0 \end{bmatrix} \quad (2.3)$$

Cast exogenous output: z

$$\begin{aligned} z &= error = y - r \\ z &= \theta - \theta_{stick} \end{aligned} \quad (2.4)$$

Cast controller inputs: v

$$\begin{aligned} v &= r - y_m \\ v &= \theta_{stick} - \theta \end{aligned} \quad (2.5)$$

The general feedback configurations in figure 2.4 and 2.5 have the controller K as a separate block. The model is sufficient in order to synthesizing the controller. However, for analysis of closed-loop performance the controller is given, by absorb K into the interconnection structure and obtain the close loop system N as shown in figure 2.6.

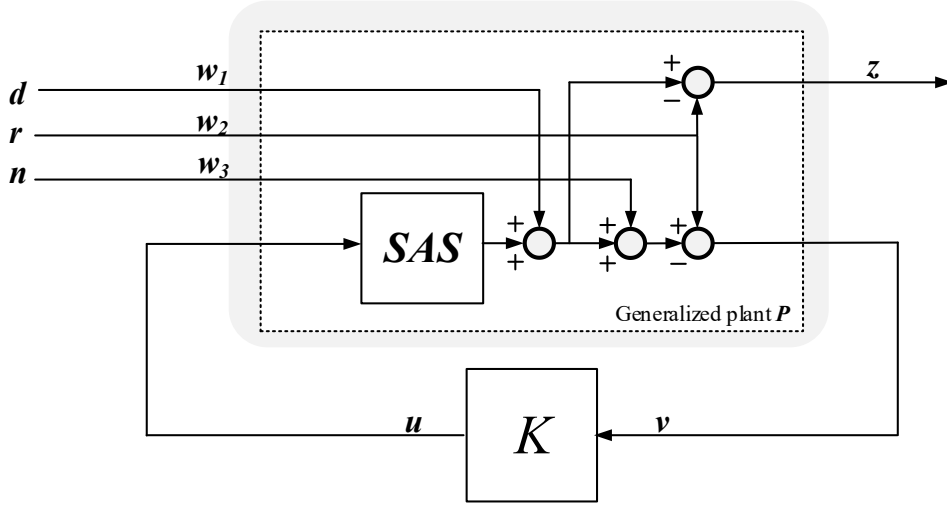


Fig. 2.5. Linear fractional model system.

Exogenous output and controller input vectors are derived as follows,

$$z = y - r = (Gu + d) - r = Gu - r \quad (2.6)$$

$$z = 0w_1 - Iw_2 + 0w_3 + Gu$$

$$v = r - y_m = r - Gu - d - n \quad (2.7)$$

$$v = 0w_1 + Iw_2 - 0w_3 - Gu$$

Set of inputs and outputs of the generalized plant P from $\begin{bmatrix} w & u \end{bmatrix}^T = \begin{bmatrix} z & v \end{bmatrix}^T$ can be obtained as follows,

$$\begin{bmatrix} w \\ u \end{bmatrix} = P \begin{bmatrix} z \\ v \end{bmatrix} \quad (2.8)$$

The generalize plant P is partitioned as follows,

$$P = \begin{bmatrix} P_{11} & \vdots \\ \cdots & \cdots \\ P_{21} & \vdots \end{bmatrix} \quad (2.9)$$

Such that, each parts are compatible with the signals w , z , u and v in the generalized control configuration as follows,

$$\begin{aligned} z &= P_{11}w + P_{12}u \\ v &= P_{21}w + P_{22}u \end{aligned} \quad (2.10)$$

P_{22} has dimensions compatible with the controller, i.e. if K is an $n_u \times n_v$ matrix, then P_{22} is an $n_u \times n_v$ matrix. For cases with one degree-of-freedom negative feedback control $P_{22} = -G$.

The generalized plant matrix can be found as

$$P = \begin{bmatrix} 0 & -I & 0 & +G \\ 0 & +I & 0 & -G \end{bmatrix} \quad (2.11)$$

QTW-closed loop

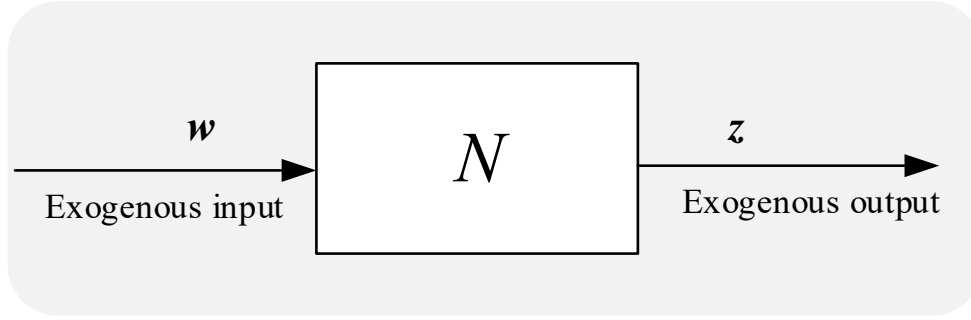


Fig. 2.6. General block diagram for analysis with no uncertainty.

QTW-UAV closed loop generalized system for tuning fixed control structures model N which shown in Figure 2.6 can be obtained as

$$z = Nw \quad (2.12)$$

Where N is a function of K and P . To find N , first partition the generalized plant P as given in (10) combine with the controller equation

$$u = Kv \quad (2.13)$$

In particular, CAS PI controller can be parameterized by two scalars K_p , K_i gain

$$K_{CAS} = K_p + \frac{K_i}{s} \quad (2.14)$$

Eliminate controller command u and its input v to yield $z = Nw$ where N is given by

$$N = P_{11} + P_{12}K(I - P_{22}K)^{-1}P_{21} \quad (2.15)$$

$$N \triangleq \begin{pmatrix} 1 & 0 \\ 0 & 1 \end{pmatrix}$$

Where $F_l(P, K)$ is a lower linear fractional transformation (LFT) of P with K as the parameters.

2.3. H_∞ Control via loop shaping

In this section, we introduce the shaping of the magnitudes of closed-loop transfer functions, where we synthesize a controller by minimizing an H_∞ performance objective. An alternative design strategy is to directly shape the magnitudes of closed-loop transfer functions, such as $S(s)$, sensitivity function, and $T(s)$ transmissibility function. Such a design strategy can be formulated as an H_∞ optimal control problem, thus automating the actual controller design and leaving the engineer with the task of selecting reasonable bounds (“weights”) on the desired closed-loop transfer functions. Before explaining how this may be done in practice, we discuss the terms H_∞ index.

2.3.1. H_∞ Terms

The H_∞ norm of a stable scalar transfer function $f(s)$ is simply the peak value of $|f(s)|$ as a function of frequency, that is,

$$\|f(s)\|_\infty \triangleq \sup_{\omega \in \mathbb{R}} |f(j\omega)| \quad (2.16)$$

Remark. In strictly constraint, replace “max” (the maximum value) by “sup” (the supremum, the least upper bound). This is because the maximum might only be approached as $\omega \rightarrow \infty$ and therefore not actually be achieved. However, for engineering purposes there is no difference between “sup” and “max”.

The terms H_∞ norm and H_∞ control is intimidating at first, and a name conveying the engineering significance of H_∞ would have been clarified. Next, design method which aims to press down the peak(s) of the selected transfer functions is describe as follows.

2.3.2. Weighted sensitivity

The sensitivity function S is a very good indicator of closed-loop performance, both for SISO and MIMO systems. The main advantage of considering S is that because we ideally want S small, it is sufficient to consider just its magnitude $|S(s)|$ that is, we need not worry about its phase. Typical specifications in terms of S include:

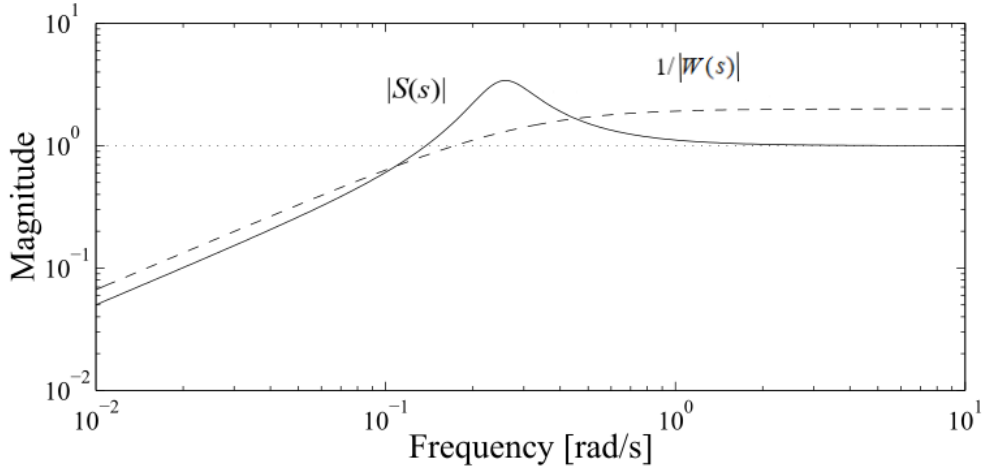
1. Minimum bandwidth frequency ω_{B^*} (defined as the frequency $|S(j\omega)|$ where crosses 0.707 from below).
2. Maximum tracking error at selected frequencies.
3. System type, or alternatively the maximum steady-state tracking error, A .
4. Shape of S over selected frequency ranges
5. Maximum peak magnitude of S , $\|S(j\omega)\|_\infty \leq M$

The peak specification prevents amplification of noise at high frequencies, and also introduces a margin of robustness; typically we select $M = 2$. Mathematically, these specifications may be captured by an upper bound, $1/|W(s)|$ on the magnitude of S , where $W(s)$ is a weight selected by the designer. The subscript P stands for performance since S is mainly used as a performance indicator, and the performance requirement becomes

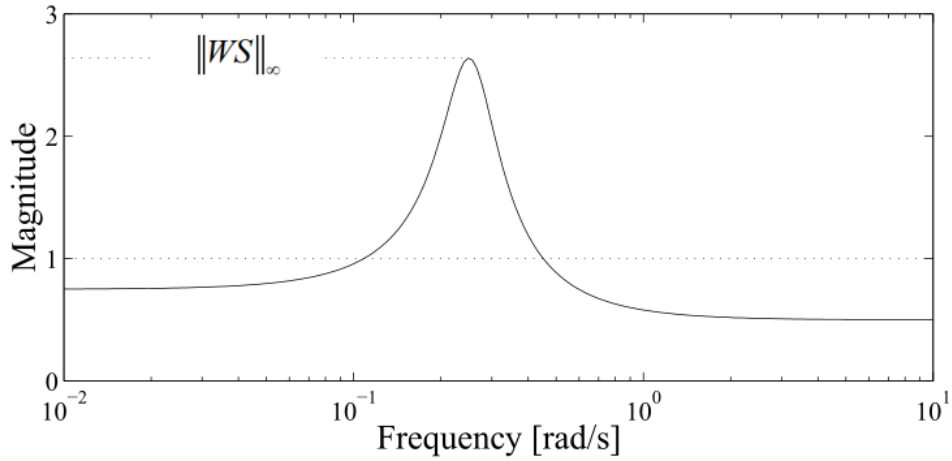
$$|S(j\omega)| < 1/|W(j\omega)|, \forall \omega \quad (2.17)$$

$$|WS| < 1, \forall \omega \Leftrightarrow \|WS\|_\infty < 1 \quad (2.18)$$

The last equivalence follows from the definition of the H_∞ norm, and in words the performance requirement is that the H_∞ norm of the weighted sensitivity, $|WS|$, must be less than one.



(a) Sensitivity S and performance weight W



(b) Weighted sensitivity WS

Fig. 2.7. Case where $|S(s)|$ exceed its bound $1/|W(s)|$ resulting in $\|WS\|_\infty > 1$.

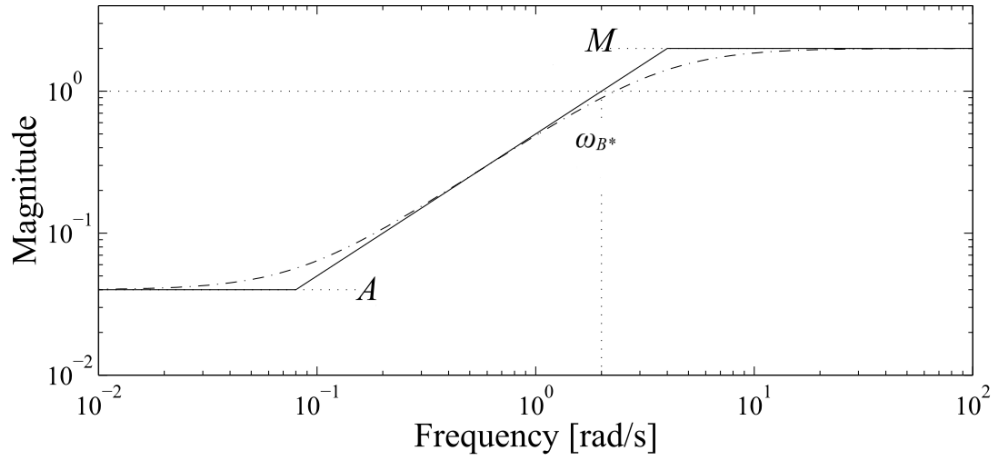


Fig. 2.8. Inverse of performance weight. Exact and asymptotic plot of $1/|W(s)|$.

2.4. Particle Swarm Optimization

Eberhart and Kennedy,^{2,3)} proposed a concept for an optimization of continuous nonlinear functions using particle swarm methodology which was inspired by the simplified movement behavior of organisms in a bird flock or fish school. In PSO, an “interesting site” corresponds to at least a local optimum of a certain function defined in a search space. This function can be given by a mathematical formula or, failing this, by an algorithm, or even by the outcome of a process, real or simulated. The main thing is that one can calculate its value at each point. For this simple version, we do not seek all the interesting sites, but only the most interesting, i.e. the global optimum of our function. With this intention, PSO takes as a starting point the cooperative behavior described in our metaphor: each particle is able to communicate to some others the position and quality of the best site it knows, a quality that one can interpret as its “value”. Let us call this set of particles connected to a given one by the descending information links the group of information receivers. Conversely, at every moment, a given particle can belong simultaneously to several informant groups and thus has a certain number of informants, who inform it about various more or less good sites. It is up to it to take

advantage of this information in order to define its next displacement. This operation of synthesis of information for an action has not yet been elucidated in biological reality, but has been the subject here of a very simple formalization (linear). This formalization does not claim to model the real behavior of bees or any other living organism. It simply proves to be effective for the resolution of many mathematical problems of optimization.

PSO consists of three extreme cases. In the first case, the particle is adventurous and intends to follow only its own way. Then it will allot a null confidence to received information and even to its own explorations: it will be satisfied with following more or less the already followed direction, i.e. the next displacement will be made with approximately the same velocity (intensity and direction) as the preceding one. In the second case, it is very conservative: it will grant great confidence to its best performance and will tend to return to it unceasingly. In the third case, it does not accord any confidence to itself, but instead moves according to the guidance of its best informant.

We thus have three fundamental displacements, shown in Figure 2.9 according to its current velocity; towards its own best performance; and towards that of its best informant. It is significant to note that “towards” in fact means “towards a point located not far from”, a concept that will be clarified by defining random proximities (to be exact, random distributions). In the same way, “according to its velocity” means “towards the point that would be reached by continuing with the same velocity vector”. The simplest way to calculate the true displacement starting from these three basic vectors is to make a linear weighting of it, thanks to confidence coefficients. All the skill of PSO consists of the judicious definition of these coefficients.

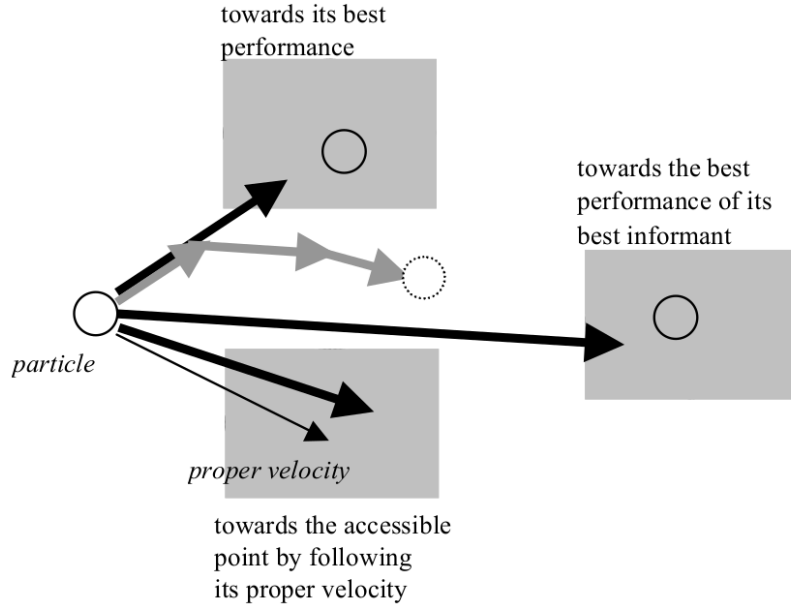


Fig. 2.9. Three fundamental elements for the PSO calculations

The optimization process is based on three steps, initialization, solution update with extremely non-complex calculations, and termination judgement using pre-defined termination condition. With regard to this algorithm, “particles” is used to represent candidates of the solution to the problem. Not only the local optima obtained by each particle at all previous iteration steps but also the global optimum obtained by whole particles, i.e., “swarm” at the current iteration step, are used to update the candidates.

The design procedures are briefly summarized below. In the initialization, a large number of particles are with randomly chosen solutions in feasible search space, and the maximum iteration step number k_{max} is defined. In the solution update, the best previously obtained solution of i^{th} particles ($\mathbf{x}_i^{best,k}$) and the best solution ($\mathbf{x}_{swarm}^{best,k}$) among all particles at the current iteration step k are calculated. Then, the velocity of each particle, which denotes the direction and the magnitude for updating the particle, are calculated by using these two kinds

of positions $(\mathbf{x}_i^{best,k}$ and $\mathbf{x}_{swarm}^{best,k}$) with random numbers $(r_{1,i}^k, r_{2,i}^k)$. In the termination judgement, the decision for continuing the iteration is given.

Suppose that cost function is given by $f(\mathbf{x})$, then the problem is given as Eq. (2.19).

$$\min_{\mathbf{x} \in \mathbb{R}^n} f(\mathbf{x}), \quad (2.19)$$

where the vector $\mathbf{x} = [x_1 \ \cdots \ x_n]^T$ denotes the particle's position whose elements

denote the design variables $x_i (i = 1, 2, \dots, n)$. PSO algorithm uses a swarm of m particles i.e., (n -dimensional vectors $\mathbf{x}_1, \mathbf{x}_2, \dots, \mathbf{x}_m$). The positions of the i -th particle and its velocity are respectively denoted by \mathbf{x}_i (i.e., $x_{i,1}, x_{i,2}, \dots, x_{i,n}$) and \mathbf{v}_i (i.e., $v_{i,1}, v_{i,2}, \dots, v_{i,n}$) where $i \in \{1, 2, \dots, m\}$. At iteration step k , $\mathbf{x}_i^{best,k}$ and $\mathbf{x}_{swarm}^{best,k}$ are defined as follows:

$$\mathbf{x}_i^{best,k} := \underset{\mathbf{x}_i^j}{\operatorname{argmin}} \{f(\mathbf{x}_i^j), 0 \leq j \leq k\}, \quad (2.20)$$

$$\mathbf{x}_{swarm}^{best,k} := \underset{\mathbf{x}_i^k}{\operatorname{argmin}} \{f(\mathbf{x}_i^k), \forall i\}. \quad (2.21)$$

Using these two solutions, the position and velocity of the i -th particle, \mathbf{x}_i and \mathbf{v}_i , are updated as follows:

$$\mathbf{x}_i^{k+1} = \mathbf{x}_i^k + \mathbf{v}_i^{k+1}, \quad (2.22)$$

$$\mathbf{v}_i^{k+1} = C_0 \mathbf{v}_i^k + C_1 r_{1,i}^k (\mathbf{x}_i^{best,k} - \mathbf{x}_i^k) + C_2 r_{2,i}^k (\mathbf{x}_{swarm}^{best,k} - \mathbf{x}_i^k). \quad (2.23)$$

High values of C_1 will demand the particles movements to be headed for their local best solutions. Similarly, high values of C_2 will demand the particles movements to be headed for the global best solution with fast convergence.

PSO algorithm is processed through the following the steps outlined below.

Step 0: Set k_{max} and iteration number $k = 0$. Initialize m particles with random positions in a feasible search space and evaluate the corresponding cost function values at each particle position, Calculate $\mathbf{x}_i^{best,0}$ and $\mathbf{x}_{swarm}^{best,0}$.

Step 1: If $k = k_{max}$, the algorithm stops with the solution with $\mathbf{x}^* := \underset{\mathbf{x}_i^j}{\operatorname{argmin}} \{f(\mathbf{x}_i^j), \forall i, j\}$.

Otherwise go to Step 2.

Step 2: Apply Eqs. (2.22) and (2.21) to all particles and calculate the corresponding cost function values at each position of particles. Update the iteration number, $k:=k+1$. Calculate $x_i^{best,k}$ and $x_{swarm}^{best,k}$ before go back to Step 1.

PSO technique has many interesting properties. It does not require the smoothness of the cost function with respect to design variables, nonlinear constraints, i.e, admissible intervals for design variables, discontinuous of cost functions, can thus be easily incorporated by defining modified cost functions^{2.3)}. Moreover, PSO has been applied to various design problems, e.g., non convex optimization problems^{2.5)}, equality/ inequality constraints optimization problems^{2.6)}, structured controller design problem^{2.4,2.7,2.8)}, etc

2.5. References

- 2.1) Muraoka, K., Okada, N., Kubo, D., and Sato, M.: Transition Flight of Quad Tilt Wing VTOL UAV, 28th International Congress of the Aeronautical Sciences, ICAS 2012-11.1.3, Bonn, Germany, 2012.
- 2.2) Sato, M. and Muraoka, K.: Flight Controller Design of Quad Tilt Wing Aircraft and Flight Tests -Basic Controller Using PID Control Scheme-, the 52nd Aircraft Symposium, 2014, JSASS-2014-5129.
- 2.3) Kennedy, J and Eberhart, R.C.: Particle Swarm Optimization, Neural Networks, 1995. Proceedings., IEEE International Conference on. Perth, WA, Australia, 1995.
- 2.4) Maruta, I., Kim, T. and Sugie, T.: Fixed-structure H_∞ controller synthesis: A meta-heuristic approach using simple constrained particle swarm optimization, *Automatica*, **45** (2009) pp. 553–559.
- 2.5) Banks, A., Vincent, J., and Anyakoha, C.: A review of particle swarm optimization. Part I: Background and development. *Natural Computing*, **6** (2007), pp. 467–484.
- 2.6) Sedlaczek, K., & Eberhard, P. (2006).: Using augmented Lagrangian particle swarm optimization for constrained problems in engineering``>Using augmented Lagrangian particle swarm optimization for constrained problems in engineering. *Structural and Multidisciplinary Optimization*, **32** (2006), pp. 277–286.
- 2.7) Latha, K. , Rajinikanth, V. and Surekha, P. M.: PSO-Based PID Controller Design for a Class of Stable and Unstable Systems, *ISRN Artificial Intelligence*, **2013** (2013).
- 2.8) Alfi, A. and Modares, H.: System identification and control using adaptive particle swarm optimization, *Applied Mathematical Modelling*, **35** (2011), pp. 1210–1221.

Chapter 3

H_∞ Control Based CAS Design of QTW-UAV Using Particle Swarm Optimization

Chapter Overview

This section proposes H_∞ control based Control Augmentation System (CAS) design of Quad Tilt Wing (QTW) Unmanned Aerial Vehicle (UAV) using Particle Swarm Optimization (PSO). In contrast to the previously used method, the design requirements for CAS gains are given in frequency domain to adjust the frequency characteristics from attitude command to attitude error, and PSO is used to reduce the numerical complexity coming from brute-force method, i.e., gridding method. The applicability of our method is first confirmed by designing CAS gains which have almost the same performance as the previous design, then non-oscillatory CAS gains are designed as an application of our method.

3.1. Chapter Introduction

Unmanned Aerial Vehicle (UAV) has been widely researched in the last two decades^{3.1-3}. In particular, Quad-Tilt-Wing Unmanned Aerial Vehicle (QTW-UAV) has gained more attention as a possible tool for various applications such as surveillance, scientific measurement^{3.1-3}, etc. Japan Aerospace Exploration Agency (JAXA) has therefore developed a series of QTW-UAVs (McART2^{3.4}, AKITSU^{3.5}, and McART3^{3.6}). The flight test of AKITSU was conducted to verify the feasibility of aircraft with practically sized QTW-UAV.

It successfully flew from helicopter mode to airplane mode, and vice versa; however, oscillatory motions were found in both longitudinal and lateral-directional motions^{3.5)}. Similar motions were also found in the flight test of McART3^{3.6)}. In particular, the oscillatory motion in the lateral-directional motions was sometimes large and it thus should be suppressed for flight safety. This section aims to be the first step to solve this problem.

The drawbacks of the CAS design in 3.5) and 3.6) are twofold, i.e., time domain design and optimization method. The details are given below. Controller gains are designed in time domain for good tracking performance by minimizing the error between attitude (roll and pitch angles) and its step-type input command. The obtained gains worked well in flight tests as shown in 3.5) and 3.6). However, it is difficult to prevent the oscillatory motions completely as shown in the data of full conventional flights for both QTW-UAVs. This is because it is not so easy to impose time-domain constraints for suppressing oscillatory motions. Next, CAS gains are optimized by brute-force method, i.e., grid search optimization method. When the controller ranges are wide and/or the number of the gains increases, large computational time will be required.

At the current moment, CAS is composed of only two control gains (proportional and integral gains) in the longitudinal as well as lateral-directional motions. However, it might be a problem when complex CAS is adopted to enhance control performance.

To tackle the drawbacks, we propose a design method with frequency domain constraints via reduced computational complexity for the optimization; that is, CAS gains are designed by loop shaping technique within H_∞ framework, and Particle Swarm Optimization (PSO) method which is one of oriented search algorithms is used as an alternative to the brute-force method with small computational complexity. As shown in 3.7), PSO is more effective than Generic Algorithm (GA), which is one of the most famous meta-heuristic methods, in

terms of computation time. In addition, PSO does not require any gradient or derivative of the cost function. Thus, it can be easily applied to the problems in which cost functions are non-smooth with respect to controller gains to be designed.

3.2. Design Problem and Method

This research uses the block diagram shown in Figure 3.1 for designing fixed structured CAS gains. Stability Augmentation System (SAS) is integrated into the block named “McART3 dynamics model with SAS” which also includes primary flight control system. Fixed-structured CAS consists of partial and integral gains both of which are required to be designed. The design requirement is to satisfy a constraint for the weighted sensitivity function from attitude command to attitude error.

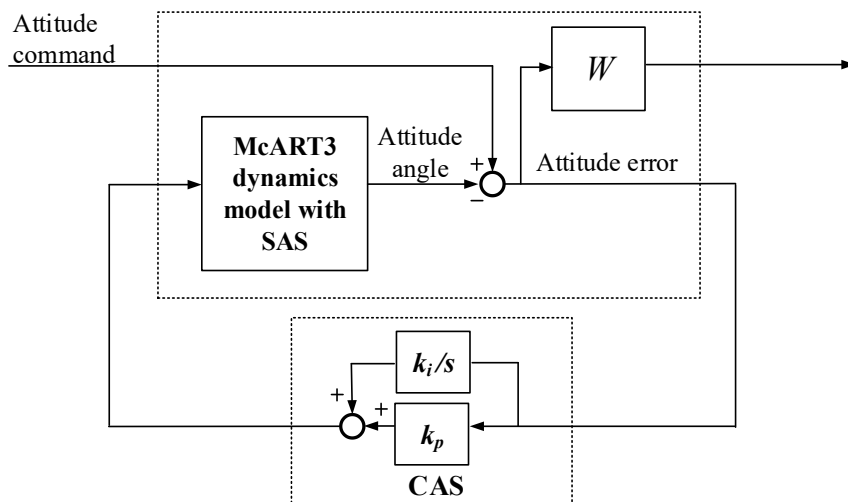


Fig. 3.1. Block diagram for fixed structured CAS in H_∞ framework.

3.2.1. Loop-shaping technique

Loop-shaping technique^{3,8)} within H_∞ control framework is used in this section. The

CAS gains are searched to satisfy the constraint in Eq. (3.1) with an appropriately chosen

weighting function $W(s)$ for the sensitivity function $S(s)$ which represents the transfer function from attitude command to attitude error.

$$\|W(j\omega)S(j\omega)\|_{\infty} < 1 \quad (3.1)$$

If this constraint is satisfied, then the sensitivity function $S(s)$ satisfies $|S(j\omega)| < 1/|W(j\omega)|$ for all frequencies ω , since we now consider Single-Input-Single-Output (SISO) systems; that is, the gain of the inverse of the weighting function, i.e., $1/|W(j\omega)|$, is interpreted as an upper bound of the magnitude of the sensitivity function $S(j\omega)$. Thus, loop-shaping for sensitivity function can be conducted by choosing suitable weighting function $W(s)$.

3.2.2. Particle swarm optimization

Thanks to the attractive property that PSO does not require the smoothness of the cost function with respect to design variables, nonlinear constraints, such as, admissible intervals for design variables, discontinuous cost functions, can be easily incorporated by defining modified cost functions^{3.10)}. PSO has been applied to various design problems, e.g., non-convex optimization problems^{3.11)}, equality/ inequality constraints optimization problems^{3.12)}, structured controller design problem^{3.10,3.13-14)}, etc.

3.3. Results

We first show the design results in which the target sensitivity function is set as the one with CAS gains in 3.6), then show the design results for oscillatory suppressing CAS. In both cases, the weighting function $W(s)$ is chosen as a low-pass filter whose characteristics are parametrized with three parameters, Direct Current (*DC*) gain, cut-off frequency (ω_c), and High Frequency (*HF*) gain. We use 50 particles and set k_{max} as 50 in our design.

3.3.1. Basic design

To confirm the applicability of our proposed method, for the nominal McART3 models at all design tilt angles in 3.6), we tried to design CAS gains which have almost the same frequency characteristics as in 3.6) by using our proposed method. Appropriate weighting functions are very important in our method and they are determined as follows: *DC* gains are first set as 1.0×10^{-6} to realize good tracking performance in low frequencies as in 3.6), then *HF* gains are set closely to the maximum peak gains of the closed-loop sensitivity function using the gains in 3.6), and finally ω_c is adjusted by trial-and-errors to realize the target tracking performance. By following the procedures above, we obtained CAS gains shown in Table 3.1 (a) and (b). The optimized gains are almost the same as in 3.6) apart from clean and 70-degree case in the longitudinal motions and from 15 degrees to 70 degree cases in the lateral-directional motions. However, it is confirmed that the step responses with those gains are almost the same as the gains in 3.6). For reference, Figure 3.2 shows the gain plots of the sensitivity functions with gains in Table 3.3, and the inverse of our weighting functions for the longitudinal motions and the lateral-directional motions at 15 degrees. These results confirm the applicability of our method (for reference in basic design, all tilt angles results are provided in Appendix A).

3.3.2. Extension to oscillatory suppressing CAS

As an extension of the basic design, we address oscillatory suppressing CAS design in the lateral-directional motions. We also addressed the same problem for the longitudinal motions; however, we couldn't design suitable CAS gains due to the restricted intervals for the admissible CAS gains. Weighting functions for oscillatory suppression CAS gains are determined in almost the same manner as basic design; however, only HF gains are adjusted as lower than the maximum peak gains of the sensitivity functions with CAS gains in 3.6) by

several trial-and-errors. By using the weighting functions obtained in the above, we design CAS gains for the lateral-directional motions. In particular, the designed CAS gains at 15 and 30 degrees, which are shown in Table 3.1(c), reduce the oscillatory motions. The gain plots of the sensitivity functions and step responses are respectively shown in Figures 3.3 and 3.4. It is confirmed that, in Figure 3.3, the peaks of the oscillated motions are indeed suppressed compared to the results in 3.6); however, in exchange for the suppression of oscillatory motions, slightly slow responses are confirmed in Figure 3.4. Regarding HF gain, if it is set as just above unity, then the designed controller gains tend to have the property that step responses are overdamped, viz., no oscillations; however, the settling time is too large. Thus, HF gains should be appropriately set to suppress oscillatory motions while good tracking performance is maintained.

Table 3.1. (a) Admissible CAS gain regions, CAS gains in 3.6), and optimized CAS controller gains using our method. [Basic design - longitudinal motion]

Tilt Angle	Admissible CAS gain			Nominal weighting		
	domains(K_{lon})		$[k_{p\theta}, k_{i\theta}]$	$[k_{p\theta}, k_{i\theta}]$	function ($1/W_{Nominal}$)	$\ W(j\omega)S(j\omega)\ _{\infty}$
	k_p	k_i	JAXA	PSO	[makeweight(DC, ω_c, HF)]	
CLN	[0,-70]	[0,-70]	[-70, -33]	[-42.59 , -2.49]	makeweight(1e-6, 0.9 , 1.1)	0.9512
0	[0,-100]	[0,-100]	[-100, -100]	[-99.99, -98.31]	makeweight(1e-6, 0.95 , 2.6)	0.9669
15	[0,-150]	[0,-100]	[-150, -100]	[-145.88, -91.90]	makeweight(1e-6, 0.3 , 1.9)	0.9635
30	[0,-150]	[0,-100]	[-150, -100]	[-149.84, -99.98]	makeweight(1e-6, 0.3 , 1.9)	0.9243
50	[0,-100]	[0,-70]	[-100, -70]	[-99.82, -67.61]	makeweight(1e-6, 0.4 , 1.75)	0.9890
70	[0,-50]	[0,-40]	[-50, -40]	[-49.47, -19.91]	makeweight(1e-6, 0.97 , 5.5)	0.9792
90	[0,-50]	[0,-40]	[-50, -40]	[-50.00 -40.00]	Unstable – pilot engage	

Table 3.1. (b) Admissible CAS gain regions, CAS gains in 3.6), and optimized CAS controller gains using our method. [Basic design - longitudinal motion]

Tilt Angle	Admissible CAS gain			Nominal weighting		
	domains(K_{lat})		$[k_{p\varphi}, k_{i\varphi}]$	$[k_{p\varphi}, k_{i\varphi}]$	function ($1/W_{Nominal}$)	$\ W(j\omega)S(j\omega)\ _{\infty}$
	k_p	k_i	JAXA	PSO	[makeweight(DC, ω_c, HF)]	
CLN	[0,-100]	[0,-50]	[-100, -50]	[-94.18 -49.54]	makeweight(1e-6, 2 , 2)	0.9932
0	[0,-100]	[0,-50]	[-100, -50]	[-94.00 -48.39]	makeweight(1e-6, 0.65 , 3)	0.9813
15	[0,-100]	[0,-50]	[-100, -50]	[-78.60 -49.70]	makeweight(1e-6, 0.6 , 2)	0.9975
30	[0,-120]	[0,-50]	[-88, -50]	[-106.05 -48.47]	makeweight(1e-6, 2 , 3)	0.9761
50	[0,-80]	[0,-50]	[-80, -50]	[-64.23 -49.52]	makeweight(1e-6, 1.7 , 1.6)	0.9728
70	[0,-50]	[0,-40]	[-50, -40]	[-27.20 -39.24]	makeweight(1e-6, 0.6 , 1.5)	0.9925
90	[0,-50]	[0,-40]	[-50, -40]	[-43.63 -39.72]	makeweight(1e-6, 0.3 , 1.5)	0.9936

Table 3.1. (c) Admissible CAS gain regions, CAS gains in 3.6), and optimized CAS controller gains using our method. [Extension design - lateral directional motion]

Admissible CAS gain			Oscillatory reduction		
Tilt	domains(K_{lat})		$[k_{p\varphi}, k_{i\varphi}]$	$[k_{p\varphi}, k_{i\varphi}]$	weighting function ($1/W_{\text{osc}}$) $\ W(j\omega)S(j\omega)\ _{\infty}$
Angle	$k_{p\varphi}$	$k_{i\varphi}$	JAXA	PSO	[makeweight(DC, ω_c, HF)]
15	[0,-100]	[0,-50]	[-100, -50]	[-25, -45]	makeweight(1e-6, 0.6, 1.36)
30	[0,-120]	[0,-50]	[-88, -50]	[-27, -22]	makeweight(1e-6, 1 ,1.25)

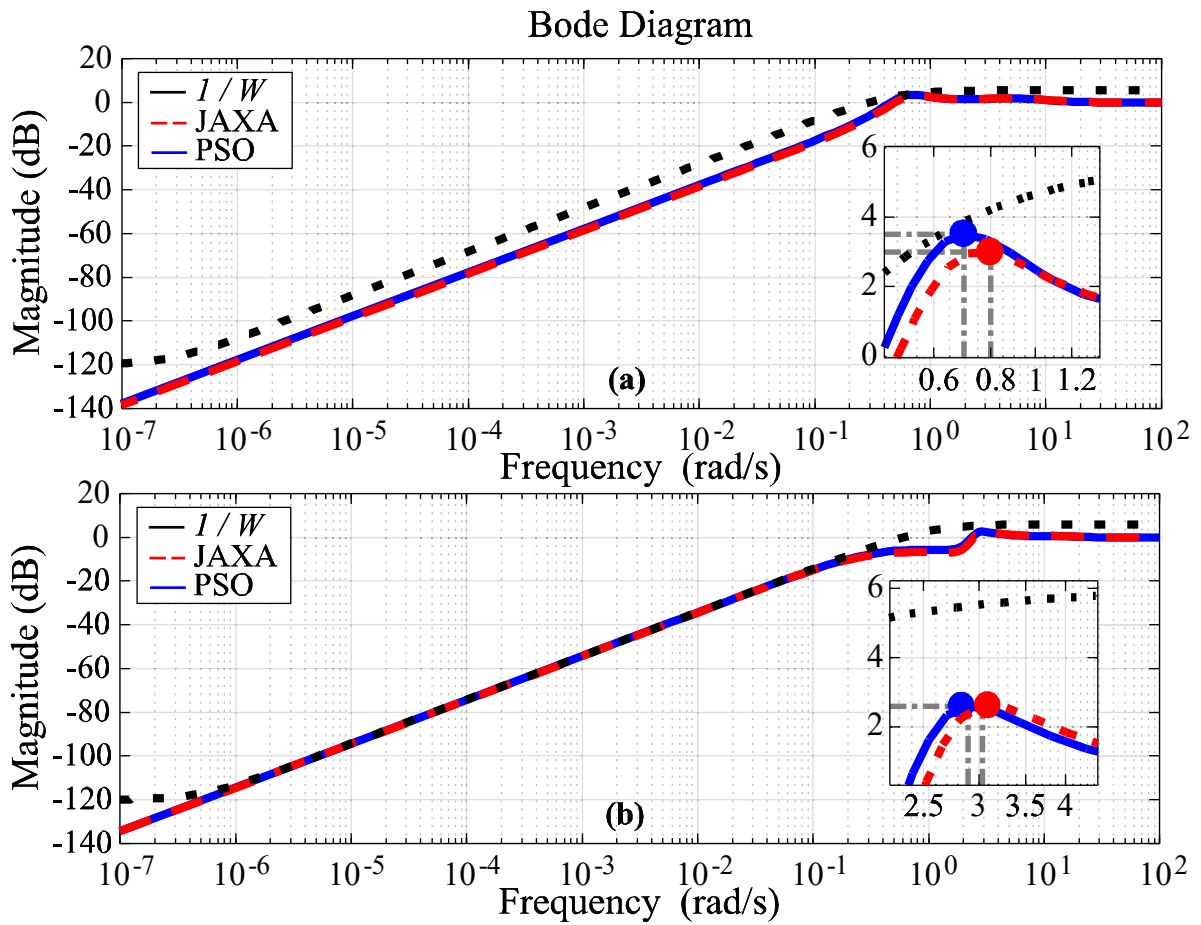


Fig. 3.2. Gain plots of sensitivity functions with CAS gains in 3.6), optimized gains in Table 3.1 (a) and (b), and $1/|W(s)|$ (Close-look figures at max peak gains are given in the boxes.) (a) $\tau_\omega = 15^\circ$ [lon. motion] (b) $\tau_\omega = 15^\circ$ [lat.-dir. motion].

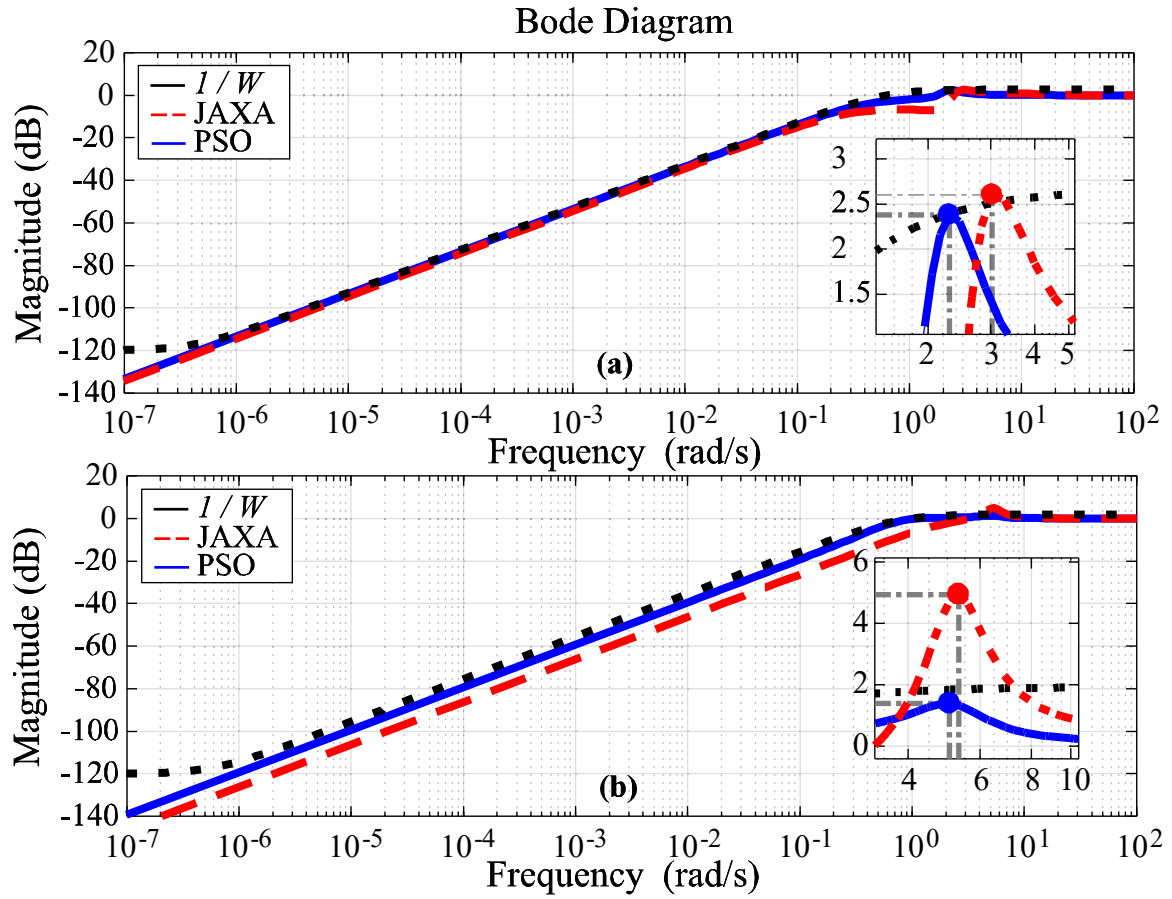


Fig. 3.3. Gain plots of sensitivity functions with CAS gains in 3.6), optimized gains in Table 3.1 (c), and $1/W(s)$ (Close-look figures around max peak gains are given in the boxes.) (a) $\tau_\omega = 15^\circ$ and (b) $\tau_\omega = 30^\circ$ [lat.-dir. motions].

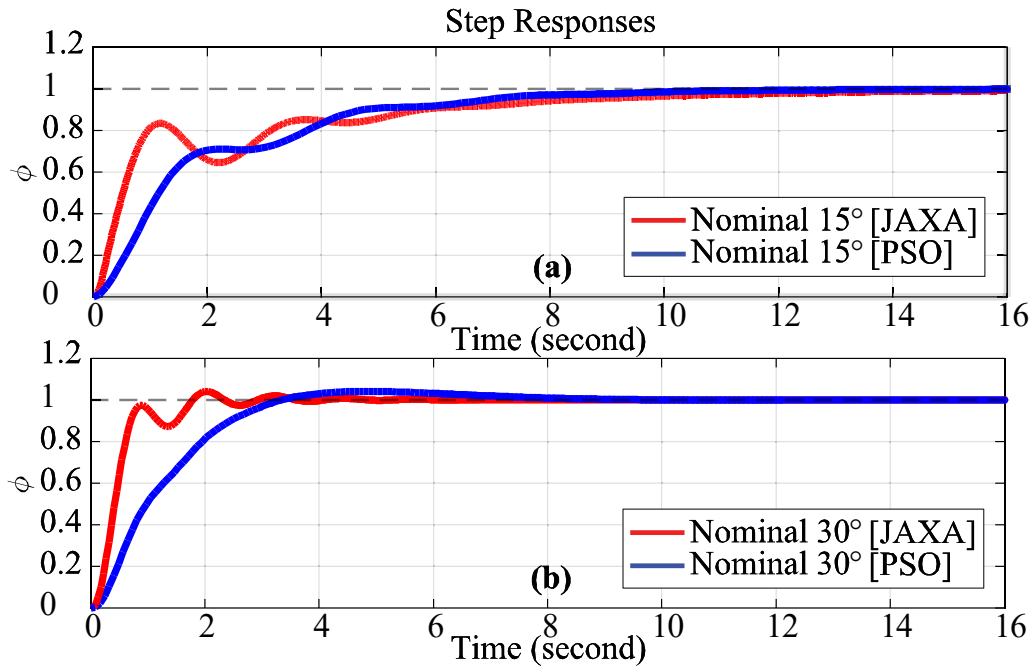


Fig. 3.4. Step responses of ϕ at (a) $\tau_\omega = 15^\circ$ and (b) $\tau_\omega = 30^\circ$.

3.4. Chapter summary

To address the drawbacks in existing design methods for Quad Tilt Wing Unmanned Aerial Vehicle (QTW- UAV), i.e., oscillatory motions and a large numerical complexity in controller gain design, this chapter proposes a method for Control Augmentation System (CAS) design with the application of Particle Swarm Optimization (PSO). In contrast to the previously used method, the design requirements are given in frequency domain, to be more specific, weighted sensitivity function from attitude command to attitude error is required to satisfy an H^∞ norm constraint. We first verify the applicability of our method by CAS design for McART3 in which the target sensitivity function is given by using the gains in an existing paper. Then, as an extension, we address oscillatory suppressing CAS design. In exchange for slightly slow responses, oscillatory sup-pressing CAS gains are obtained in the latter problem.

3.5. References

- 3.1) Cox, T. H., Nagy, C. J., Skoog, M. A., and Somers, I. A.: Civil UAV Capability Assessment, NASA TR, Dec. 2004.
- 3.2) Hassanalian, M. and Abdelkefi, A.: Classifications, applications, and design challenges of drones: A review, *Progress in Aerospace Sciences*, 91 (2017), pp. 99–131.
- 3.3) Unmanned Aircraft Systems Roadmap:2005–2030, U.S. Dept. of Defense, Office of the Secretary of Defense, 2005, https://www.fas.org/irp/program/collect/uav_roadmap2005.pdf (accessed October 20, 2013).
- 3.4) Muraoka, K., Okada, N., Kubo, D., and Sato, M.: Transition Flight of Quad Tilt Wing VTOL UAV, 28th International Congress of the Aeronautical Sciences, ICAS 2012-11.1.3, Bonn, Germany, 2012.
- 3.5) Sato, M. and Muraoka, K.: Flight Controller Design and Demonstration of Quad-Tilt-Wing Unmanned Aerial Vehicle, *Journal of Guidance, Control, and dynamics*, **38** (2015), pp. 1071–1082.
- 3.6) Sato, M. and Muraoka, K.: Flight Controller Design for Small Quad Tilt Wing UAV, *Journal of the Japan Society for Aeronautical and Space Sciences*, **64** (2016), pp. 79–82(in Japanese).

- 3.7) Yavari, S., Zoj, M. J. V., Mokhtarzade, M., Mohammadzadeh, A.: Comparison of Particle Swarm Optimization and Genetic Algorithm in Rational Function Model Optimization, *International Archives of the Photogrammetry, Remote Sensing and Spatial Information Sciences*, Volume XXXIX-B1 (2012), pp. 281–284.
- 3.8) Skogestad, S. and Postlethwaite, I.: *Multivariable Feedback Control Analysis and Design Second Edition*, John Wiley& Sons Press, New York, 2001, pp. 55–57.
- 3.9) Kennedy, J and Eberhart, R.C.: Particle Swarm Optimization, Neural Networks, 1995. Proceedings., IEEE International Conference on. Perth, WA, Australia, 1995.
- 3.10) Maruta, I., Kim, T. and Sugie, T.: Fixed-structure H_∞ controller synthesis: A meta-heuristic approach using simple constrained particle swarm optimization, *Automatica*, **45** (2009) pp. 553–559.
- 3.11) Banks, A., Vincent, J., and Anyakoha, C.: A review of particle swarm optimization. Part I: Background and development. *Natural Computing*, **6** (2007), pp. 467–484.
- 3.12) Sedlaczek, K., & Eberhard, P. (2006): Using augmented Lagrangian particle swarm optimization for constrained problems in engineering`>`Using augmented Lagrangian particle swarm optimization for constrained problems in engineering. *Structural and Multidisciplinary Optimization*, **32** (2006), pp. 277–286.
- 3.13) Latha, K. , Rajinikanth, V. and Surekha, P. M.: PSO-Based PID Controller Design for a Class of Stable and Unstable Systems, *ISRN Artificial Intelligence*, **2013** (2013).
- 3.14) Alfi, A. and Modares, H.: System identification and control using adaptive particle swarm optimization, *Applied Mathematical Modelling*, **35** (2011), pp. 1210–1221.

Chapter 4

H_∞ Control Based CAS Design for QTW-UAV via Multiple Model Approach with Particle Swarm Optimization

Chapter Overview

This chapter presents H_∞ control based Control Augmentation System (CAS) design for Quad Tilt Wing (QTW) Unmanned Aerial Vehicle (UAV) via multiple model approach with Particle Swarm Optimization (PSO). To realize robust control performance of the design CAS gains against possible plant modeling errors, multiple models approach is applied as the same manner as the previously published reports; however, in contrast to the previously used method, this chapter has two unique contributions. The design requirements for CAS gains are given in frequency domain to shape the frequency responses from attitude command to attitude error, and PSO is used to reduce the numerical complexity coming from a brute-force method, i.e., gridding method. The applicability of our method is first confirmed by designing common CAS gains which guarantee the robust performances of all candidate models, CAS gains that suppress oscillatory motions, which is one of the drawbacks of the previously designed CAS gains, are designed using our method. The applicability of the designed CAS gains is examined by faithful nonlinear flight simulations under no gust and wind gust conditions. In addition, the improvement of the performance of nominal models are further investigated when the probability density functions for the nominal models and the perturbed models are given *a priori* and the latter is less than the former.

4.1. Chapter Introduction

Unmanned Aerial Vehicle (UAV) has gained much attention among researchers and widely researched since the last two decades,^{4.1-3)}. Quad-Tilt-Wing Unmanned Aerial Vehicle (QTW-UAV) has particularly been considered as a possible tool for numerous fields of applications, e.g. surveillance, monitoring and scientific measurement^{4.1-3)}. Japan Aerospace Exploration Agency (JAXA) has thus designed and developed a series of QTW-UAVs (McART2^{4.4)}, AKITSU^{4.5)}, and McART3^{4.6)}). To verify the aircrafts feasibility, the flight test of AKITSU was conducted with practically sized QTW-UAV in outdoor environments. It successfully flied from helicopter mode to airplane mode, and *vice versa*; however, oscillatory motions were found in both longitudinal and lateral-directional motions^{4.5)}. Likewise, for AKITSU; similar motions were found during the flight test of McART3^{4.6)}. In particular, the oscillatory motion in the lateral-directional motions was sometimes large, and hence it should be suppressed for flight safety. This chapter aims to solve this problem.

The CAS gains in 4.5) and 4.6) are designed to be robust against the supposed modelling error of McART3 plants models. Using multiple models composed of a nominal configuration model and slightly off-nominal (perturbed) configuration models, more details on multiple model approach will be provided in beginning of the next section, CAS gains that are common to all the configuration models are successfully designed. However, the drawbacks of the CAS design in twofold, i.e., time domain design and optimization method. The details are summarized below. Controller gains are designed in time domain for good tracking performance. This is done by minimizing the maximum error between attitude (roll and pitch angles) and its step-type input command among nominal and its perturbed models. The obtained gains worked well in flight tests as shown in 4.5) and 4.6). However, it is difficult to completely prevent the oscillatory motions as shown in the time history data of full

conventional flights for both QTW-UAVs. This is because it is not so straightforward to impose constraints in time domain for suppressing oscillatory motions. Next, CAS gains are optimized by brute-force method, i.e., grid search optimization method. When the controller ranges are wide and/or the number of the control gains increases, large computational time will be inevitably required.

At this present moment, CAS is composed of only two control gains (proportional and integral gains) in the longitudinal as well as lateral-directional motions. Nevertheless, when the complex CAS is adopted to enhance control performance, this might unavoidably be problem. To overcome these drawbacks, this chapter proposes a design method with frequency domain constraints via reduced computational complexity for the optimization; that is, robust CAS gains are designed by loop shaping technique within H_∞ framework combine with the multiple models which are provided in 4.6), and Particle Swarm Optimization (PSO) method which is one of oriented search algorithms is used as an alternative to the brute-force method with small computational complexity. As shown in 4.7), PSO is more effective than Generic Algorithm (GA), which is one of the most famous meta-heuristic methods, in terms of computation time. In addition, PSO does not require any gradient or derivative of the cost function. Hence, it can be easily applied to the problems in which cost functions are non-smooth with respect to controller gains to be designed.

This research verifies our proposed method as a design tool for robust CAS gains, in which design requirements are given not in time domain but in frequency domain, and the applicability of PSO algorithm. To this end, the nominal and its perturbed models of McART3^{4,6)} are chosen as plant models, and the target frequency characteristics from attitude command to attitude error are chosen by the worst performance among the models with the CAS gains in 4.6). Solving this problem, the CAS gains which have robustly optimized control performance are obtained. Next, the CAS gains which suppress oscillatory motions are also

designed as a useful and practical application of the proposed technique. In addition, an improvement of nominal model performance problem is considered when the probability function is given as an extension of the robust gains design. The effectiveness of the proposed techniques is confirmed through McART3 lateral-directional step-responses simulations. The applicability of the optimized CAS controller gains is consequently verified through non-linear flight simulations under both normal and gust wind conditions for safe flight. This confirms that CAS gains which design in linear time invariant domain are also work well even in the nonlinear flight environments.

4.2. Design Problem and Method

This research uses the block diagram shown in Figure 4.1 for designing robust fixed structured CAS gains. Stability Augmentation System (SAS) is integrated into the block named “McART3 dynamics model with SAS” which also includes primary flight control system. Fixed-structured CAS consists of partial and integral gains both of which are required to be designed. To realize robust control performance of the design CAS gains against possible plant modeling errors, multiple model approach is applied in accordance with 4.6).

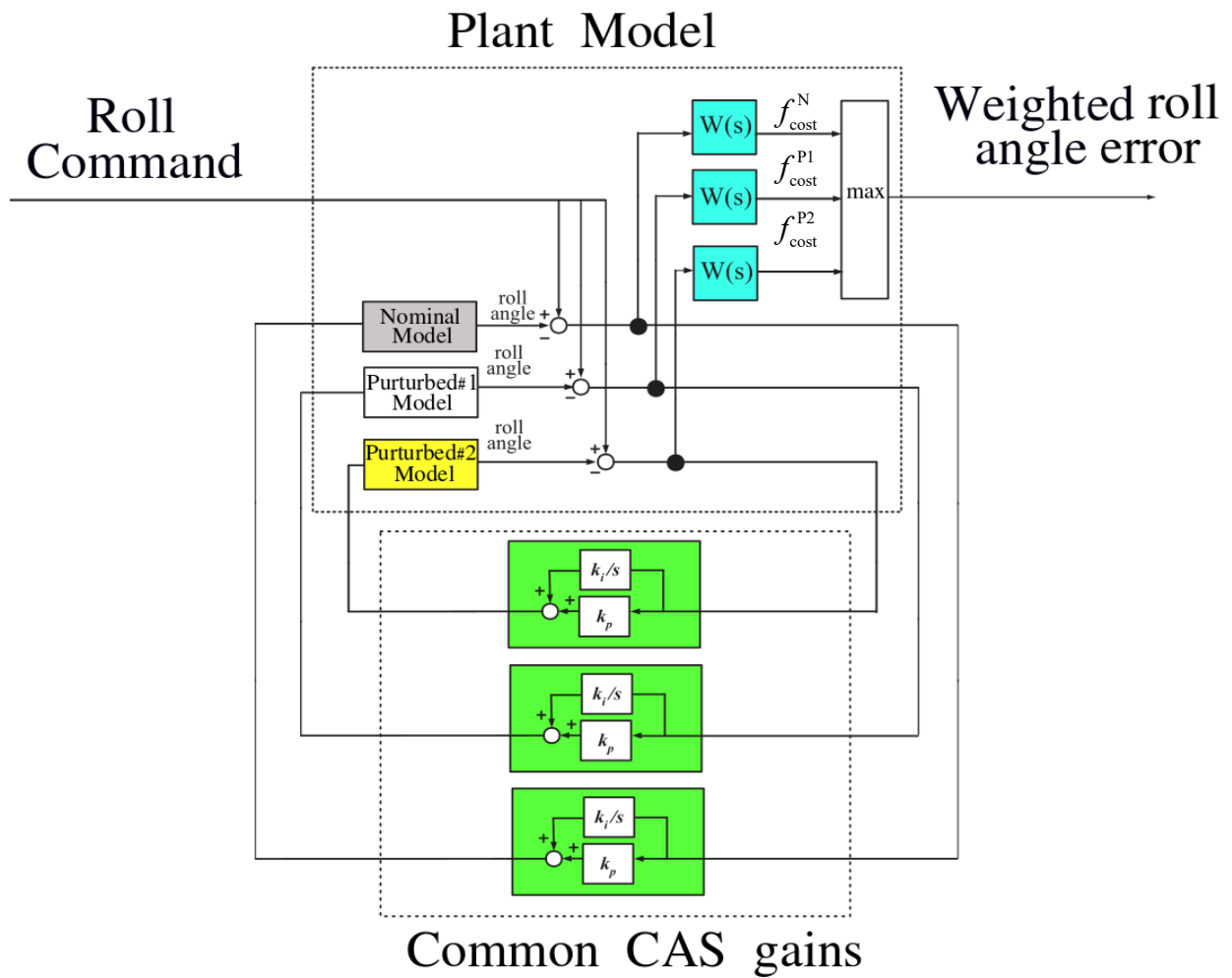


Fig. 4.1. Block diagram for robust fixed structured CAS in H_∞ framework.

Table 4.1. McART3 nominal and the perturbed models represent the supposed plants modeling errors in 4.6)

The nominal and perturbed models represent the modeling errors or uncertainty		
Designed point	Tilt angle	Model name
1 (T90)	90	Nominal
	80	Purturbed-2
2 (T70)	80	Purturbed -1
	70	Nominal
	60	Purturbed -2
	60	Purturbed -1
3 (T50)	50	Nominal
	40	Purturbed -2
	40	Purturbed -1
4 (T30)	30	Nominal
	20	Purturbed -2
	20	Purturbed -1
5 (T15)	15	Nominal
	10	Purturbed -2
	10	Purturbed -1
6 (T00)	0	Nominal
	0 (clean)	Purturbed -2
7 (TCLN)	0 (flap down)	Purturbed -1
	0 (clean)	Nominal

The idea of the multiple-model approach is simple and rational for designing practical controller gains. That is, CAS gains are robust against modeling errors represented by multiple designed plant models. To this end, the McART3 dynamics model with SAS is set as “nominal model”, and systems which are similarly generated at neighboring tilt angles are set as “perturbed models” to represent the possible modeling errors as shown in Table 4.1 Using

those models, we design common CAS gains with respect to the following control performance as follows:

$$\min_{\mathbf{k} \in K} \max_{\substack{\text{nominal and} \\ \text{perturbed models}}} f_{\text{cost}}(\mathbf{k}), \quad (4.1)$$

This formulation attempts to design the optimal CAS controller gain with the worst cost among all supposed models being minimized. Therefore, it is expected that the designed gains have robustly optimized control performance against the modeling errors which represented by the multiple models.

By using the block diagram in Fig. 4.1 we define sensitivity function and weighted sensitivity function as the transfer function from roll command to roll angle error and from roll command to weighted roll angle error. The sensitivity function correspond to the transfer function from “command” to “error” represented by “ S_N ” or “ S_{Pi} ” and the weighted sensitivity function correspond to the transfer function from “command” to “ f_{cost}^N ” or “ f_{cost}^{Pi} ”. Thus, in our problem, “ f_{cost} ” is defined as “ $W(s)$ ” with an appropriately set weighting function W . Next, common CAS gains for those models are designed to guarantee robustness against the modeling errors. The cost function $f_{\text{cost}}(\mathbf{k})$ in Eq. (4.1) is set as follows:

$$f_{\text{cost}}(\mathbf{k}) = \begin{cases} f_{\text{cost}}^N(\mathbf{k}), & \text{if plant is Nominal model,} \\ f_{\text{cost}}^{P1}(\mathbf{k}), & \text{if plant is Perturbed-1 model,} \\ f_{\text{cost}}^{P2}(\mathbf{k}), & \text{if plant is Perturbed-2 model.} \end{cases} \quad (4.2)$$

where

$$\begin{aligned} f_{\text{cost}}^N(\mathbf{k}) &= \|W(j\omega)S_N(j\omega)\|_{\infty} \\ f_{\text{cost}}^{P1}(\mathbf{k}) &= \|W(j\omega)S_{P1}(j\omega)\|_{\infty} \\ f_{\text{cost}}^{P2}(\mathbf{k}) &= \|W(j\omega)S_{P2}(j\omega)\|_{\infty} \end{aligned}$$

To proceed to CAS design via multiple model approach within H^∞ framework, $f_{\text{cost}}(\mathbf{k})$ in Eq. (4.1). The design requirement is set to satisfy a constraint to minimize the maximum weighted sensitivity functions from attitude command to attitude error.

4.2.1. Loop-shaping Technique

Loop-shaping technique^{4.8)} within H_∞ control framework is used in this section. The CAS gains are searched to satisfy the constraint in Eq. (4.1) with an appropriately chosen weighting function $W(s)$ for the sensitivity function $S(s)$ which represents the transfer function from attitude command to attitude error.

$$\|W(j\omega)S(j\omega)\|_\infty < 1 \quad (4.2)$$

If this constraint is satisfied, then the sensitivity function $S(s)$ satisfies $|S(j\omega)| < 1/|W(j\omega)|$ for all frequencies ω , since we now consider Single-Input-Single-Output (SISO) systems; that is, the gain of the inverse of the weighting function, i.e., $1/|W(j\omega)|$, is interpreted as an upper bound of the magnitude of the sensitivity function $S(j\omega)$. Thus, loop-shaping for sensitivity function can be conducted by choosing suitable weighting function $W(s)$.

4.2.2. Particle swarm optimization

Thanks to the attractive property that PSO does not require the smoothness of the cost function with respect to design variables, nonlinear constraints, such as, admissible intervals for design variables, discontinuous cost functions, can be easily incorporated by defining modified cost functions^{4.10)}. PSO has been applied to various design problems, e.g., non-convex optimization problems^{4.11)}, equality/ inequality constraints optimization problems^{4.12)}, structured controller design problem^{4.10,4.13-14)}, etc.

4.3. Results

We first present the design results in which the target sensitivity function is set as the one whose holds the maximum peak gain, among the nominal and perturbed models, using CAS gains in 4.6). Afterwards, we present the design results for oscillatory suppression for CAS. To specify loop shapes for CAS gains synthesis in both cases, the continuous-time first-order weighting function $W(s)$ is chosen as a low-pass filter whose characteristics are parametrized with three parameters, low frequency gain (*DC* gain), cut-off frequency (ω_c), and High Frequency gain (*HF* gain). In this research, we use a swarm of 50 particles. k_{\max} is set as 50 iterates. PSO factors C_0 , C_1 and C_2 are set as 0.2, 0.8 and 0.8, respectively. Next, an improvement of nominal model performance is designed when the probability function is given. Finally, we provide further evidence to confirm the applicability of our designed CAS via nonlinear-flight simulation under normal as well as gust wind conditions.

4.3.1. Basic design (Robust CAS gains design)

To confirm the applicability of the proposed method, we attempted to design common CAS gains which ensure the robust performance against the modeling errors using multiple models from Table 4.1. As a matter of fact, appropriate chosen weighting functions are crucially designed in our proposed method. Those are particularly determined as follows: *DC* gains are first set as 1.0×10^{-6} to realize good tracking performance in low frequencies as in 4.6), then *HF* gains are set closely to the maximum peak gains among the models of the closed-loop sensitivity functions using the gains in 4.6), and finally ω_c is adjusted by trial-and-errors to realize the target tracking performance. By following the proposed selecting weighting function strategy, we obtained CAS gains shown in Table 4.2 (a) and (b). Those obtained gains indicate the longitudinal motions as well as the lateral-directional motions are robustly

stabilized at all tilt angles apart from the longitudinal motions in 90 degree. For reference, figure 4.2 shows the gain plots of the sensitivity functions with gains in Table 4.2, and the inverse of proposed weighting functions for the longitudinal motions as well as the lateral-directional motions given at 30 degrees.

4.3.2. Extension to oscillatory suppressing CAS

In this section, we addressed oscillatory suppressing CAS design problem in only the lateral-directional motions. For the longitudinal motions, Similar problem is addressed as well; Nonetheless, because of the restricted intervals of the admissible CAS gains, the appropriate CAS gains cannot thus be designed due to this inevitable limitation.

Weighting functions for oscillatory suppression CAS gains are determined in almost similar manner as the previous basic design. In despite of this, *HF* gains are only refined to set lower than the maximum peak gains of the sensitivity functions among the nominal and perturbed models with CAS gains in 4.6) by several trial-and-errors.

By using the weighting functions obtained from the above, oscillatory suppression CAS gains are successfully designed for the lateral-directional motions as shown in Table 4.2(c). Those obtained gains indicate the lateral-directional motions are robustly stabilized and reduced the oscillatory motions. For references, the gain plots of the sensitivity functions and step responses at 30 and 50 degrees are shown in Figures 4.3 and 4.4, respectively. The results ensured that, in Figure 4.3, the peaks of the oscillated motions of the nominal as well as the perturbed models are indeed suppressed compared to the results in 4.6); however, in exchange for the suppression of oscillatory motions, slightly slow responses are confirmed in Figure 4.4. Regarding *HF* gain, if it is set as just above unity, then the designed controller gains tend to have the property that step responses are shaped into overdamped, viz., no oscillations; however, the settling time is too large. Hence, *HF* gains should be appropriately set to suppress

oscillatory motions while good tracking performance is maintained. (for reference in basic design, all tilt angles results are provided in Appendix B).

4.3.3. Extension to parametric study for control improvement when the probability function is given

In this section, we addressed an improvement of nominal model performance problem when the probability function is given. In actual flight, an existence of uncertainties in the system or the environments, or pilot interaction with the aircraft system is uncontrollable factors. In particular, those realistic environment modelling are difficult to model and incorporate with McART3 systems. However, if the probability of the models is different from model to model, then we have no need to use the same weighting function, and it is reasonable to use the same formed weighting function with different gains. The “different gains” can represent the different probability which denote as C_N for nominal model and C_{P_i} for i -th perturbed model. For example, if the 1st perturbed model has just half possibility compared to the nominal model and the 2nd perturbed model has only 25% possibility compared to the nominal model, then, it is reasonable to set the gains for the nominal, 1st and 2nd perturbed models (i.e., C_N , C_{P1} and C_{P2}) as 1, 0.5 and 0.25, respectively.

In contrast to the oscillatory reduction problem, we focus on an improvement of the nominal performance when the probabilistic weight is given. In particular, the magnitudes of the desire target sensitivity loop shapes is bounded by the inverse of different weighted probability gains (i.e., $1/|C_N W(j\omega)|$ or $1/|C_{P_i} W(j\omega)|$). If probability of the supposed perturbed models is set to be smaller than that of the nominal model, the improvement of the nominal performance is achieved in exchange of slightly poor performance for the perturbed models

The cost function in Eq. (4.2) is thus modified as follows:

$$f_{\text{cost}}(\mathbf{k}) = \begin{cases} f_{\text{cost}}^{\text{N}}(\mathbf{k}), & \text{if plant is Nominal model,} \\ f_{\text{cost}}^{\text{P1}}(\mathbf{k}), & \text{if plant is Perturbed-1 model,} \\ f_{\text{cost}}^{\text{P2}}(\mathbf{k}), & \text{if plant is Perturbed-2 model.} \end{cases}$$

where

(4.3)

$$\begin{aligned} f_{\text{cost}}^{\text{N}}(\mathbf{k}) &= \|C_{\text{N}}W(j\omega)S_{\text{N}}(j\omega)\|_{\infty} \\ f_{\text{cost}}^{\text{P1}}(\mathbf{k}) &= \|C_{\text{P1}}W(j\omega)S_{\text{P1}}(j\omega)\|_{\infty} \\ f_{\text{cost}}^{\text{P2}}(\mathbf{k}) &= \|C_{\text{P2}}W(j\omega)S_{\text{P2}}(j\omega)\|_{\infty} \end{aligned}$$

This formulation attempt to improve the nominal model performance. By setting coefficient C_{N} to unity while the perturbation models coefficient $C_{\text{P-1}}$ and $C_{\text{P-2}}$ are gradually decreased, we designed CAS gains for the lateral-directional motions. In particular, the designed CAS gains at clean configuration, which are shown in Table 4.4, indeed improve the nominal model performance while the performance output of the perturbed model is degraded which confirms through Figure 4.5. The parametric study for nominal control performance improvements in the other tilt angles are also investigated. However, the control performance improvement cannot be expected because the obtained CAS gains are almost the same.

Table 4.2. (a) Admissible CAS gain regions, CAS gains in 4.6), and optimized CAS controller gains using our method. [Basic design - lateral directional motion]

Tilt Angle	Admissible CAS gain domains(K_{lat})			Robust weighting function		
	$k_{p\phi}$	$k_{i\phi}$	$[k_{p\phi}, k_{i\phi}]$	$[k_{p\phi}, k_{i\phi}]$	$(1/W_{Nominal})$	$\ W(j\omega)S(j\omega)\ _{\infty}$
			JAXA	PSO	$[\text{makeweight}(DC, \omega_c, HF)]$	
CLN	[0,-100]	[0,-50]	[-100, -50]	[-43.64, -38.01]	$\text{makeweight}(1\text{e-}6, 0.8, 1.1)$	0.9664
0	[0,-100]	[0,-50]	[-100, -50]	[-73.83, -44.81]	$\text{makeweight}(1\text{e-}6, 0.8, 1.15)$	0.9628
15	[0,-100]	[0,-50]	[-100, -50]	[-64.75, -47.91]	$\text{makeweight}(1\text{e-}6, 0.6, 1.45)$	0.9918
30	[0,-120]	[0,-50]	[-88, -50]	[-58.95, -50.00]	$\text{makeweight}(1\text{e-}6, 1.2, 5.60)$	0.9761
50	[0,-80]	[0,-50]	[-80, -50]	[-18.37 -44.50]	$\text{makeweight}(1\text{e-}6, 1.1, 3.2)$	0.9613
70	[0,-50]	[0,-40]	[-50, -40]	[-22.70, -38.10]	$\text{makeweight}(1\text{e-}6, 0.42, 1.47)$	0.9918
90	[0,-50]	[0,-40]	[-50, -40]	[-37.96, -34.74]	$\text{makeweight}(1\text{e-}6, 0.25, 1.44)$	0.9670

Table 4.2. (b) Admissible CAS gain regions, CAS gains in 4.6), and optimized CAS controller gains using our method. [Basic design - lateral directional motion]

Tilt Angle	Admissible CAS gain domains(K_{lat})			Robust weighting function		
	$k_{p\phi}$	$k_{i\phi}$	$[k_{p\phi}, k_{i\phi}]$	$[k_{p\phi}, k_{i\phi}]$	$(1/W_{Nominal})$	$\ W(j\omega)S(j\omega)\ _{\infty}$
			JAXA	PSO	$[\text{makeweight}(DC, \omega_c, HF)]$	
CLN	[0,-100]	[0,-50]	[-100, -50]	[-43.64, -38.01]	$\text{makeweight}(1\text{e-}6, 0.8, 1.1)$	0.9664
0	[0,-100]	[0,-50]	[-100, -50]	[-73.83, -44.81]	$\text{makeweight}(1\text{e-}6, 0.8, 1.15)$	0.9628
15	[0,-100]	[0,-50]	[-100, -50]	[-64.75, -47.91]	$\text{makeweight}(1\text{e-}6, 0.6, 1.45)$	0.9918
30	[0,-120]	[0,-50]	[-88, -50]	[-58.95, -50.00]	$\text{makeweight}(1\text{e-}6, 1.2, 5.60)$	0.9761
50	[0,-80]	[0,-50]	[-80, -50]	[-18.37 -44.50]	$\text{makeweight}(1\text{e-}6, 1.1, 3.2)$	0.9613
70	[0,-50]	[0,-40]	[-50, -40]	[-22.70, -38.10]	$\text{makeweight}(1\text{e-}6, 0.42, 1.47)$	0.9918
90	[0,-50]	[0,-40]	[-50, -40]	[-37.96, -34.74]	$\text{makeweight}(1\text{e-}6, 0.25, 1.44)$	0.9670

Table 4.2. (c) Admissible CAS gain regions, CAS gains in 4.6), and optimized CAS controller gains using our method. [Extension design - lateral directional motion]

Tilt Angle	Admissible CAS gain domains(K_{lat})			Oscillatory suppressing CAS		
	$[k_{p\phi}, k_{i\phi}]$			$[k_{p\phi}, k_{i\phi}]$		
	$k_{p\phi}$	$k_{i\phi}$	JAXA	PSO	weighting function ($1/W_{Nominal}$) [makeweight(DC, ω_c, HF)]	$\ W(j\omega)S(j\omega)\ _{\infty}$
CLN	[0,-100]	[0,-50]	[-100, -50]	[-30.50, -22.28]	makeweight(1e-6, 0.6 , 1.05)	0.9932
0	[0,-100]	[0,-50]	[-100, -50]	[-54.49, -44.96]	makeweight(1e-6, 1.0 , 1.1)	0.9813
15	[0,-100]	[0,-50]	[-100, -50]	[-41.83, -26.16]	makeweight(1e-6, 0.4 ,1.21)	0.9975
30	[0,-120]	[0,-50]	[-88, -50]	[-41.35, -19.11]	makeweight(1e-6, 0.5 ,1.7)	0.9761
50	[0,-80]	[0,-50]	[-80, -50]	[-41.17 -18.64]	makeweight(1e-6, 0.2 , 1.67)	0.9728
70	[0,-50]	[0,-40]	[-50, -40]	[-40.01, -36.62]	makeweight(1e-6, 0.1 ,1.47)	0.9925
90	[0,-50]	[0,-40]	[-50, -40]	[-37.68, -34.46]	makeweight(1e-6, 0.2 ,1.44)	0.9936

Table 4.3. McART3 given probability coefficients for parametric study

Optimization routines	Given probability coefficients		
	C_N	C_{P-1}	C_{P-2}
1 st optimization	1	1	1
2 nd optimization	1	0.8	0.8
3 rd optimization	1	0.5	0.5
4 th optimization	1	0.2	0.2

Table 4.4. CAS controller improvement using probability density coefficients

Lateral directional motion						
Tilt Angle	$[C_N]$	C_{P-1}	C_{P-2}	$[k_{p\phi}, k_{r\phi}]_{\text{PSO}}$	$\ W(j\omega)S(j\omega)\ _{\infty}$	Improvement
CLN	[1	1	-]	[-43.64, -38.01]	0.9664 [P1]	Success
	[1	0.8	-]	[-43.92, -35.95]	0.9425 [N]	
	[1	0.5	-]	[-44.21, -32.39]	0.9390 [N]	
	[1	0.2	-]	[-43.55, -28.03]	0.9350 [N]	

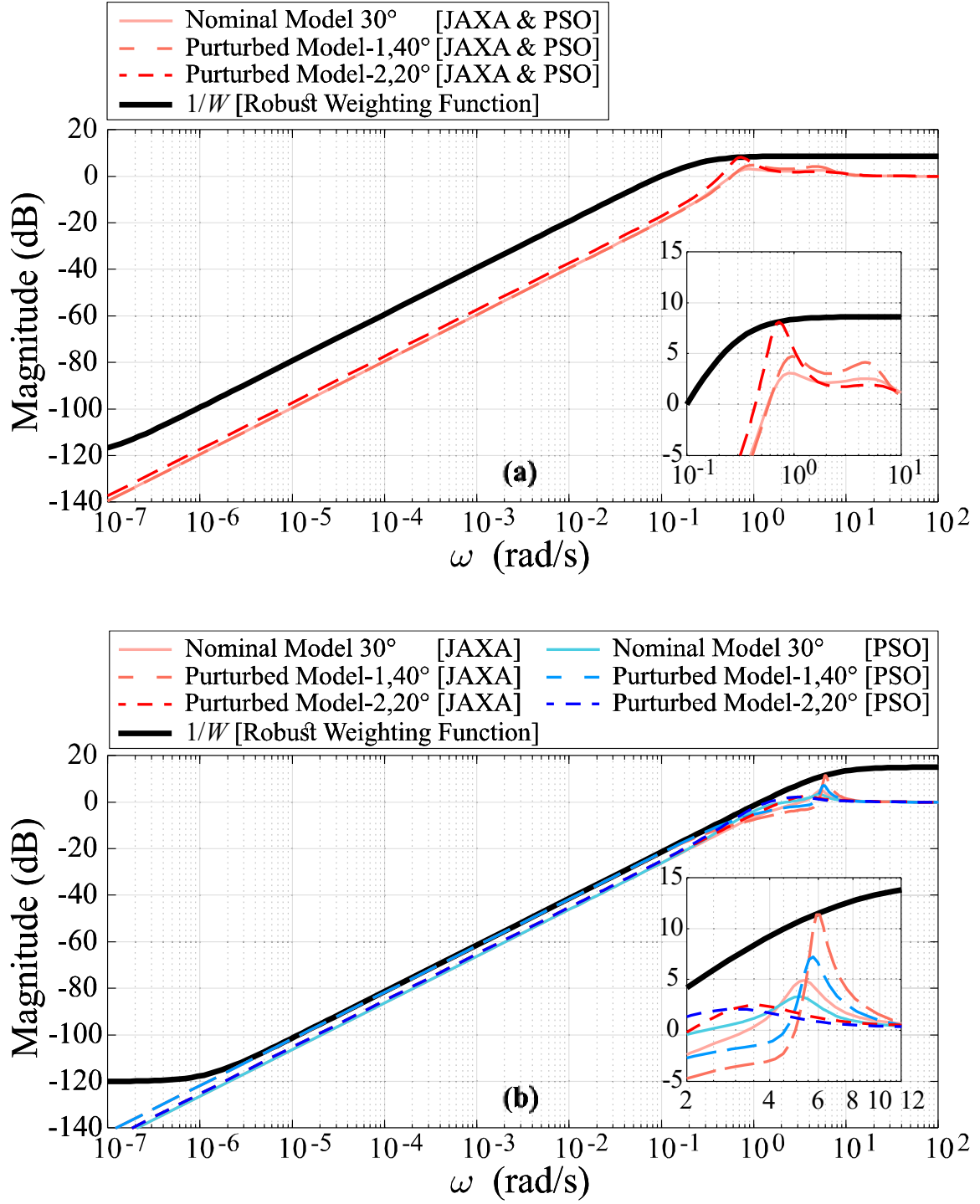


Fig. 4.2. Gain plots of sensitivity functions with CAS gains in 4.6), optimized gains in Table 4.2 (a) and (b), and $1/|W(s)|$ (Close-look are given in the boxes.) (a) $\tau_\omega = 30^\circ$ [lon. motion] (b) $\tau_\omega = 30^\circ$ [lat.-dir. motion].

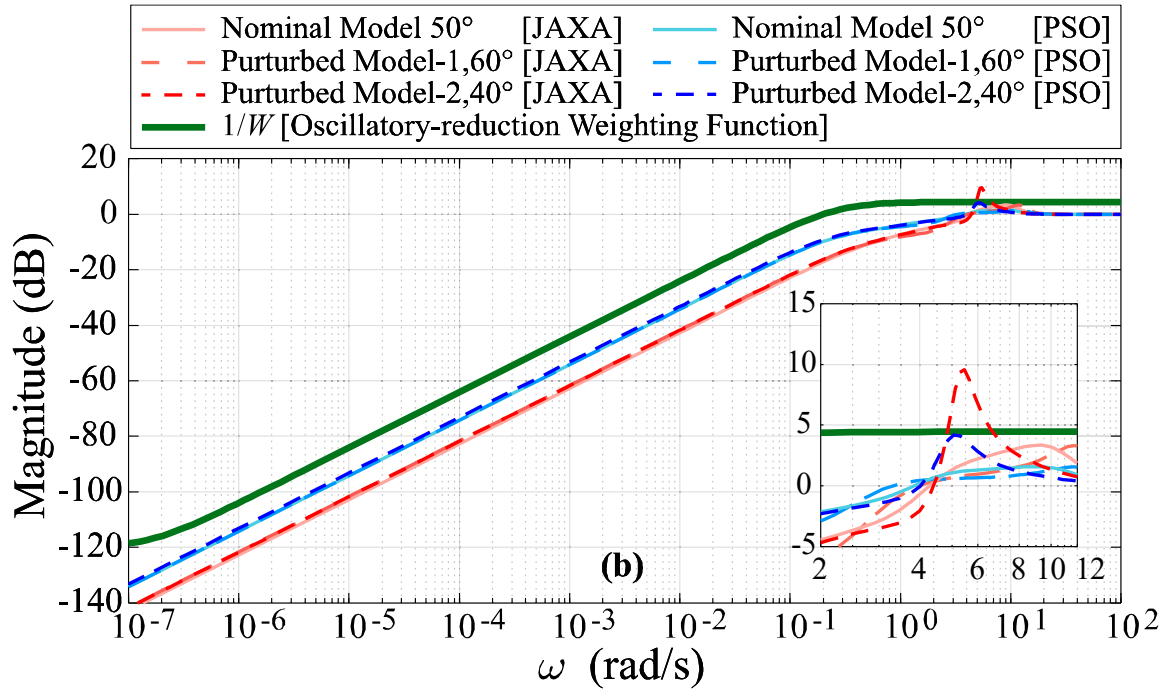
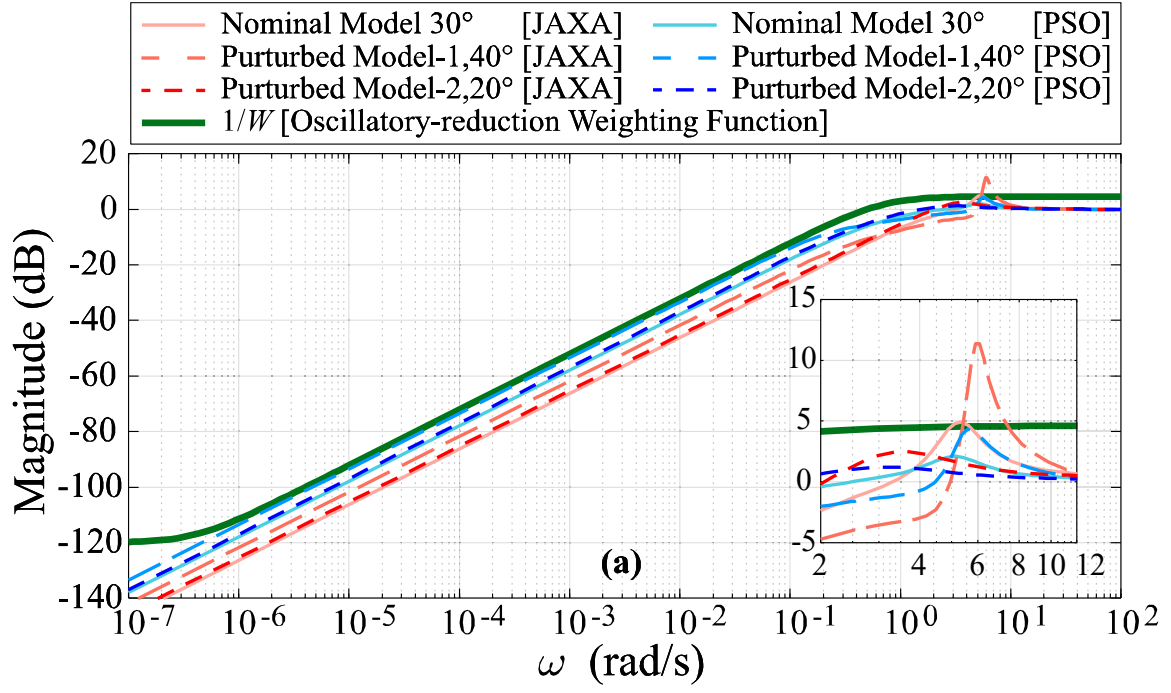


Fig. 4.3. Gain plots of sensitivity functions with CAS gains in 4.6), optimized gains in Table 4.2 (c), and $1/|W(s)|$ (Close-look figures around max peak gains are given in the boxes.) (a) $\tau_\omega = 30^\circ$ and (b) $\tau_\omega = 50^\circ$ [lat.-dir. motions].

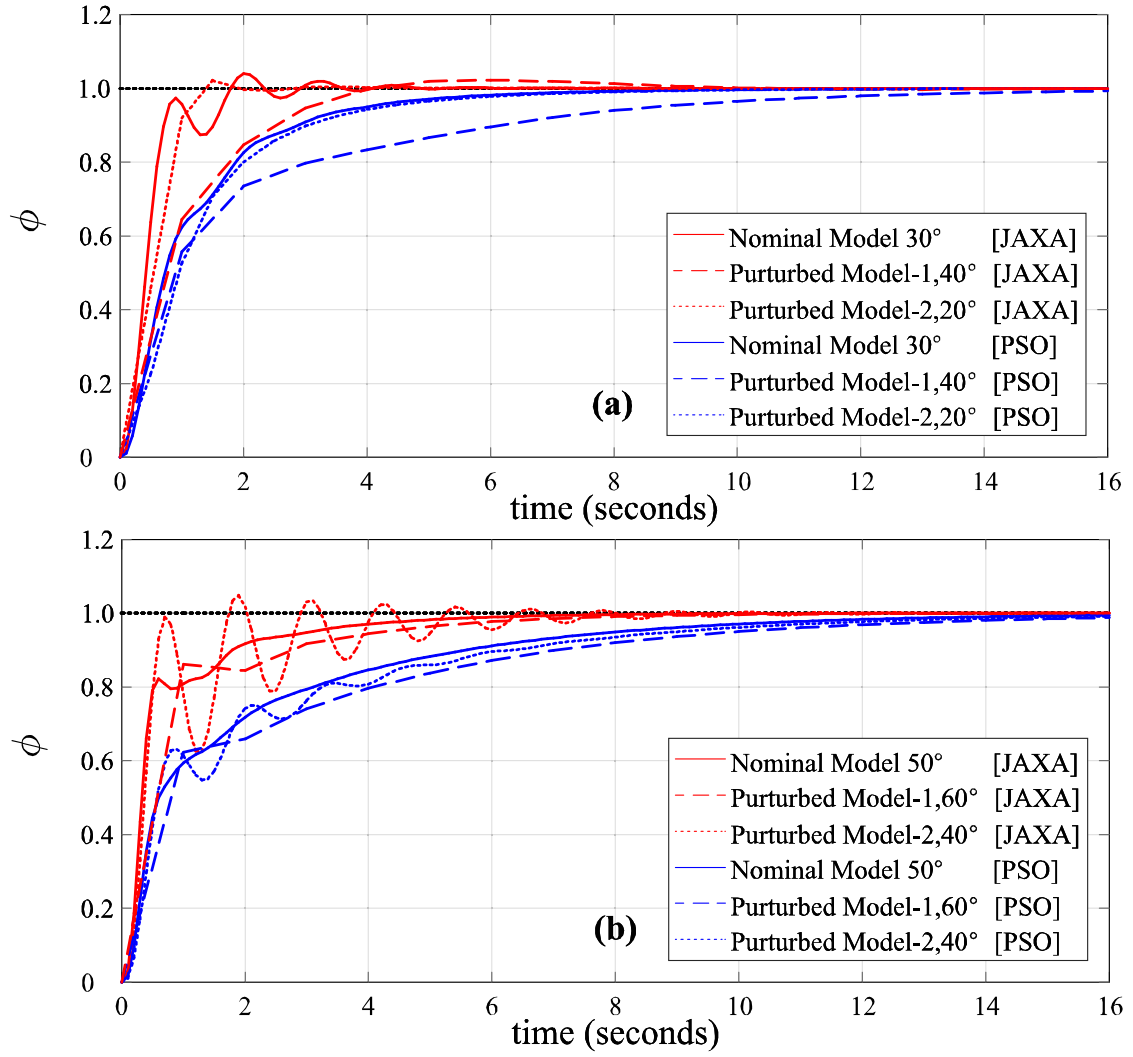


Fig. 4.4. Step responses of using oscillatory suppression CAS gains in Table 4.2(c) at (a) $\tau_\omega = 30^\circ$ and (b) $\tau_\omega = 50^\circ$ [lat.-dir. motions].

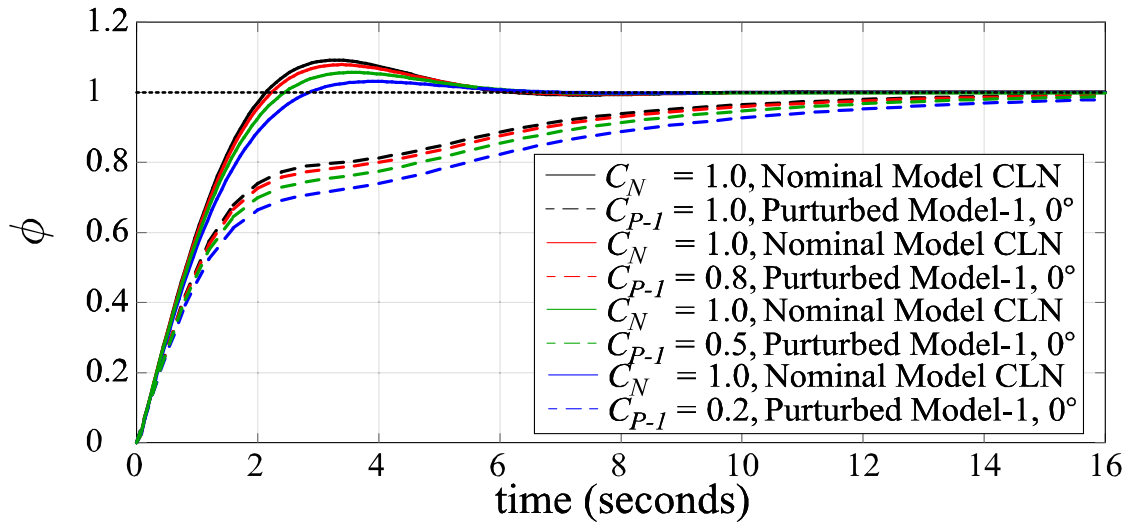


Fig. 4.5. Step responses at clean configuration using CAS gains from parametric study in table 4.4 [lat.-dir. motions].

4.3.4. Nonlinear Flight Simulation

To confirm the applicability of our oscillatory suppressing CAS gains which successfully designed in linear time in-variant domain, human-in-the-loop flight simulations; using nonlinear equations to calculate McART3 motions, are conducted. In the simulations, we particularly focus on only tracking performance of lateral-directional motion between roll angles and their commands. To do that, lateral-directional CAS gains are set as Table 4.1(c) while longitudinal CAS gains are set as the same as 4.6).

The flight simulations are conducted under normal condition as shown in Figure 4.6 as well as wind gust conditions as shown in Figure 4.7 which given by Dryden model. In the figures, terms “eas” and “vgs” denote equivalent airspeed and ground speed in m/s. where the difference between them represents wind gust speed in m/s. Vertical takeoff time is denoted by inverse black triangle symbol, CAS engagement time is denoted by inverse white triangle symbols, and vertical landing time is denoted by black diamond symbol. The CAS was engaged from just after takeoff until landing. The terms “clean” denote that McART3 fly in airplane mode with flaperons being retracted. In converse, tilt angle at 0 degree without the “clean” term means that McART3 fly in airplane mode with flaperons being extended.

It is confirmed that our designed CAS gains worked well throughout the flight simulation. McART3 can fly safely in helicopter mode, airplane mode, and transition in nominal conditions as well as slightly off-nominal conditions. In particular, roll angle faithfully follows their commands in all tilt angles which represent good tracking performance in both with and without wind gust conditions. The oscillations motions are barely found in roll angles as expected and slightly slow responses are apparently found. This confirms the applicability of our designed gains which are consistent with an example in Figure 4.4.

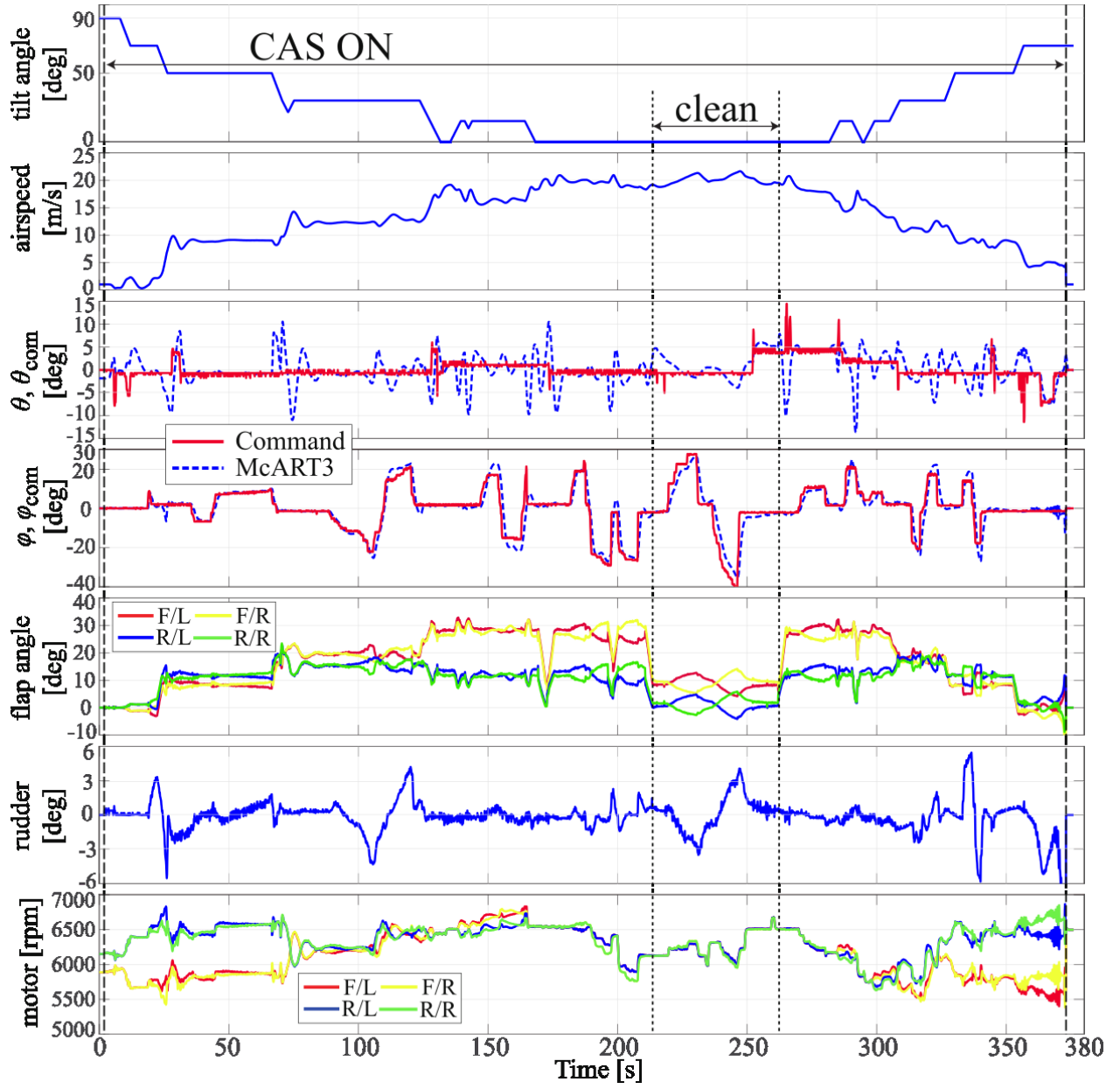


Fig. 4.6. Time history of full conversion flight under normal condition.

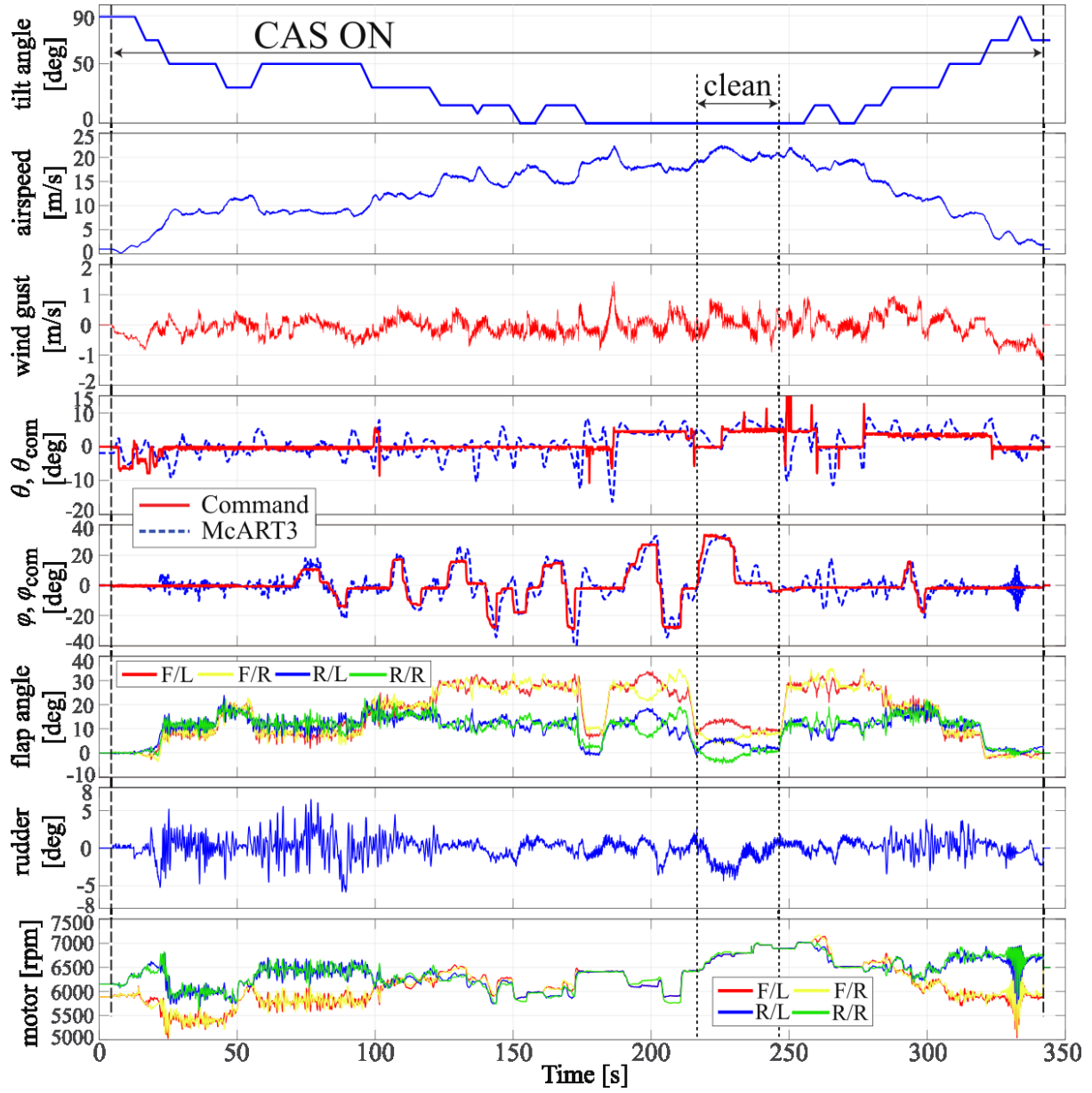


Fig. 4.7. Time history of full conversion flight under wind gust condition.

4.4. Chapter summary

To address existing design methods for Quad Tilt Wing Unmanned Aerial Vehicle (QTW-UAV), i.e., oscillatory motions and a large numerical complexity in controller gain design, this chapter proposes a method for Control Augmentation System (CAS) design with the application of Particle Swarm Optimization (PSO). By analogy with the previously used method, multiple model approach is similarly applied to realize controller gains robustness against the plants modeling errors. In contrast, the design requirements are given in frequency domain, to be more specific, weighted sensitivity functions from attitude command to attitude error is required to satisfy an H_∞ norm constraint.

We first investigate the applicability of our CAS design method for McART3 in which the target sensitivity function is set as the one whose holds the maximum peak gain, among the nominal and perturbed models using the gains in an existing paper. As a result, it is confirmed that our obtained gains are robustly optimized as well as guarantee the worst case performances in all tilt angles.

Then, as an extension, we address oscillatory suppressing CAS design in lateral-directional motion. In exchange for slightly slow responses, oscillatory suppressing CAS gains are confirmed. Next, the improvement of the performance of nominal model is further investigated when the probability functions are given.

To confirm the applicability of our oscillatory suppressing CAS gains which successfully designed in linear time invariant domain, Nonlinear flight simulations are conducted under both normal and wind gust conditions. The designed gains worked well in both environments. In particular, roll angle faithfully follows their commands in all tilt angles which represent good tracking performances are achieved.

4.5. References

- 4.1) Cox, T. H., Nagy, C. J., Skoog, M. A., and Somers, I. A.: Civil UAV Capability Assessment, NASA TR, Dec. 2004.
- 4.2) Hassanalian, M. and Abdelkefi, A.: Classifications, applications, and design challenges of drones: A review, *Progress in Aerospace Sciences*, **91** (2017), pp. 99–131.
- 4.3) Unmanned Aircraft Systems Roadmap:2005–2030, U.S. Dept. of Defense, Office of the Secretary of Defense, 2005, https://www.fas.org/irp/program/collect/uav_roadmap2005.pdf (accessed October 20, 2013).
- 4.4) Muraoka, K., Okada, N., Kubo, D., and Sato, M.: Transition Flight of Quad Tilt Wing VTOL UAV, 28th International Congress of the Aeronautical Sciences, ICAS 2012-11.1.3, Bonn, Germany, 2012.
- 4.5) Sato, M. and Muraoka, K.: Flight Controller Design and Demonstration of Quad-Tilt-Wing Unmanned Aerial Vehicle, *Journal of Guidance, Control, and dynamics*, **38** (2015), pp. 1071–1082.
- 4.6) Sato, M. and Muraoka, K.: Flight Controller Design of Quad Tilt Wing Aircraft and Flight Tests - Basic Controller Using PID Control Scheme -, 52st Aircraft Symposium, Nagasaki, Japan, 2014 (in Japanese).
- 4.7) Yavari, S., Zoj, M. J. V., Mokhtarzade, M., Mohammadzadeh, A.: Comparison of Particle Swarm Optimization and Genetic Algorithm in Rational Function Model Optimization, *International Archives of the Photogrammetry, Remote Sensing and Spatial Information Sciences*, Volume XXXIX-B1 (2012), pp. 281–284.
- 4.8) Skogestad, S. and Postlethwaite, I.: *Multivariable Feedback Control Analysis and Design Second Edition*, John Wiley & Sons Press, New York, 2001, pp. 55–57.
- 4.9) Kennedy, J and Eberhart, R.C.: Particle Swarm Optimization, Neural Networks, 1995. Proceedings., IEEE International Conference on. Perth, WA, Australia, 1995.
- 4.10) Maruta, I., Kim, T. and Sugie, T.: Fixed-structure H_∞ youtubecontroller synthesis: A meta-heuristic approach using simple constrained particle swarm optimization, *Automatica*, **45** (2009) pp. 553–559.
- 4.11) Banks, A., Vincent, J., and Anyakoha, C.: A review of particle swarm optimization. Part I: Background and development. *Natural Computing*, **6** (2007), pp. 467–484.
- 4.12) Sedlacek, K., & Eberhard, P. (2006).: Using augmented Lagrangian particle swarm optimization for constrained problems in engineering``>Using augmented Lagrangian particle swarm optimization for constrained problems in engineering. *Structural and Multidisciplinary Optimization*, **32** (2006), pp. 277–286.
- 4.13) Latha, K. , Rajinikanth, V. and Surekha, P. M.: PSO-Based PID Controller Design for a Class of Stable and Unstable Systems, *ISRN Artificial Intelligence*, **2013** (2013).
- 4.14) Alfi, A. and Modares, H.: System identification and control using adaptive particle swarm optimization, *Applied Mathematical Modelling*, **35** (2011), pp. 1210–1221.

Chapter 5

Hardware Implementation

Chapter Overview

This chapter shows the QTW-UAV hardware study. In attempt to construct QTW-UAV, the overall aircraft design process is implement through SolidWorks programming such as wings, fuselage, rudder, tilting mechanism by considering the particular requirements. The Next, the manufacturing and assembling processes are demonstrated. The flight control frameworks are designed based on the requirements of multitasking control process as shown as the last part of the chapter. Flight programming processes are divided into four major parts; ground station, central flight controller, mechanism driver and actuators. The flight control unit are developed through raspberry PI with C++ programing language to control the aircraft.

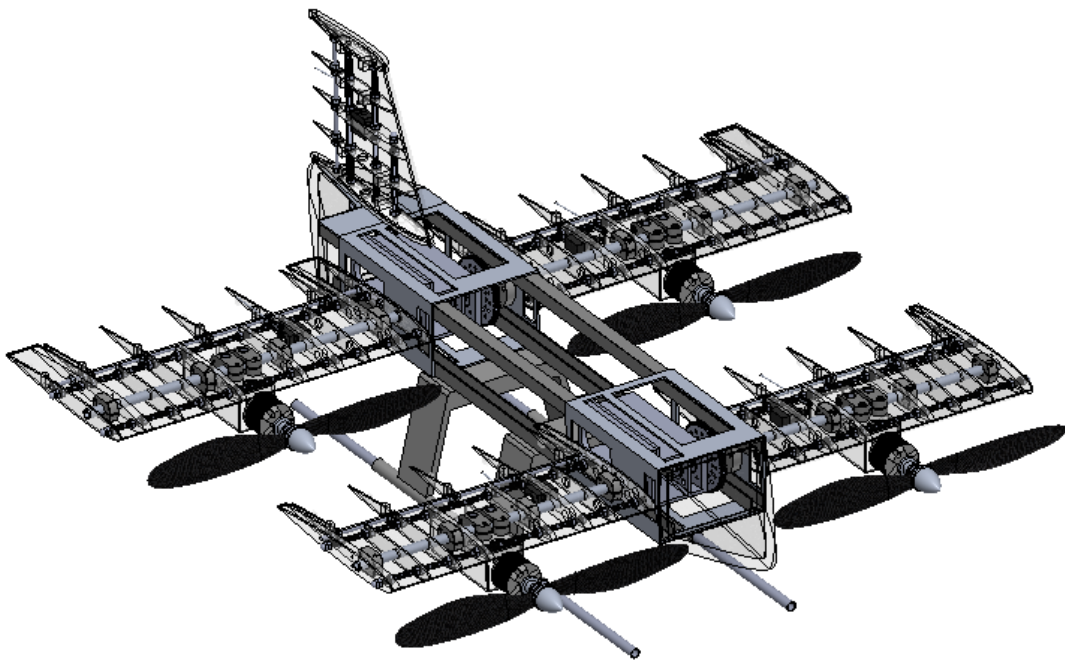


Fig. 5.1. QTW-UAV design prototype.

5.1. Structure design process

This section attempt to design the QTW-UAV. Based on Canard configuration, front wings are design to be smaller than the rare wings. The airplane is able to tilt both wings from 0 to 90-degree tilt angles to obtain thee configuration modes, that is ; airplane, helicopter and transition modes. The parts are particularly design to meets the requirements. Size of the aircraft is decided by the limited length of the wind tunnel cross section area which is 1 m. of length and height. Such that, the wing span is limited within those ranges. Therefore, the front wing span is design to be 800 mm. and the rare wing is design to be 840 mm. The weight of the aircraft is approximately 6.5 kg. The propulsion system uses four Li-Ho batteries. Figure 5.1, 5.2 and 5.3 demonstrate an overall structural design using SolidWorks Software as shown below.

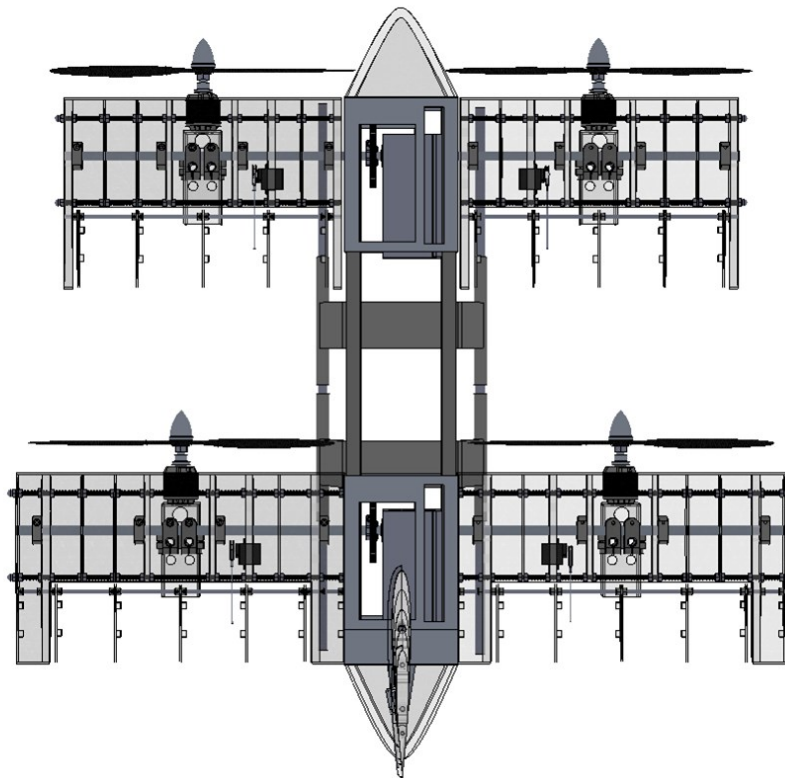


Fig. 5.2. QTW-UAV design (top-view).

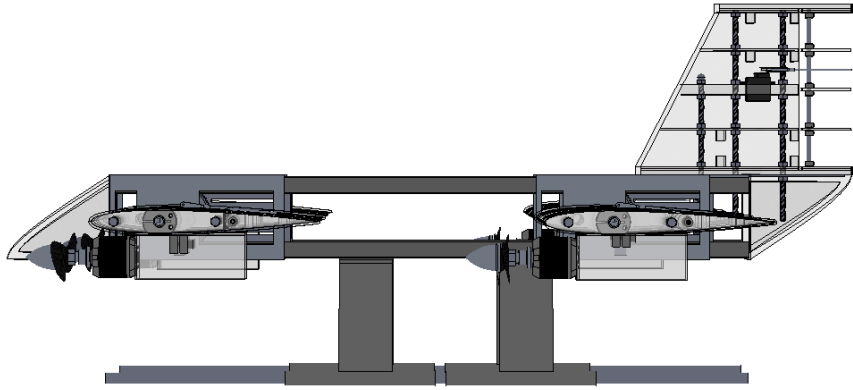


Fig. 5.3. QTW-UAV design (side-view).

5.1.1. Airfoils design

In this research, a simplest symmetric airfoil is used based on National Advisory Committee for Aeronautics (NACA). NACA 4-digit series foil is used as NACA 0008. The aerofoil profile contains maximum thickness 8% at 30% chord and maximum camber 0% at 0% chord.

Require velocity (v)=20 m/s, Chord width (l) = 0.2 m. and Kinematic Velocity of air at 20 degree (ν) = 1.5111e-5.

The Reynolds number (Re) is calculated from:

$$Re = \frac{vl}{\nu}$$

$$Re = \frac{20 \times 0.20}{1.5111E-5} = 264,708 \quad (5.1)$$

Therefore, the NACA 0008 airfoil polar coordinate at 500,000 is selected form UIUC database as shown in Figure.5.4. Figure 5.5 shows the selected airfoil profiles.

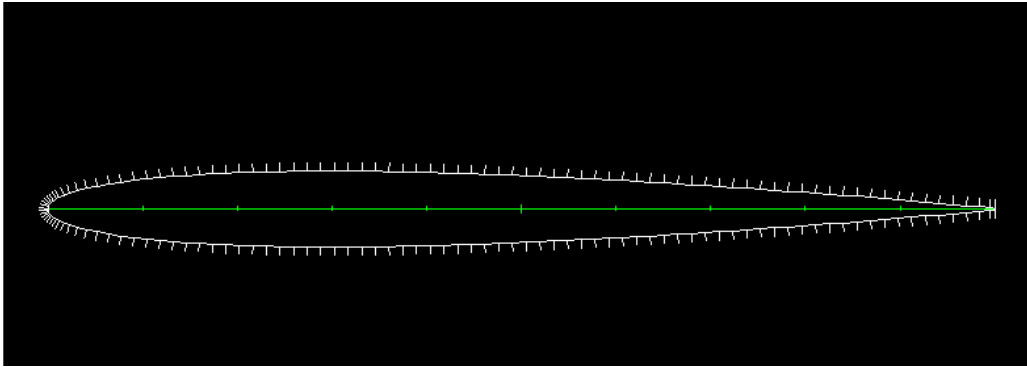


Fig. 5.4. NACA 0008 polar coordinate at $Re = 500,000$.

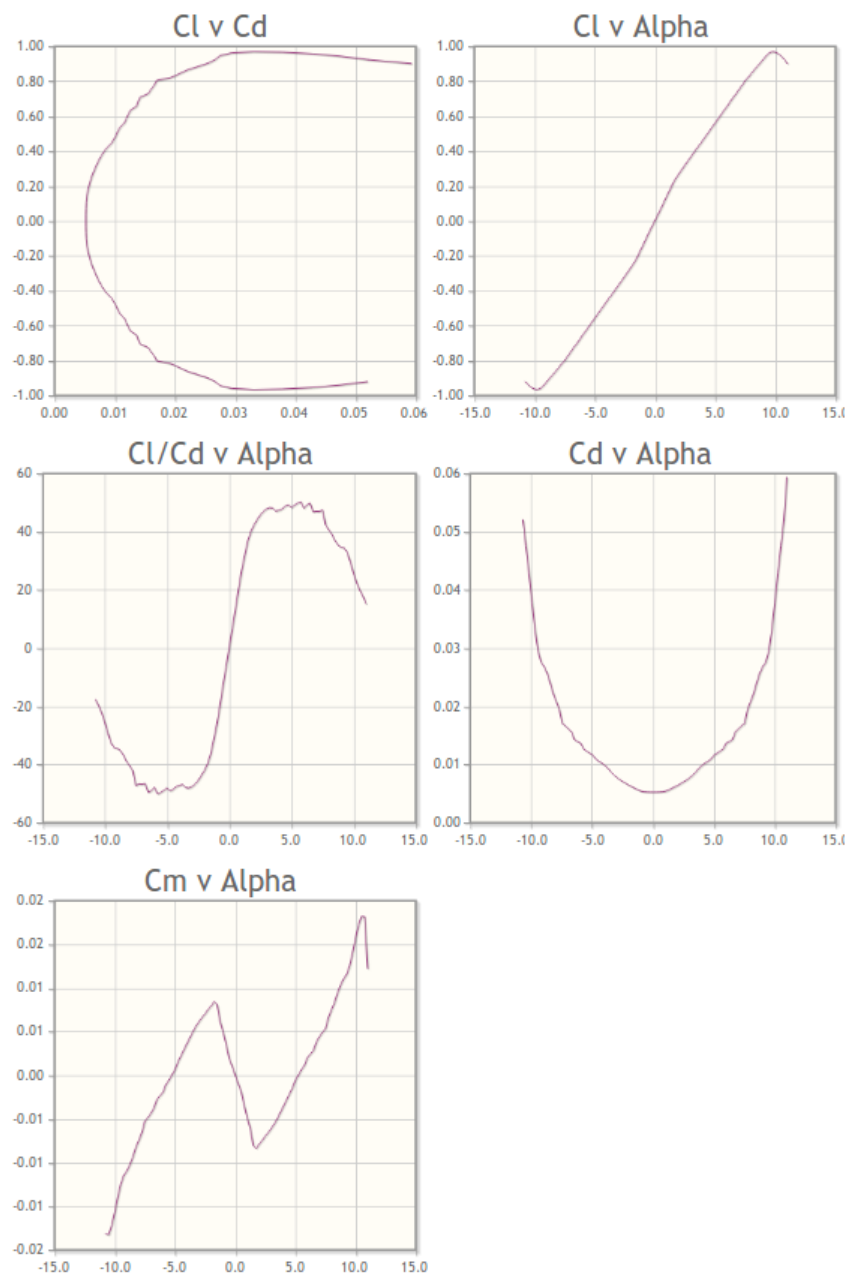


Fig. 5.5. Airfoil profile of NACA 0008 with Reynold number equal to 500,000.

5.1.2. Wing structure design

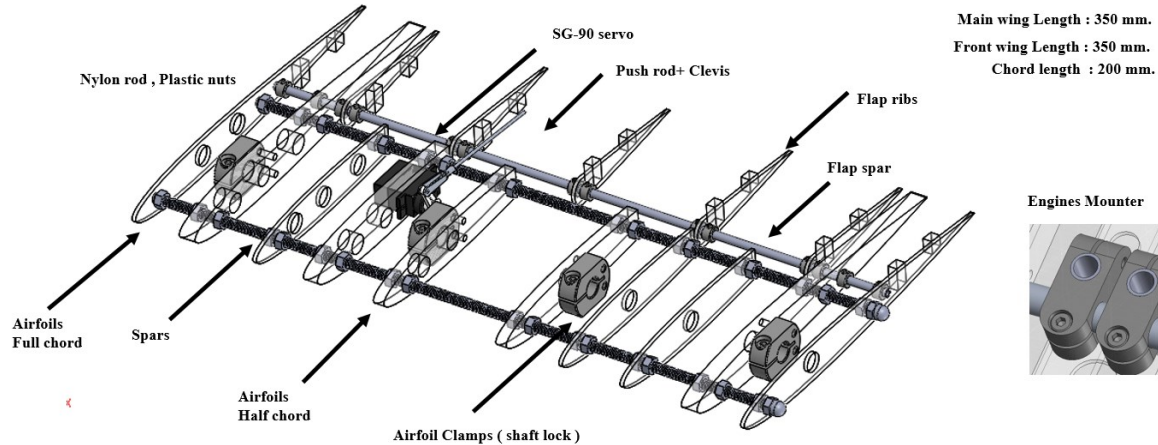


Fig. 5.6. Wing design.

The shape of the wings is selected by taking the speed range, wing span limitation, interactions mechanism with the fuselage into consideration. Airfoils are made by firstly design from CAD model and manufacturing with laser cutting machine. Laser cutting uses a high power laser beam to cut flat sheet of acrylic. The high precision laser vaporises a cut line through the ribs, leaving a 90-degree high quality cut edge finish.

Wing ribs consist of various airfoils with different thickness and length depend on its particular functions as shown in Figure 5.6. The ribs inside each wing connects to the multi spars (two nylon rods and one main aluminium shaft) which collectively provide the wing rigidity needed to enable the aircraft to fly safely. By being repeated at frequent intervals of airfoils while locking its position using double nylon bolts, those form a skeletal shape for the wing. The skin is finally adopt to this shape when stretched over the ribs.

5.1.3. Plain flap

Acrylic plain flaps type is employed as high-lift device used to increase the lift of an aircraft wing at a given airspeed. The flaps are mounted on the wing trailing. Flaps are used to lower the minimum speed at which the aircraft can be safely flown in airplane mode as well as control the aircraft motion. In particular, yawing moment is generated by aerodynamic forces on the flaperons due to propeller slipstream in helicopter mode. In airplane mode, pitching moment is generated by deflections of forward and aft flaperons, rolling moment is generated by opposite deflections of left and right flaperons.

Each flap connected to the wing using flap spar. By being repeated at frequent intervals of flaperons airfoils while locking its position using double aluminium clamps, those form a skeletal shape for the flaps as shown in Figure 5.7. The skin is adopt to this shape when stretched over those ribs.

5.1.4. Vertical tail design (Rudder)

On an aircraft, the rudder is design as a directional control surface which allows the pilot to control yaw about the vertical axis. In this design, a simplest symmetric airfoil which slightly large camber form the wing rib is used to construct rudder. NACA 4-digit series foil is used as NACA 0010. The airfoil profile contains maximum thickness 10% at 30% chord and maximum camber 0% at 0% chord. The airfoils sizes are designed in five different lengths from varying from 25 % to 100% size. The ribs inside each rudder connects to the multi spars as shown in Figure 5.8 (two nylon rods and one main aluminium shaft) which collectively provide the wing rigidity needed to enable the aircraft to create yawing moment. By being repeated at frequent intervals of airfoils while locking its position using double nylon bolts,

those form a skeletal shape for the wing. The skin is finally adopt to this shape when stretched over the ribs.

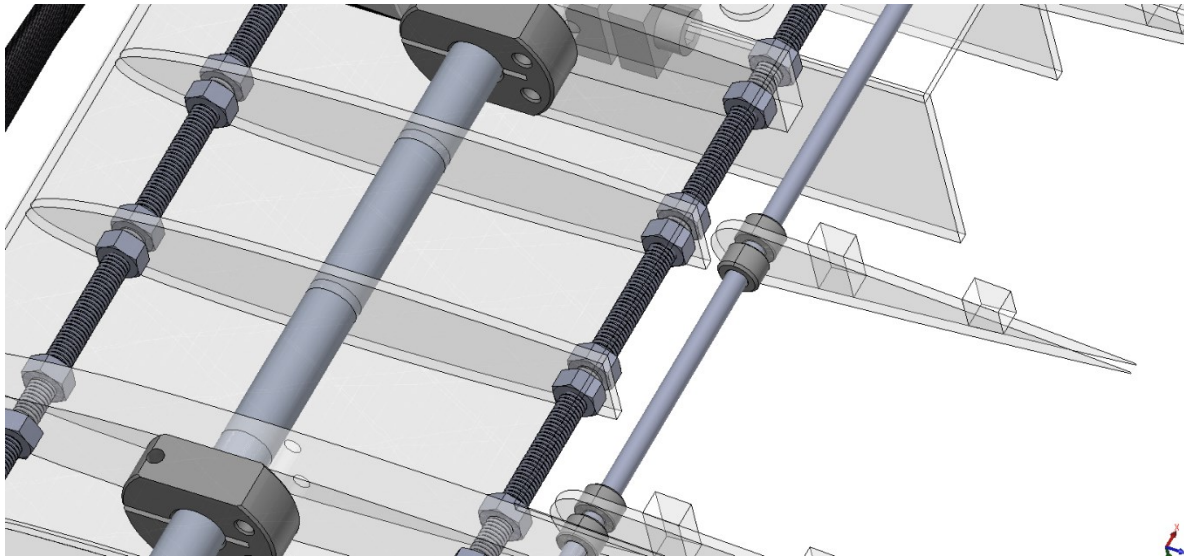


Fig. 5.7. Wing design.

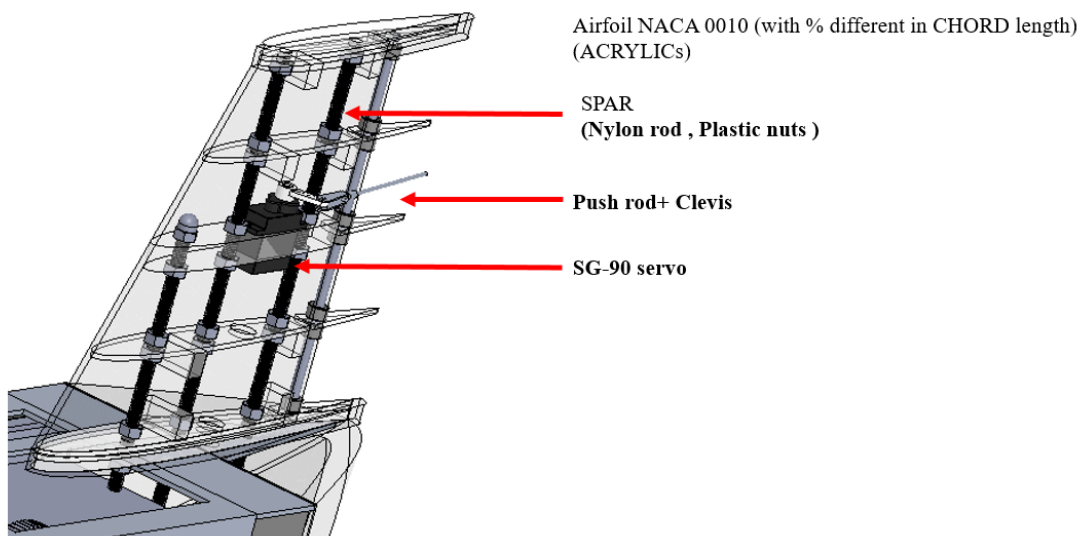


Fig. 5.8. Vertical tail design.

5.1.5. Fuselage and Gearboxes design

In tilting mechanism of the both front and rare wing. The BM-785HB Servo Gearbox with Hitec HS-785HB sail winch servo are used to generate a high-torque for wing

rotation as shown in Figure 5.9. When the servo is installed into the gearbox, the total amount of rotation is decreased by the ratio selected but the torque and precision is increased by the ratio. The lower the gear ratio, the more precision and torque it will provide but the speed and amount of rotation will be decreased. The BM-785HB can handle tremendous side loads with the dual ABEC precision ball bearings which support the hardened 3/8" stainless steel shaft. The main shaft is hollow aluminum with a .290" inner diameter to allow wires from devices to not tangle during multi-rotation movements. The brass pinion gear meshes in a high-grade 7075 aluminums 32 pitch hub gear which is fastened to the output shaft of the gearbox with a 3/8" clamping hub. Two gear boxes are linked together using 4 aluminum bar as a fuselage support structure as shown in Figure 5.10.

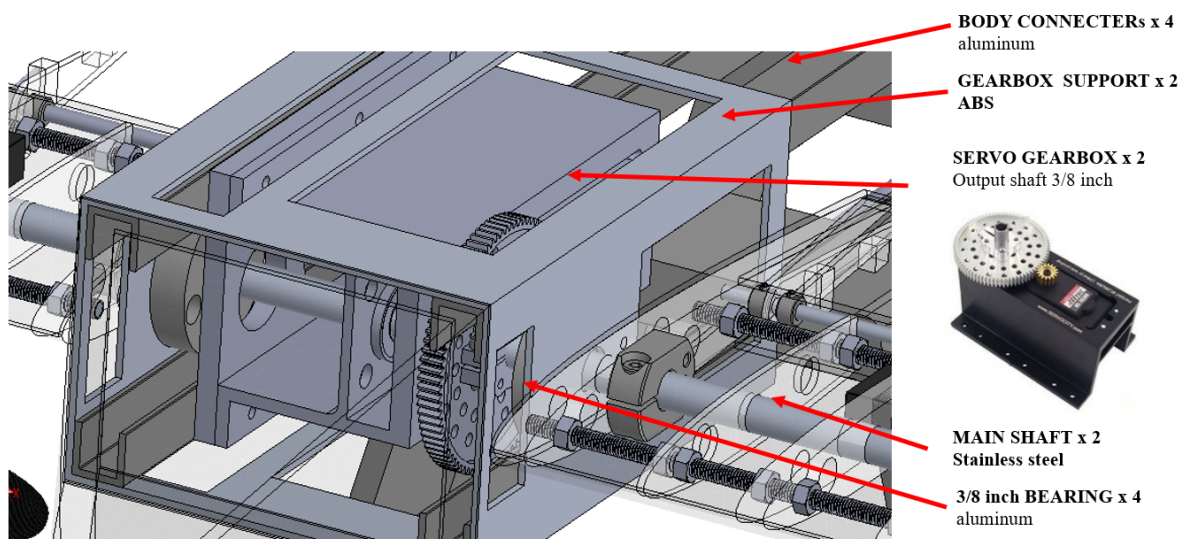


Fig. 5.9. Fuselage and tilting mechanism design.

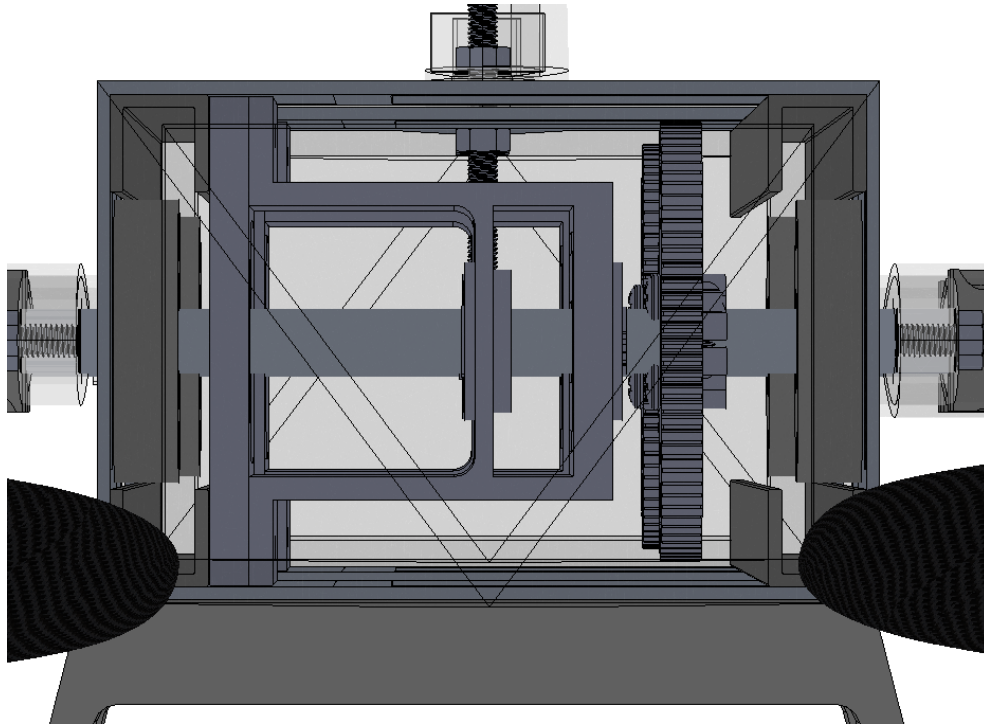


Fig. 5.10. Fuselage and tilting mechanism design.

5.1.6. Engines

To drive the aircraft, NTM Prop Drive Series EF-1 1300kv is selected as driving engines. The motor specification is listed as follows;

Model: NTM Prop Drive Series EF-1 1300kv

Kv: 1300rpm/v

Max current: 65A

Max Power: 500W @ 11.1v (3S) / 930W

@ 15v (4S)

Shaft: 5mm

Bullet-connector

ENGLINE : PROP DRIVE EF-1 x 4
PROPELLER : 10 inch x 5.5 pitch

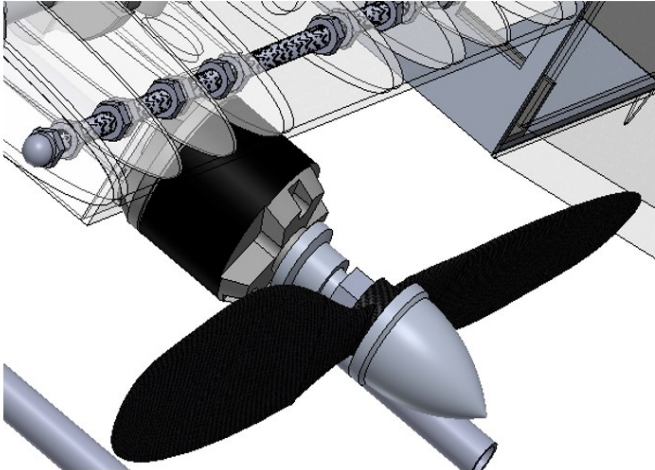


Fig. 5.11. Engines and propellers.

Prop Tests:

8x8 propeller 11.1v - 260W - 24A - 0.9kg thrust

8x8 propeller 14.8v - 560W - 38.8A - 1.45kg thrust

5.2. Manufacturing process

5.2.1. Mold making for control surface

For aircraft control surface manufacturing, 3D printer is used to print the all surface mold parts including main wings, flaps, rudder, vertical tail. The 2 mm. mold thickness making from Acrylonitrile butadiene styrene (ABS) is firstly applied to construct the molds, however, the molds reveal in severely fatigue as well as non-90 degrees cutting-edge due to the shrinkage. To solve this problem, the mold thickness is 5 mm making from ULTRAX filament to ensure the rigidity. Comparison between materials is shown in Figure.5.12

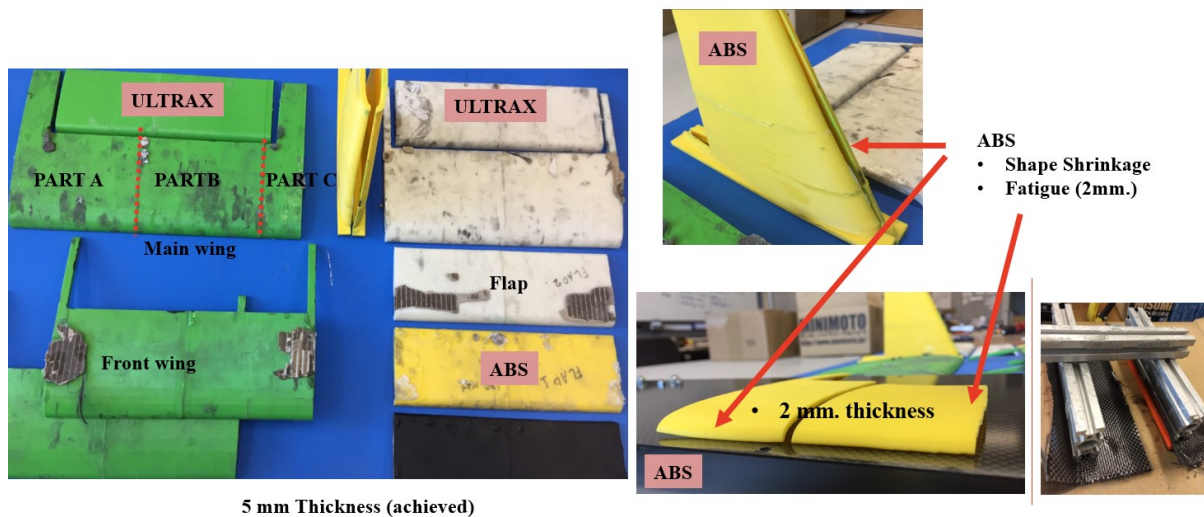


Fig. 5.12. Mold making for surface design using 3D-printer.

5.2.2. Control surface using carbon-fiber

The carbon fiber is selected as a surface material. To further explain the wing surface structure, the carbon-fiber keeps the reinforcement fibers separated so that they can be kept in maximum tensile (tension or stretching) strength. The reinforcement fibers carry the load. The resin keeps the fibers in place so they can maintain straightness and deliver their maximum strength. The resin also binds the fibers to the core. Therefore, a composite structure is really a mixture of critical components. When loads are applied to a wing, as an example, the majority of the stress occurs at the outer surfaces. To take advantage of this principle, a sandwich panel is designed with two working skins on the outside that are separated by a lightweight core. This type of design concentrates the strength in the area of high stress (outer surfaces) while reducing the weight in the area of low stress (inside the wing). List of require material is given bellows;

3k Carbon Fibre Cloth

Laminating Epoxy Resin

FAST Epoxy Hardener

PVA Mould Release Agent

Manufacturing procedure is given below;

Figure 5.13s. Shows the overall process of making carbon fiber surface. It can be divided into four main parts. (a) mould preparation, (b) main manufacturing process, (c) coating surface and final finishing surface. The process instruction is given below; In step (a): apply release agent to the mould, mix epoxy resin and hardener for the surface coat. In step (b): apply the surface coat of epoxy resin while the excessive fabric is cut. Next, lay carbon fabric into the mould and wet-out fabric. Then, apply additional layers of carbon fiber and leave to cure. In step (c): release the part and cover with epoxy at the outside wing surface. Finally, step (d): polishing surface using diamond glider and sand paper. Figure. 5.14 shows the weight comparison between each 3D printer parts and carbon fiber surface parts. The whole finishing surface weight is 0.99 kg.

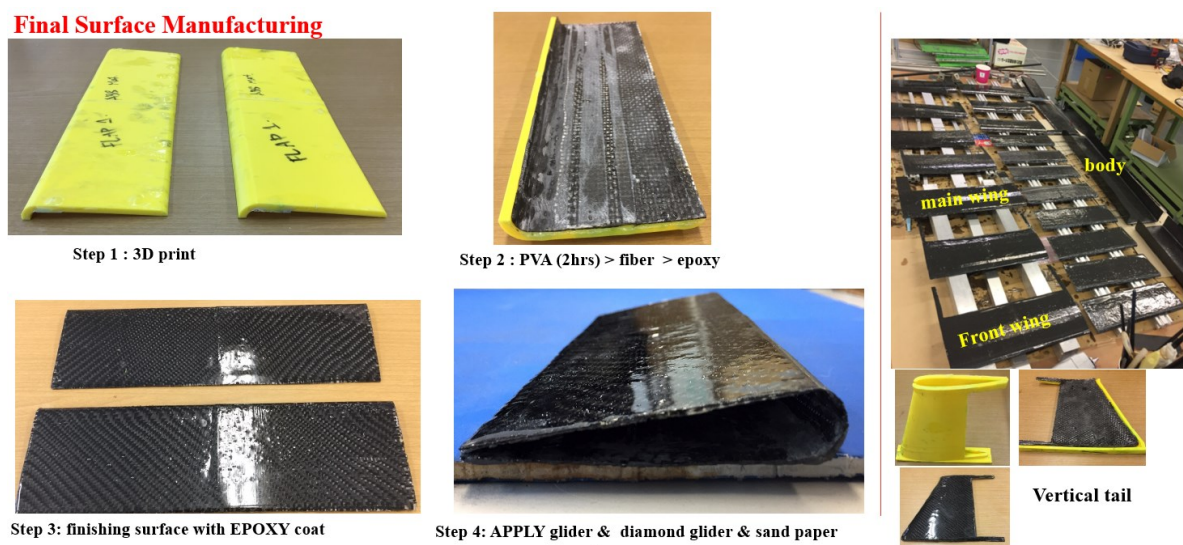


Fig. 5.13. Carbon fiber surface manufacturing.

Weight comparison

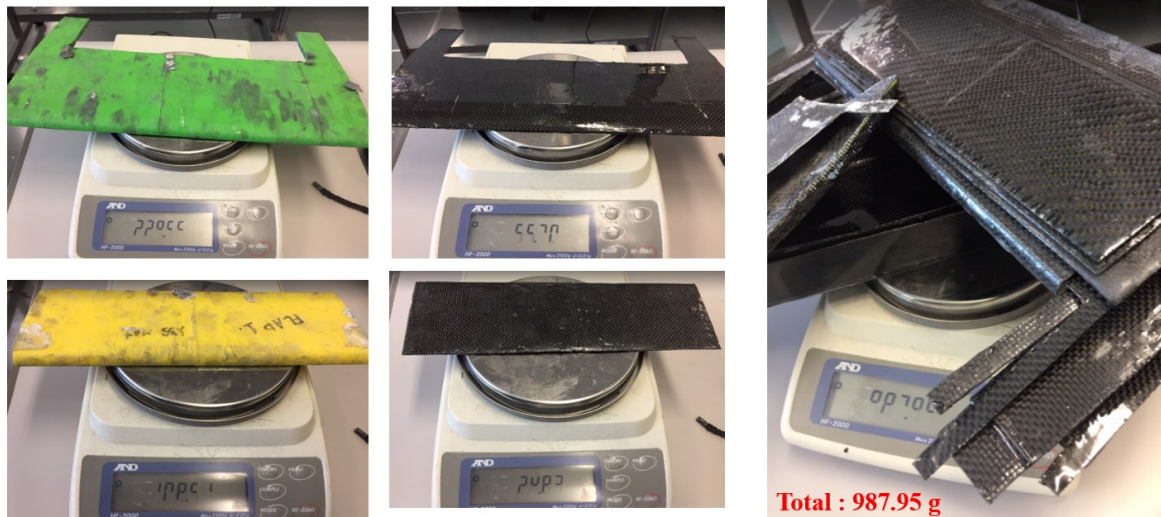


Fig. 5.14. Surface weight comparison.

The aircraft nose and tails and two gearbox support parts are constructed using rigid 3D-printers as shown in Figure 5.15 below.

3D printer parts

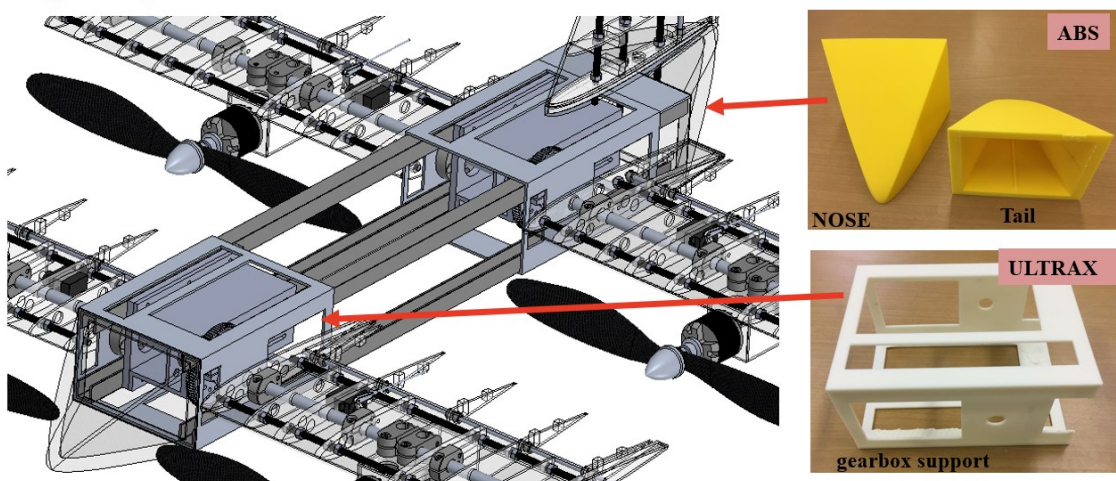


Fig. 5.15. 3D printer parts.



Fig. 5.16. Final QTW-UAV porotype.

5.3. Flight control design process and firmware design strategy

The flight control frameworks are designed based on the requirements of multitasking control process. Flight programming processes are divided into three major parts; ground station, central flight controller, mechanism driver and actuators. In ground control part, two modes are available for pilot to control the airplane. i.e., direct input keyboard using WiFi or remote control using radio frequency mode. The signal form ground station is sent to onboard central flight control unit. In particular, in QTW-UAV control, flaps and motors are required to separately operate in real-time as much as they can. Therefore, kernel based Operating System (OS) is required for multi-tasking process. The central flight control received commands from pilot and calculate the different flight operating condition for each actuator via mechanism drivers. To manage the protocol running in central flight control algorithm, distribute messaging protocols, viz. Zeromq are utilized to communicate between each unit. In actuator part, two protocols are used to communicate between sensor and actuator drivers that

is; SPI and I2C. Hardware such as motors, flaps, rudder and tilting mechanism are controlled using PWM technique. The overall flight control technique is illustrated in Figure 5.16.

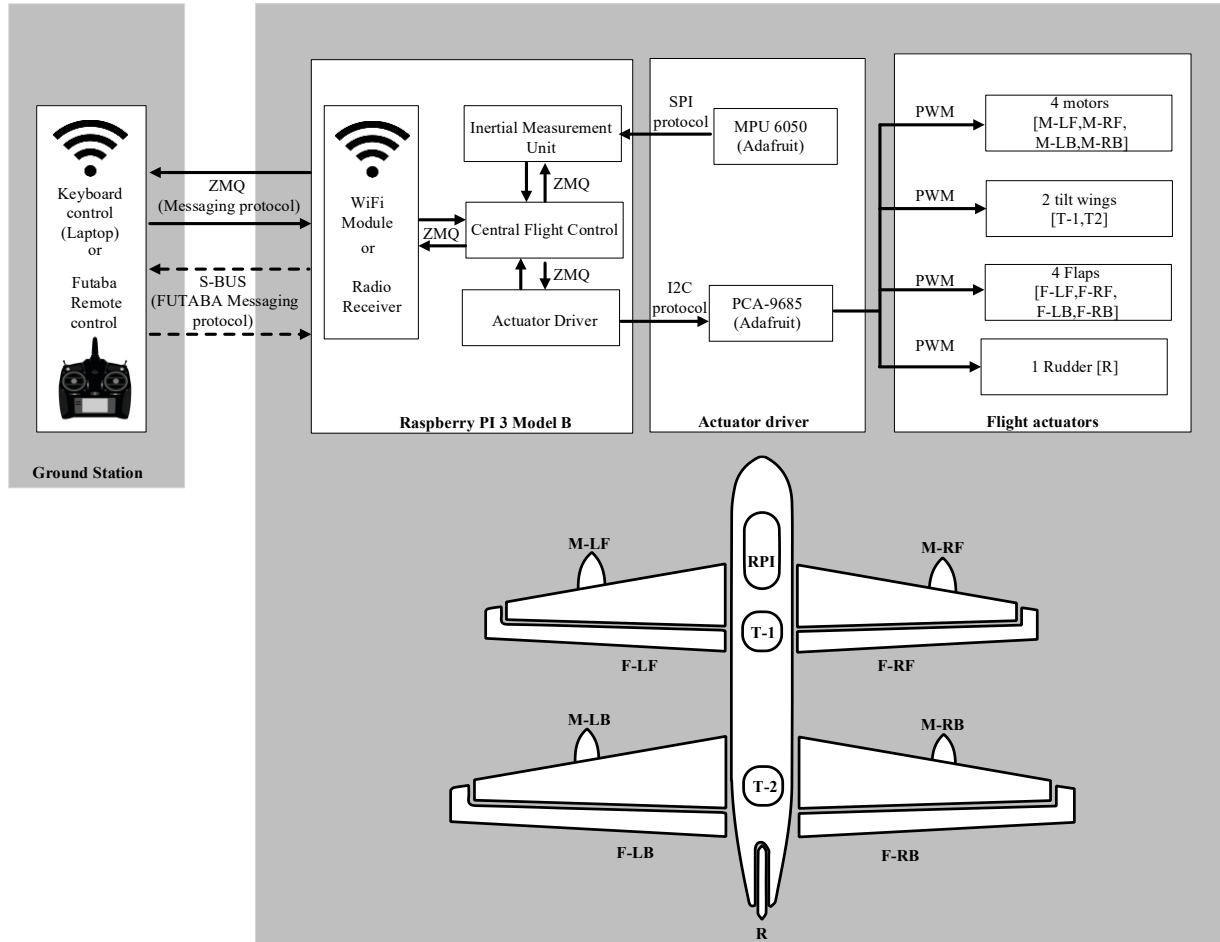


Fig. 5.17. QTW-UAV control schematic.

5.3.1. Flight control implementation

In flight control design process, the controller requirements features are describing as follows;

Requirement 1: real-time multi-tasking process scheduler

Requirement 2: support 11 GPIO pins

RPi (Raspberry Pi 3)

In control software implantation, it would be mandatory to be using a real-time kernel, which does exist for RPi. Most flight control boards split the work into at least two physical processors. One that reads IMU sensor values, integrates the result, computer error, and then computes commands. and only those tasks. That processor, typically referred to as a "controller" because it implements a control loop, has a very high performance requirement. The faster it can execute resulting in the more stable platform. The reason a real-time kernel is necessary. In this design process, the controllers are divided into another dedicated processor that accepts goals from a main processor. This means the dedicated controller processor only needs to do four things: accept commands from the main processor, read from sensors, multiply and add, and write out commands. This is where a Raspberry Pi would be a perfectly adequate choice. It is able to rapidly iterate and test, using a developer-friendly environment.

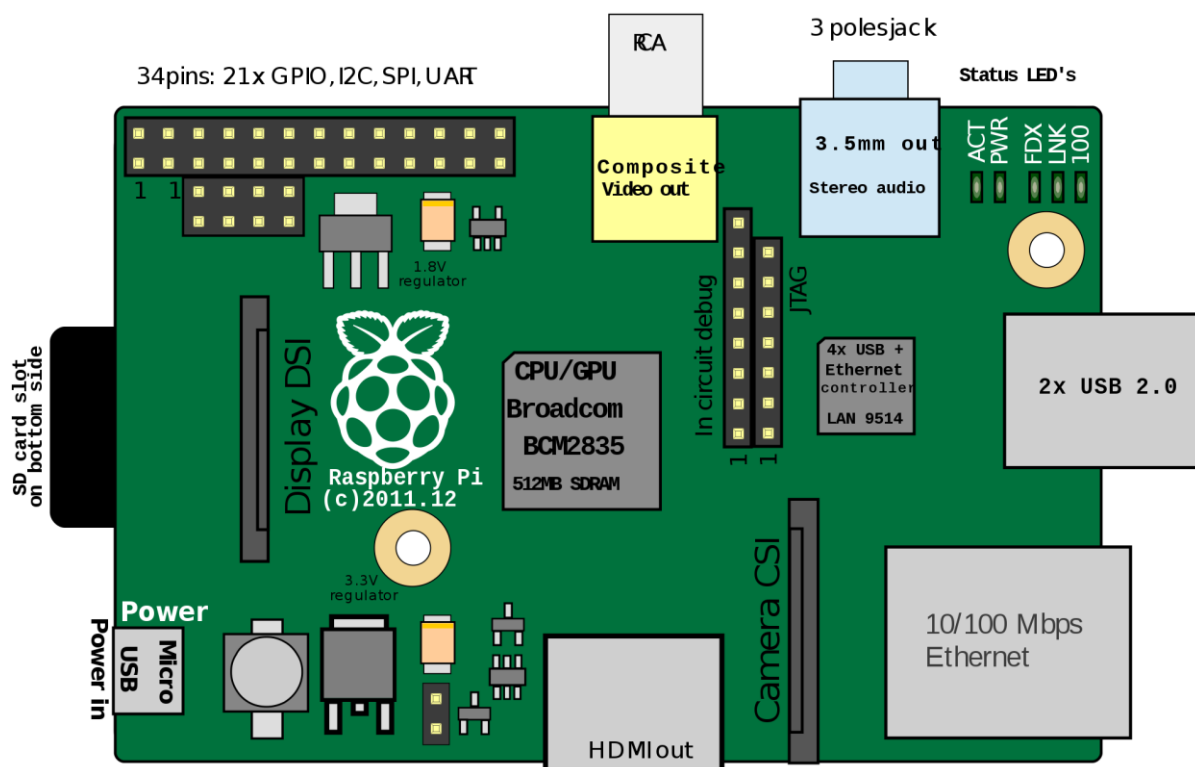


Fig. 5.18. RPI-3 schematic diagram.

Inertial Measurement Unit (IMU)

To measure the flight status, IMU is used to collect angular velocity and linear acceleration data which is sent to the main processor in RPi. The IMU contains two separate sensors. The first sensor is the accelerometer triad. It generates three analog signals describing the accelerations along each of its axes produced by, and acting on the airplane. Due to thruster system and physical limitations, the most significant of these sensed accelerations is caused by gravity. The second sensor is the angular rate sensor triad. It also outputs three analog signals. These signals describe the vehicle angular rate about each of the sensor axes.

The data from these sensors is collected by the MPU 6050 microprocessor through a 12bit ADC board. The sensor information is then returned to the main processor via a SPI interface at a rate of about 50 Hz.

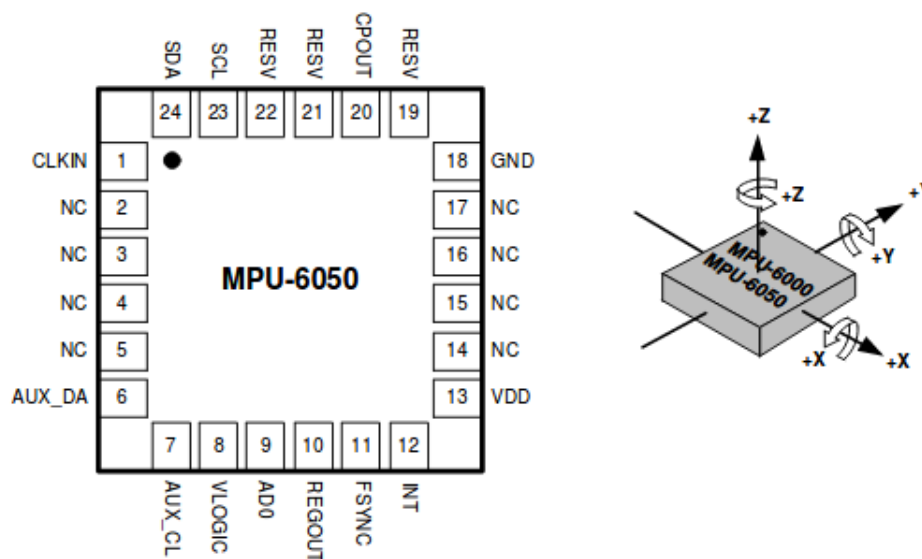


Fig. 5.19. MPU6050 schematic diagram.

PWM driver (PCA-9685)

To drive the control mechanism in aircraft, an adafruit 16-Channel 12-bit PWM/Servo Driver - I2C interface - PCA9685 is selected as servo driver board. The PCA-9685 is use to drive 4 flaps, 4 motors, 2 wing tilting servo and 1 rudder servo. As shown in Figure 5.16.

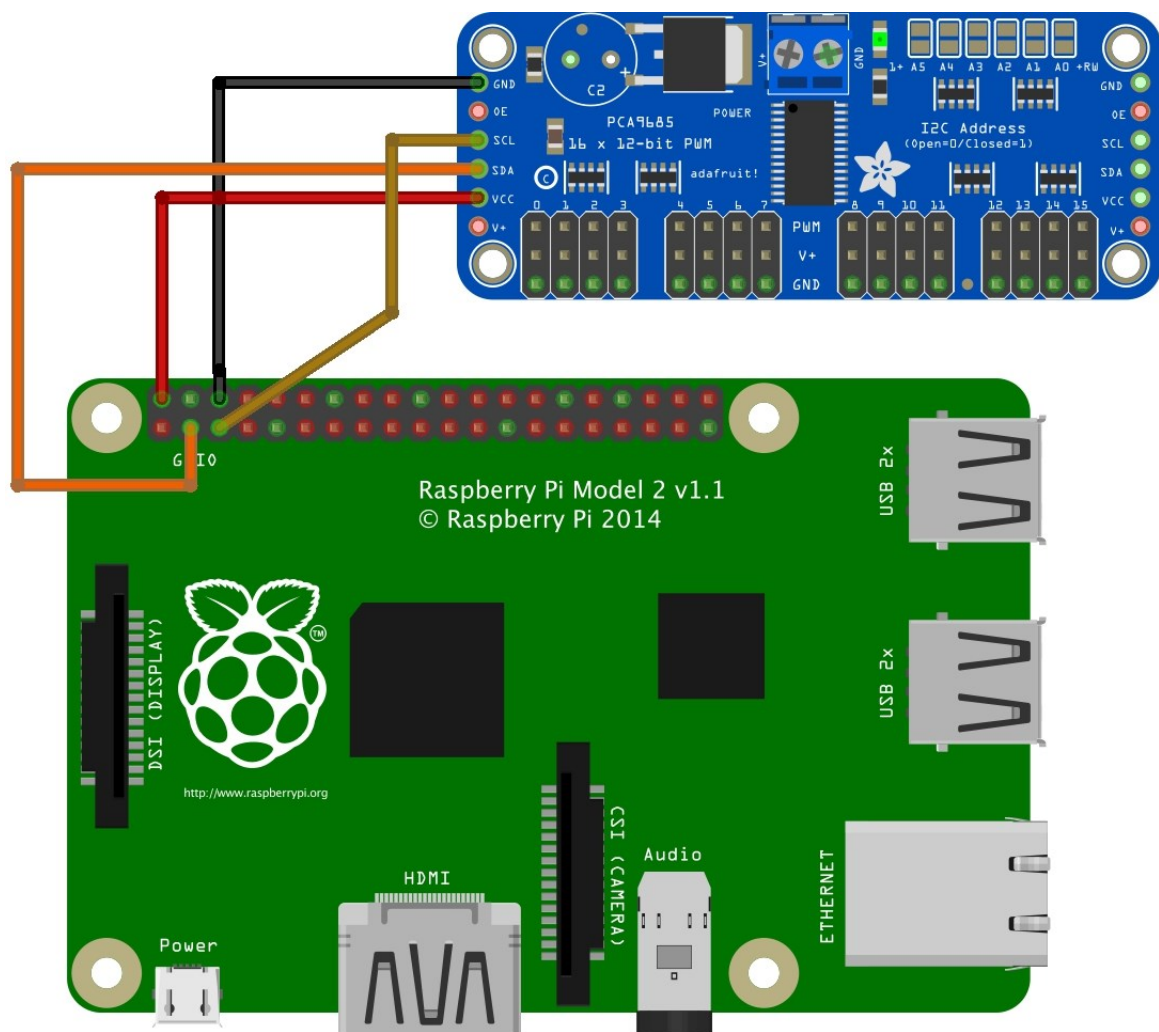


Fig. 5.20. RPI-3 and PCA 9685 schematic diagram.

Chapter 6

Conclusion

This dissertation has presented the study of Quad Tilt Wing Unmanned Aerial Vehicle (QTW-UAV) flight controller improvements and aircraft implementation. Problem motivation and objective of this research have been presented in Chapter 1. Chapter 2 has summarized the necessary background theories regarding to fixed-structured CAS controller within an H_∞ framework as well as PSO optimization.

To address the drawbacks in existing design methods for Quad Tilt Wing Unmanned Aerial Vehicle (QTW- UAV), i.e., oscillatory motions and a large numerical complexity in controller gain design, this chapter proposes a method for Control Augmentation System (CAS) design with the application of Particle Swarm Optimization (PSO). In contrast to the previously used method, the design requirements are given in frequency domain, to be more specific, weighted sensitivity function from attitude command to attitude error is required to satisfy an H_∞ norm constraint. We first verify the applicability of our method by CAS design for McART3 in which the target sensitivity function is given by using the gains in an existing paper.

For improvement of the designed CAS gains, to enhance the robust control performance of the designed gains multiple model approach is similarly applied to realize controller gains robustness against the plants modeling errors. We first investigate the applicability of our CAS design method for McART3 in which the target sensitivity function is set as the one whose holds the maximum peak gain, among the nominal and perturbed models

using the gains in an existing paper. As a result, it is confirmed that our obtained gains are robustly optimized as well as guarantee the worst case performances in all tilt angles. Then, as an extension, we address oscillatory suppressing CAS design in lateral-directional motion. In exchange for slightly slow responses, oscillatory suppressing CAS gains are confirmed. Next, the improvement of the performance of nominal model is further investigated when the probability functions are given. To confirm the applicability of our oscillatory suppressing CAS gains which successfully designed in linear time invariant domain, Nonlinear flight simulations are conducted under both normal and wind gust conditions. The designed gains worked well in both environments. In particular, roll angle faithfully follows their commands in all tilt angles which represent good tracking performances are achieved.

Finally, the aircraft hardware implementation is conducted starting from basic design requirements, design process, aircraft elements manufacturing, assembling process, on-flight control unit and ground station platform design.

List of Publications

Conference articles

1. SCI 16 symposium: (Domestic conference)

H_∞ Structured Controller Synthesis Applied to Flight Controller of QTW-UAV using Meta-Heuristic Particle Swarm Optimization, [longitudinal -nominal model]
2016.5.25-27 , Kyoto Teresa, JAPAN

2. SICE 2016 annual conference: (International conference)

H_∞ Structured Controller Synthesis Applied to Flight Controller of QTW-UAV using Meta-Heuristic Particle Swarm Optimization, 2016.9.20-23 , [longitudinal and lateral-directional nominal model]. Tsukuba international conference center, JAPAN

3. IFAC ACA 2016 conference: (International conference)

H_∞ Structured Controller Synthesis Applied to Flight Controller of QTW-UAV using Meta-Heuristic Particle Swarm Optimization, [longitudinal -nominal model] 20-25 August, 2016, Sherbrook, Quebec, CANADA

4. APISAT 2016: (International conference)

H_∞ Structured Controller Synthesis Applied to Flight Controller of QTW-UAV using Meta-Heuristic Particle Swarm Optimization, [longitudinal and lateral-directional nominal model] Toyama International Conference Center, Toyama, JAPAN, October 25-27, 2016

5. APISAT 2017: (International conference)

Oscillatory Reduction Design for Structured H_∞ Controller Applied to Flight Controller of QTW-UAV using Particle Swarm Optimization., Seoul, Korea

Journal Articles

1. H_∞ Control Based CAS Design of QTW-UAV Using Particle Swarm Optimization
Submitted to “The Transactions of the Japanese Society Japan Society for Aeronautical and Space Sciences (TJSASS)” - Under revision with reviewers
2. H_∞ Control Based CAS Design for QTW-UAV via Multiple Model Approach with Particle Swarm Optimization in submission process to International Journal of Aerospace Engineering, Hindawi – in submission process.

APPENDIX A

In this appendix A, we provide the supplementary results in which the target sensitivity function is set as the one with CAS gains in 3.6). To ensure the applicability of our proposed method. The optimized gains in Table 3.1 (a),(b) and $1/|W(s)|$ for nominal model in both longitudinal and lateral-directional motions are used to produce similar responses to the JAXA nominal model design.

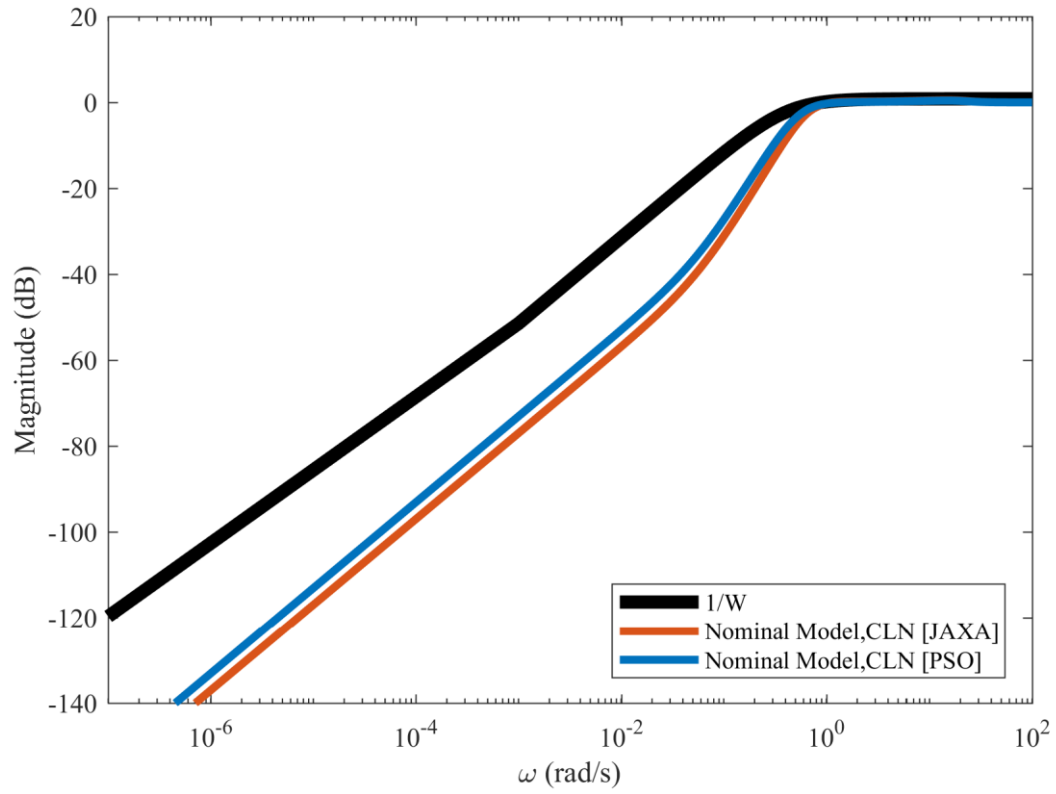


Fig. 7.1. Gain plots of sensitivity functions with CAS gains in 3.6), optimized gains in Table 3.1 (a) and $1/|W(s)|$ at $\tau_\omega = \text{cln}$ [lon. motion].

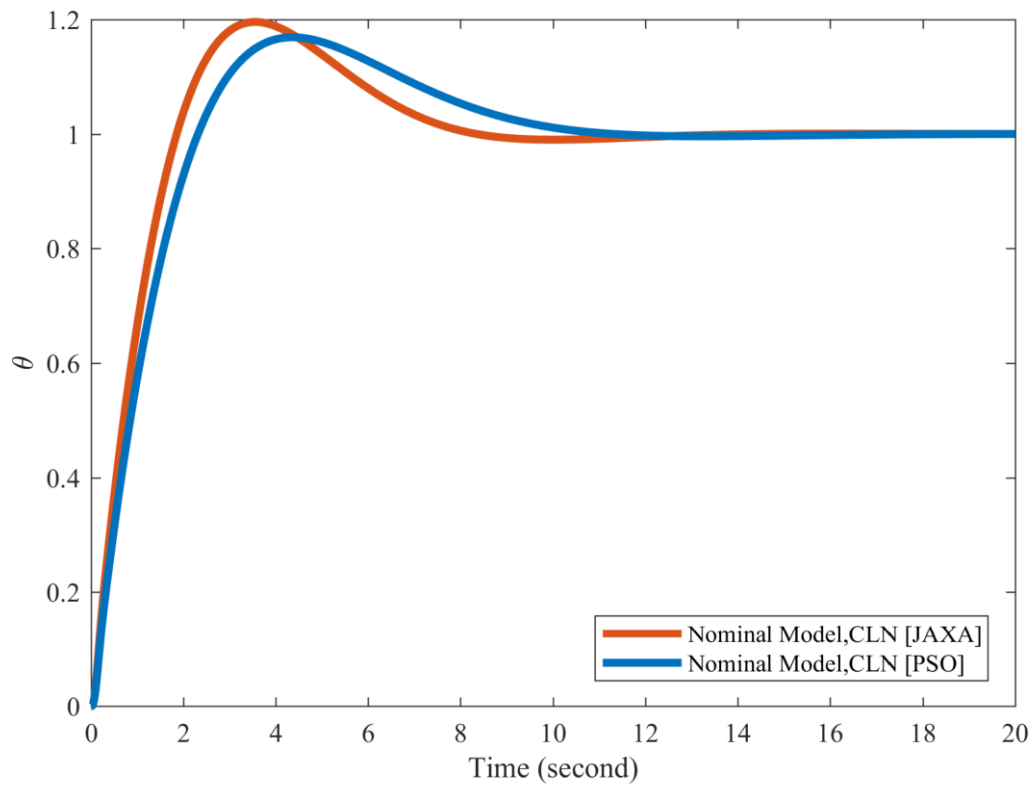


Fig. 7.2. Step responses of θ with CAS gains in 3.6), optimized gains in Table 3.1(a) at $\tau_\omega = \text{cln}$ [lon. motion].

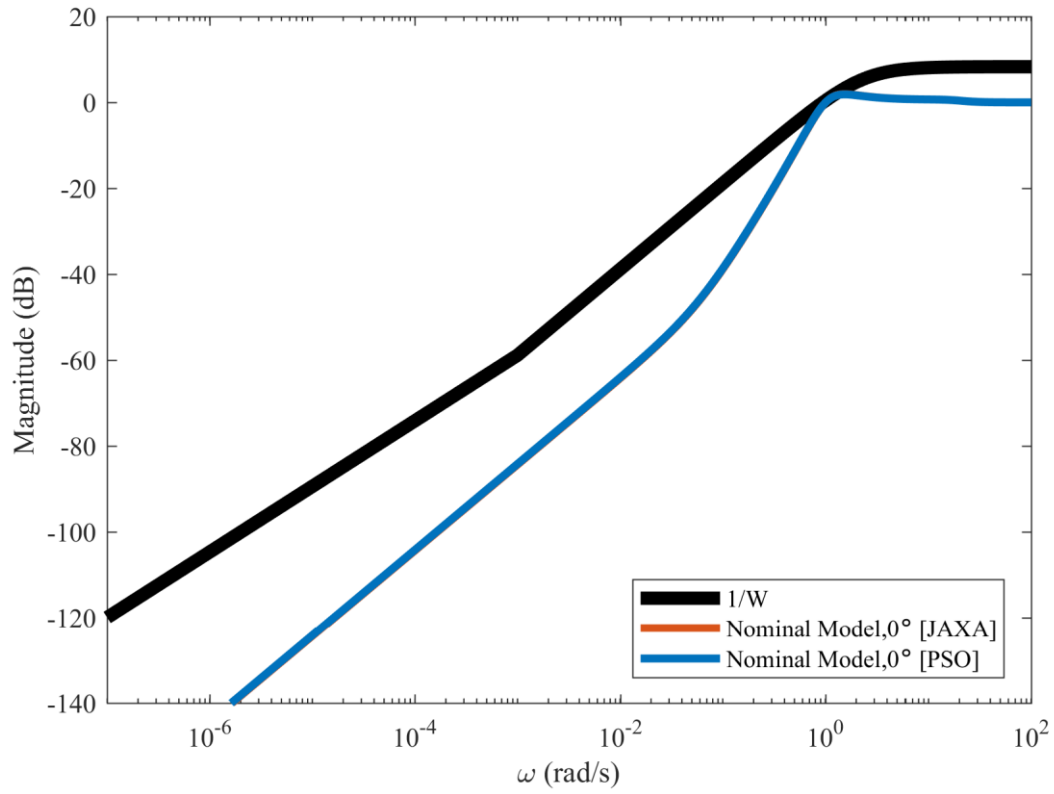


Fig. 7.3. Gain plots of sensitivity functions with CAS gains in 3.6), optimized gains in Table 3.1 (a) and $1/|W(s)|$ at $\tau_\omega = 0^\circ$ [lon. motion].

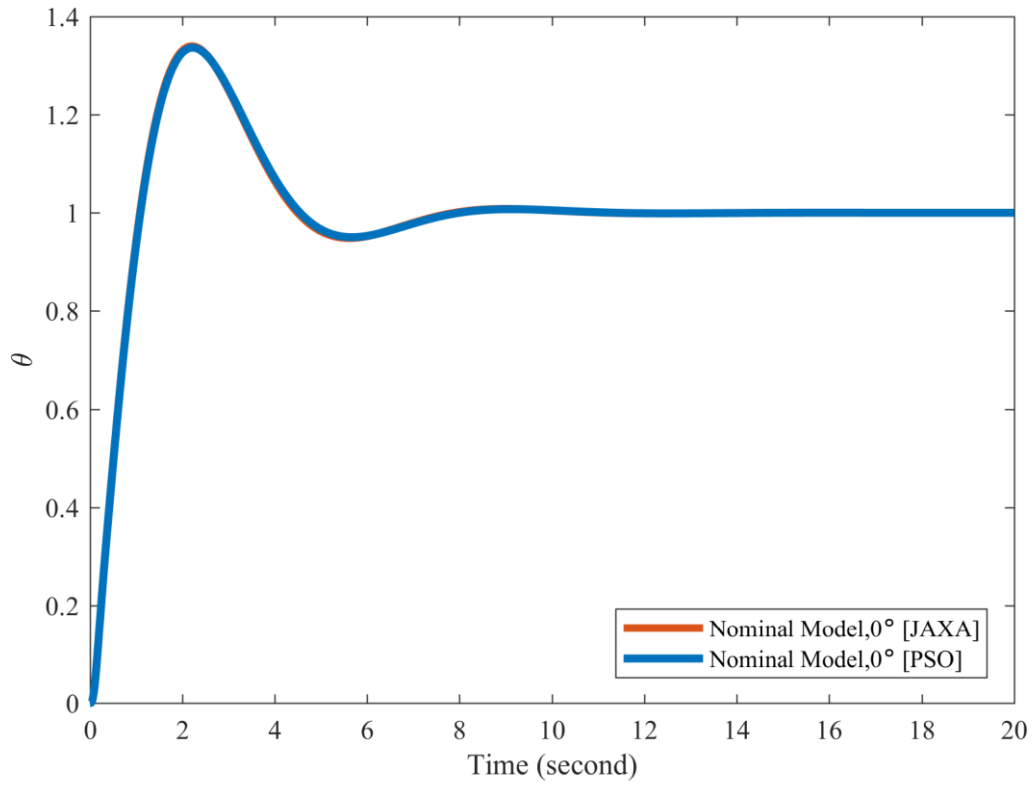


Fig.7.1. Step responses of θ with CAS gains in 3.6), optimized gains in Table 3.1(a) at $\tau_\omega = 0^\circ$ [lon. motion].

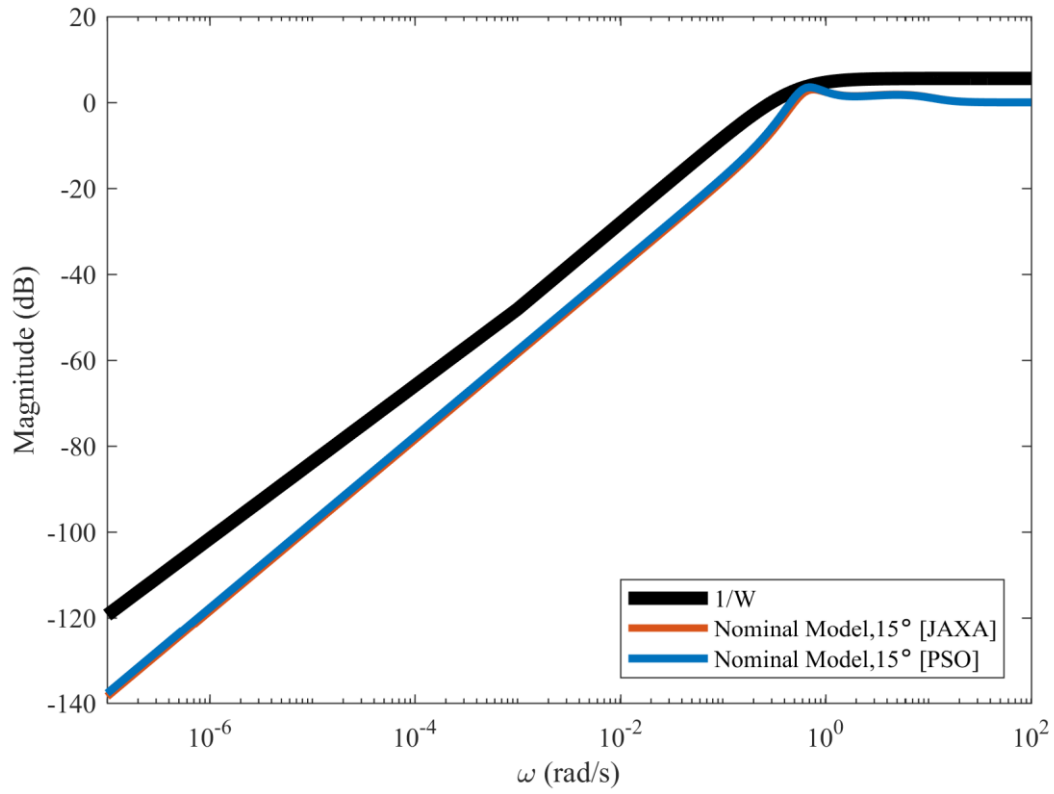


Fig. 7.5. Gain plots of sensitivity functions with CAS gains in 3.6), optimized gains in Table 3.1 (a) and $1/|W(s)|$ at $\tau_\omega = 15^\circ$ [lon. motion].

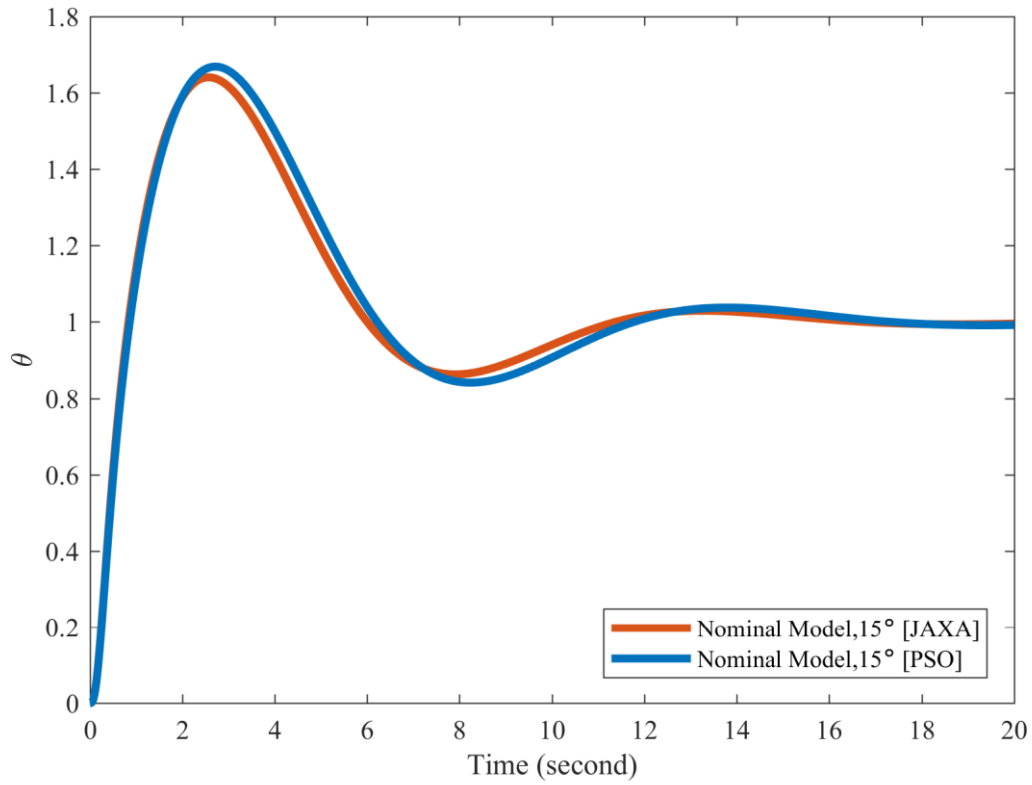


Fig. 7.6. Step responses of θ with CAS gains in 3.6), optimized gains in Table 3.1 (a) at $\tau_\omega = 15^\circ$ [lon. motion].

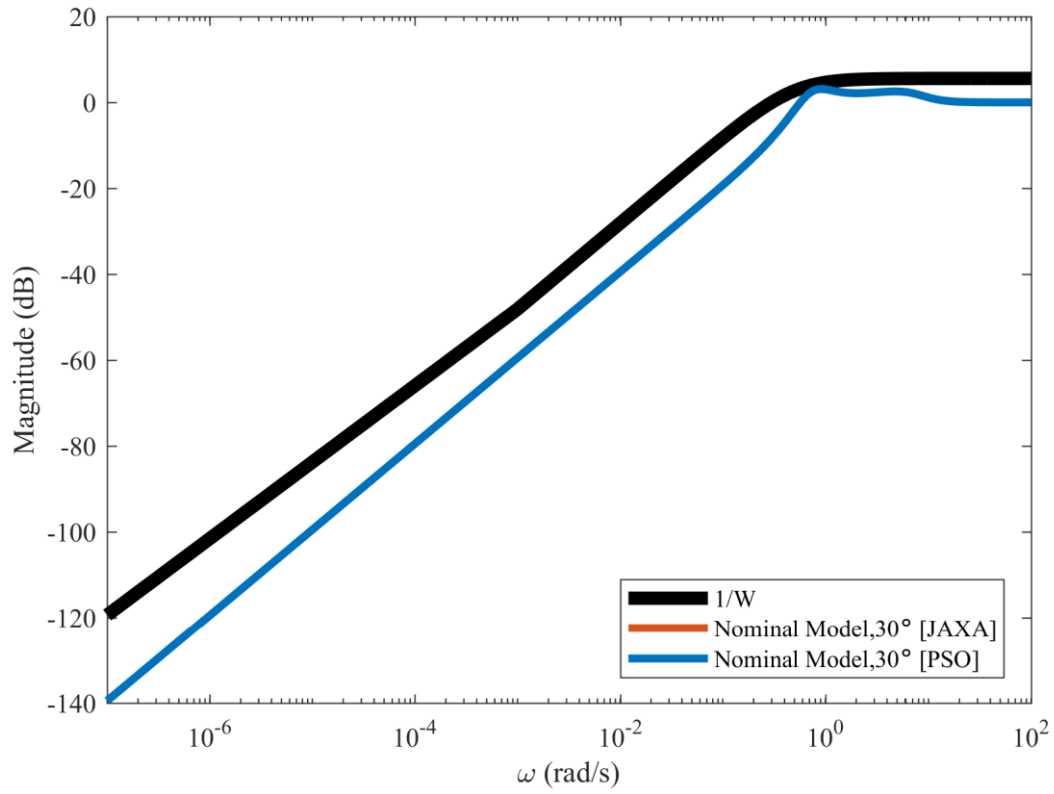


Fig. 7.7. Gain plots of sensitivity functions with CAS gains in 3.6), optimized gains in Table 3.1 (a) and $1/|W(s)|$ at $\tau_\omega = 30^\circ$ [lon. motion].

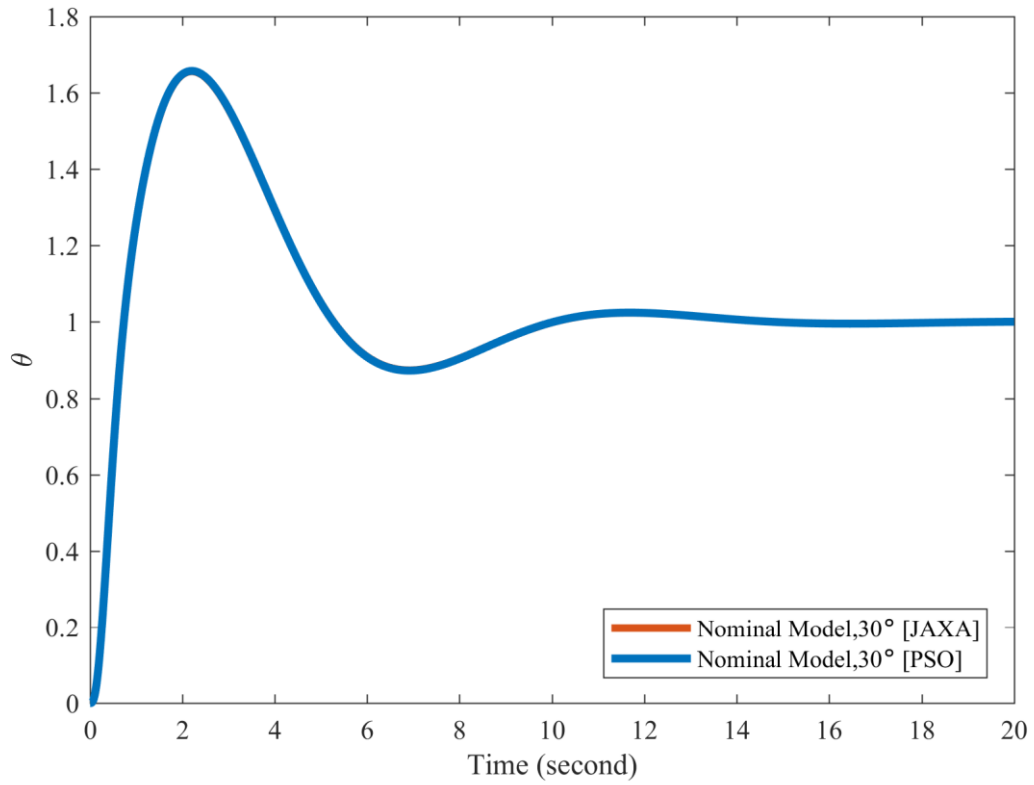


Fig. 7.8. Step responses of θ with CAS gains in 3.6), optimized gains in Table 3.1 (a) at $\tau_\omega = 30^\circ$ [lon. motion].

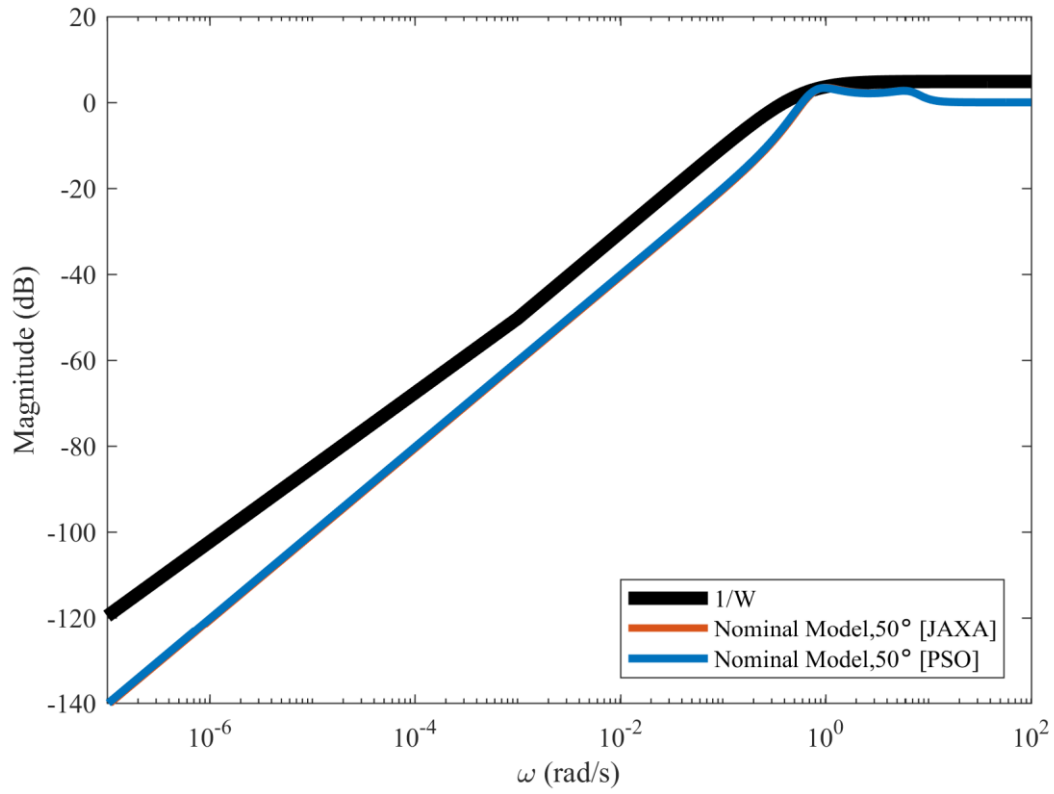


Fig. 7.9. Gain plots of sensitivity functions with CAS gains in 3.6), optimized gains in Table 3.1 (a) and $1/|W(s)|$ at $\tau_\omega = 50^\circ$ [lon. motion].

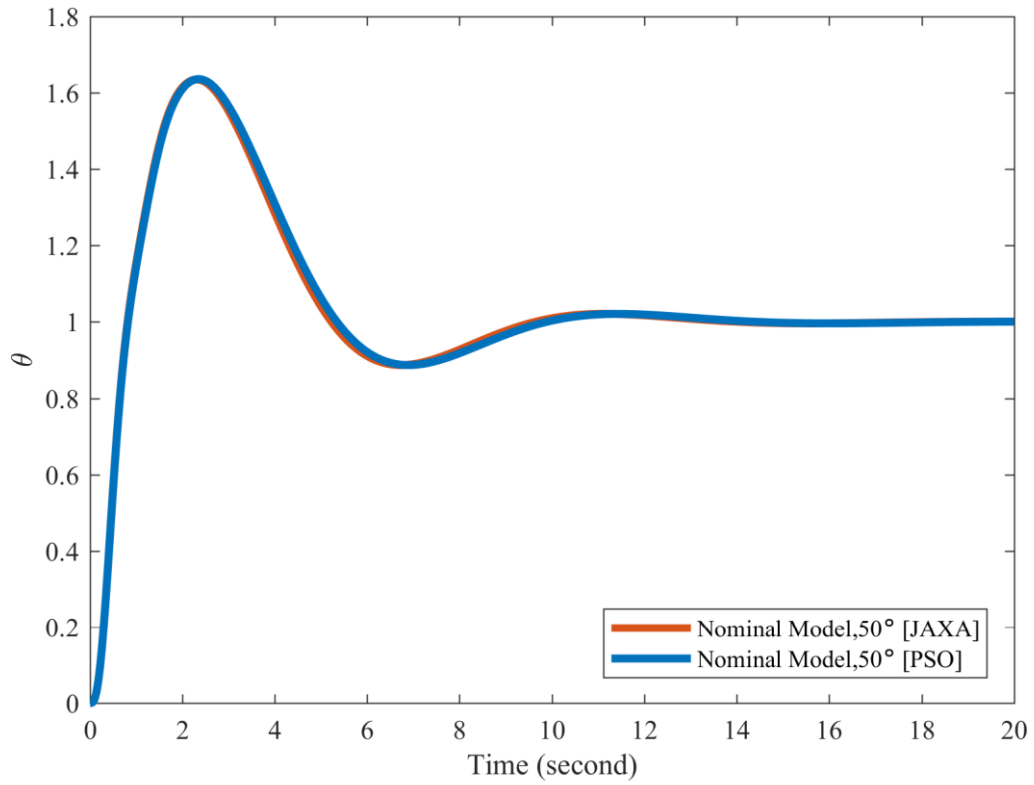


Fig. 7.10. Step responses of θ with CAS gains in 3.6), optimized gains in Table 3.1 (a) at $\tau_\omega = 50^\circ$ [lon. motion].

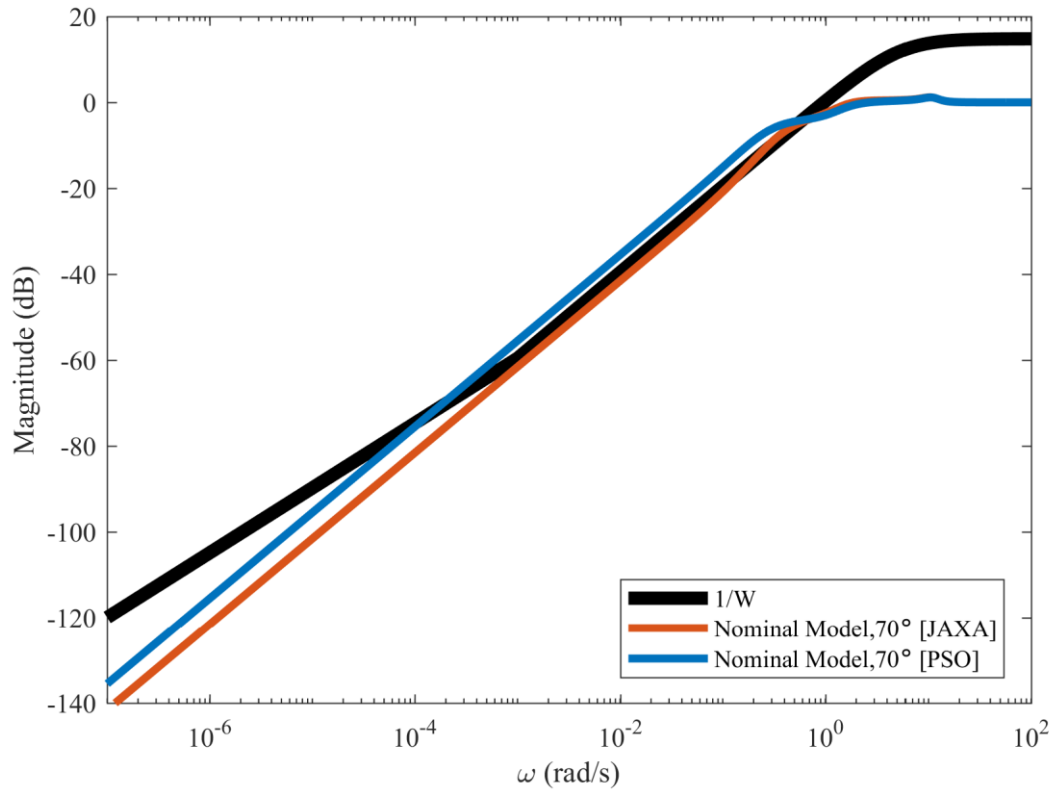


Fig. 7.11. Gain plots of sensitivity functions with CAS gains in 3.6), optimized gains in Table 3.1 (a) and $1/|W(s)|$ at $\tau_\omega = 70^\circ$ [lon. motion].

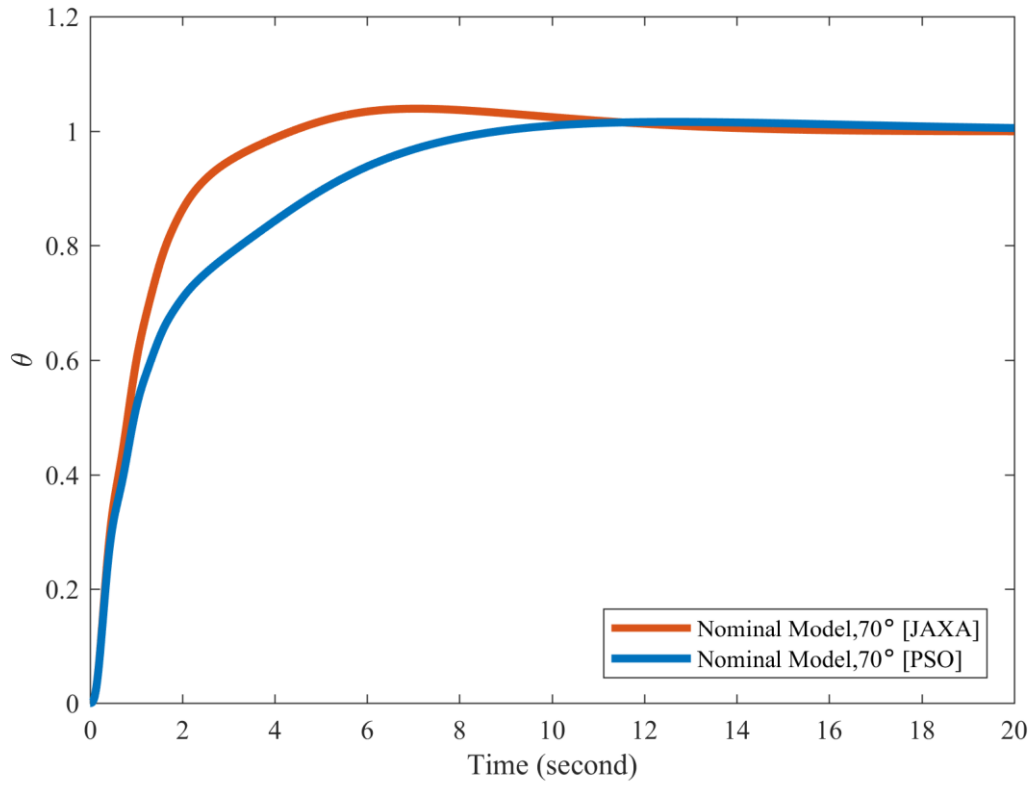


Fig. 7.12. Step responses of θ with CAS gains in 3.6), optimized gains in Table 3.1 (a) at $\tau_\omega = 70^\circ$ [lon. motion].

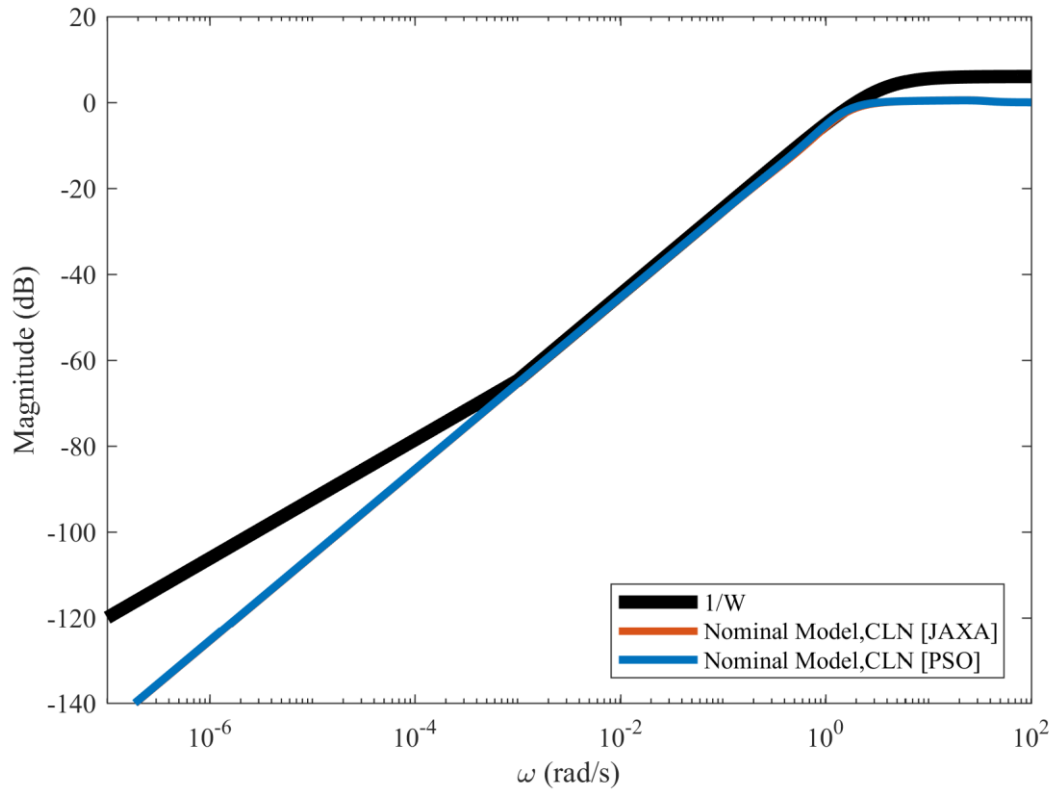


Fig. 7.13. Gain plots of sensitivity functions with CAS gains in 3.6), optimized gains in Table 3.1 (b) and $1/|W(s)|$ at $\tau_\omega = \text{cln}$ [lat. motion].

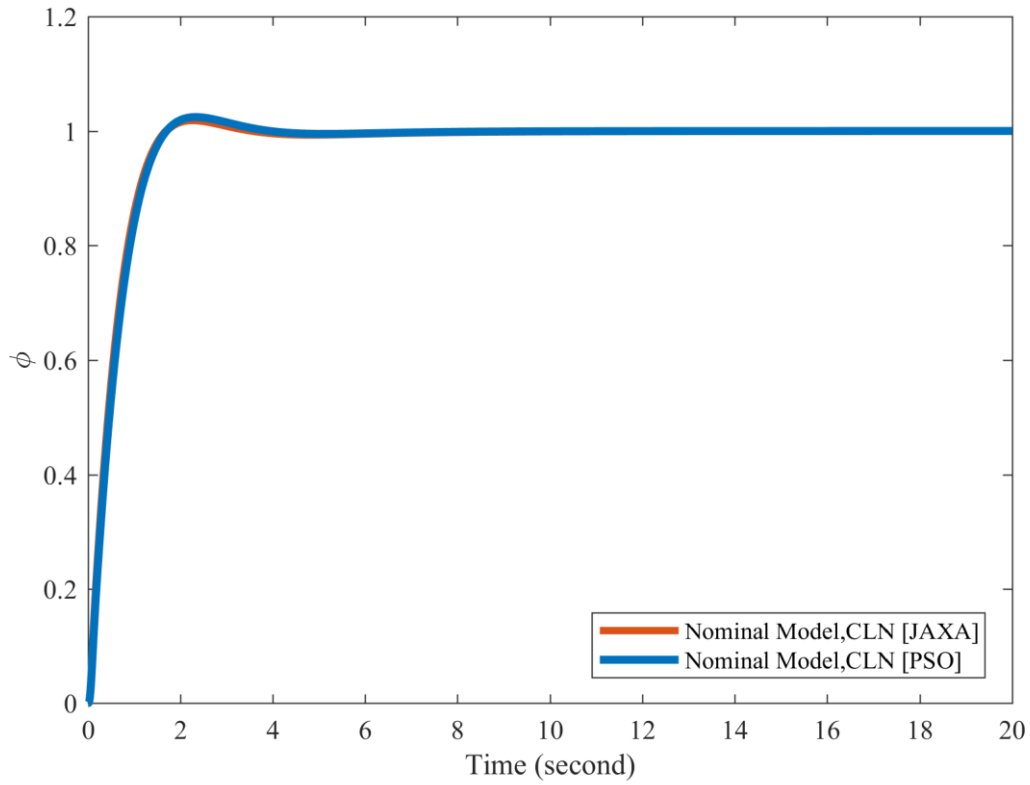


Fig. 7.12. Step responses of ϕ with CAS gains in 3.6), optimized gains in Table 3.1 (b) at $\tau_\omega = \text{cln}$ [lat. motion].

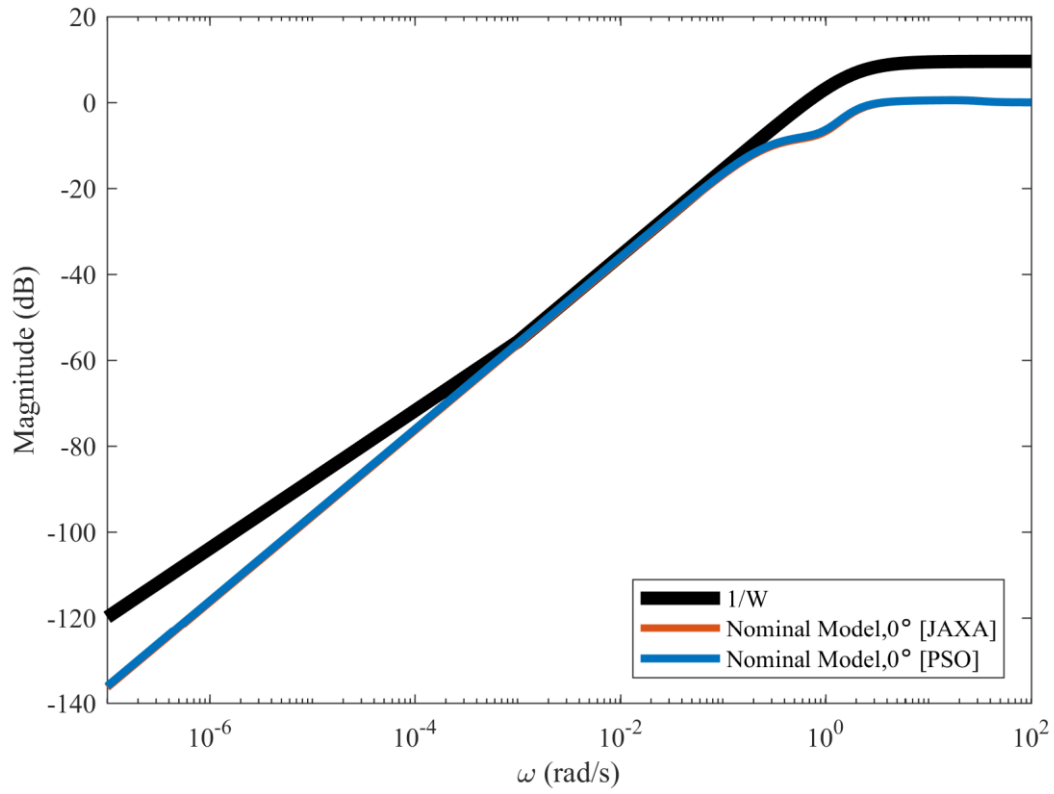


Fig. 7.15. Gain plots of sensitivity functions with CAS gains in 3.6), optimized gains in Table 3.1 (b) and $1/|W(s)|$ at $\tau_\omega = 0^\circ$ [lat. motion].

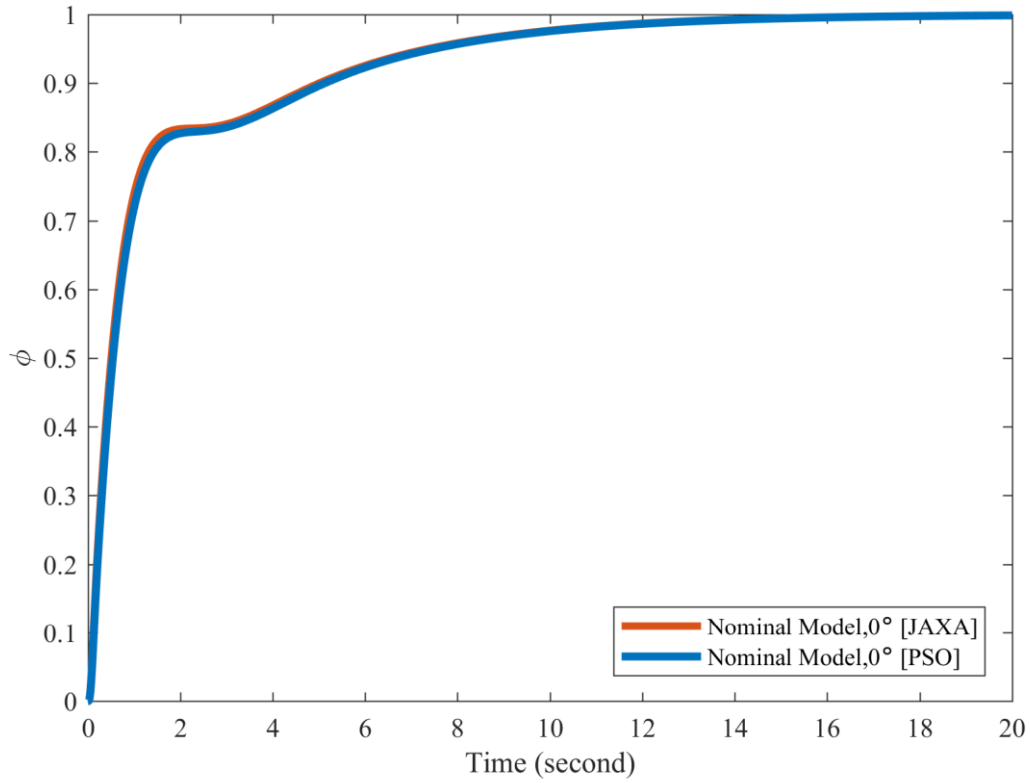


Fig. 7.16. Step responses of ϕ with CAS gains in 3.6), optimized gains in Table 3.1 (b) at $\tau_\omega = 0^\circ$ [lat. motion].

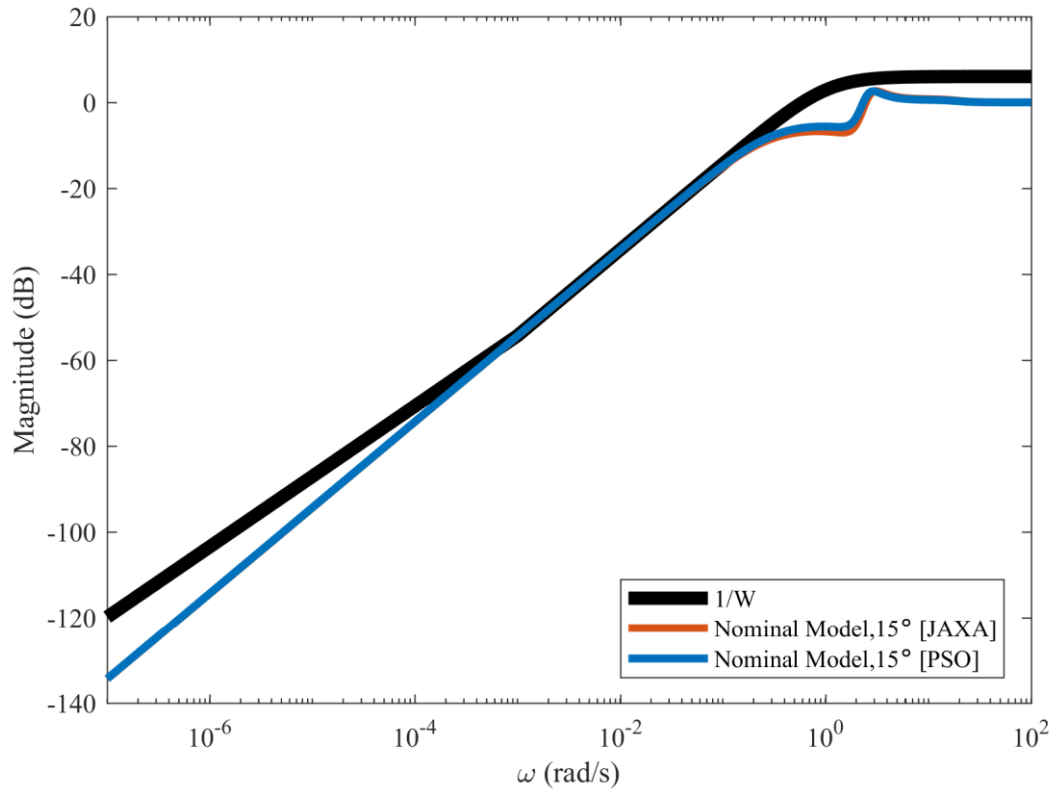


Fig. 7.17. Gain plots of sensitivity functions with CAS gains in 3.6), optimized gains in Table 3.1 (b) and $1/|W(s)|$ at $\tau_\omega = 15^\circ$ [lat. motion].

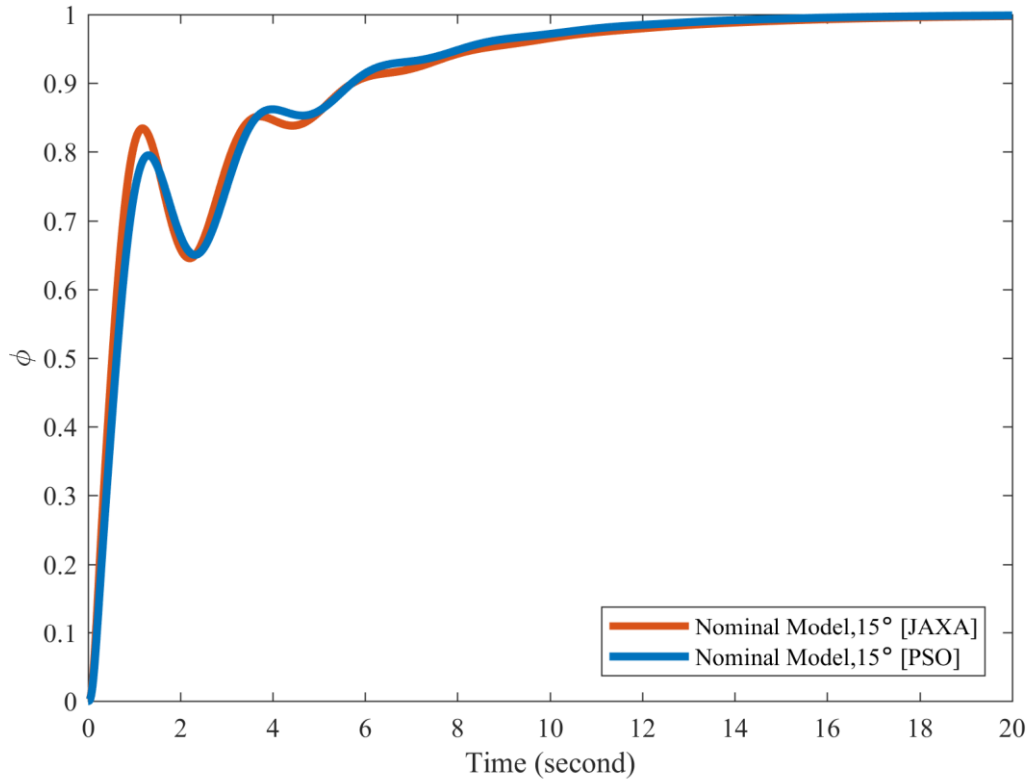


Fig. 7.18. Step responses of ϕ with CAS gains in 3.6), optimized gains in Table 3.1 (b) at $\tau_\omega = 15^\circ$ [lat. motion].

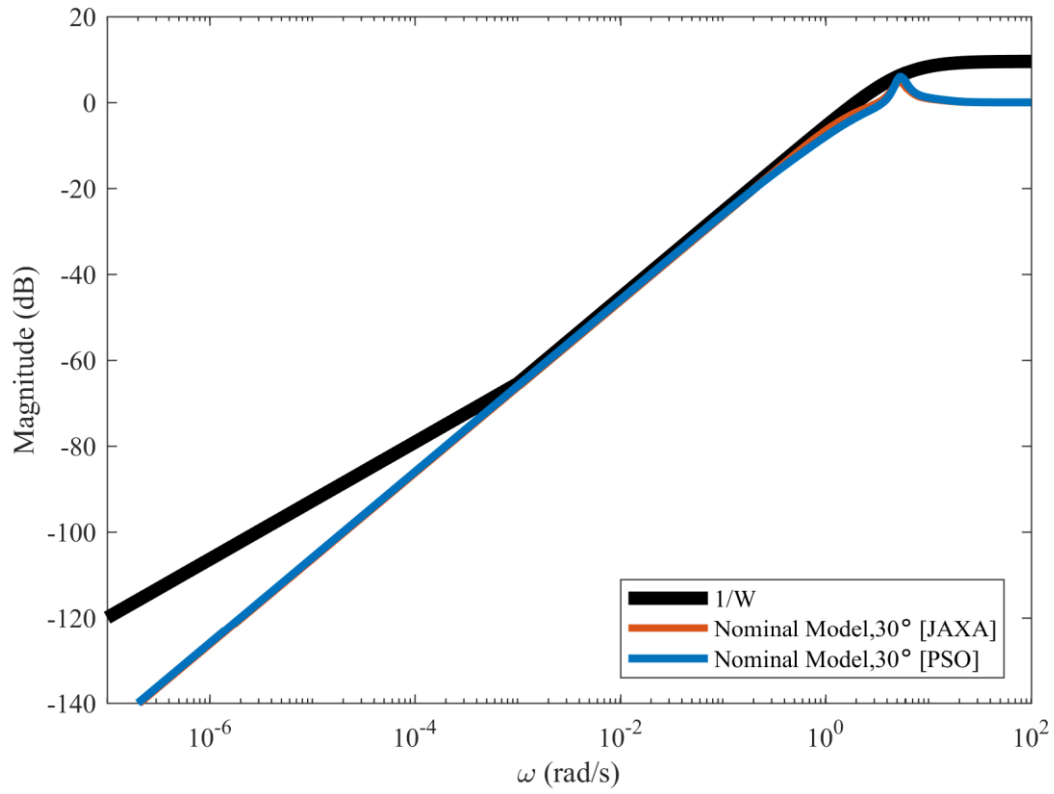


Fig. 7.19. Gain plots of sensitivity functions with CAS gains in 3.6), optimized gains in Table 3.1 (b) and $1/|W(s)|$ at $\tau_\omega = 30^\circ$ [lat. motion].

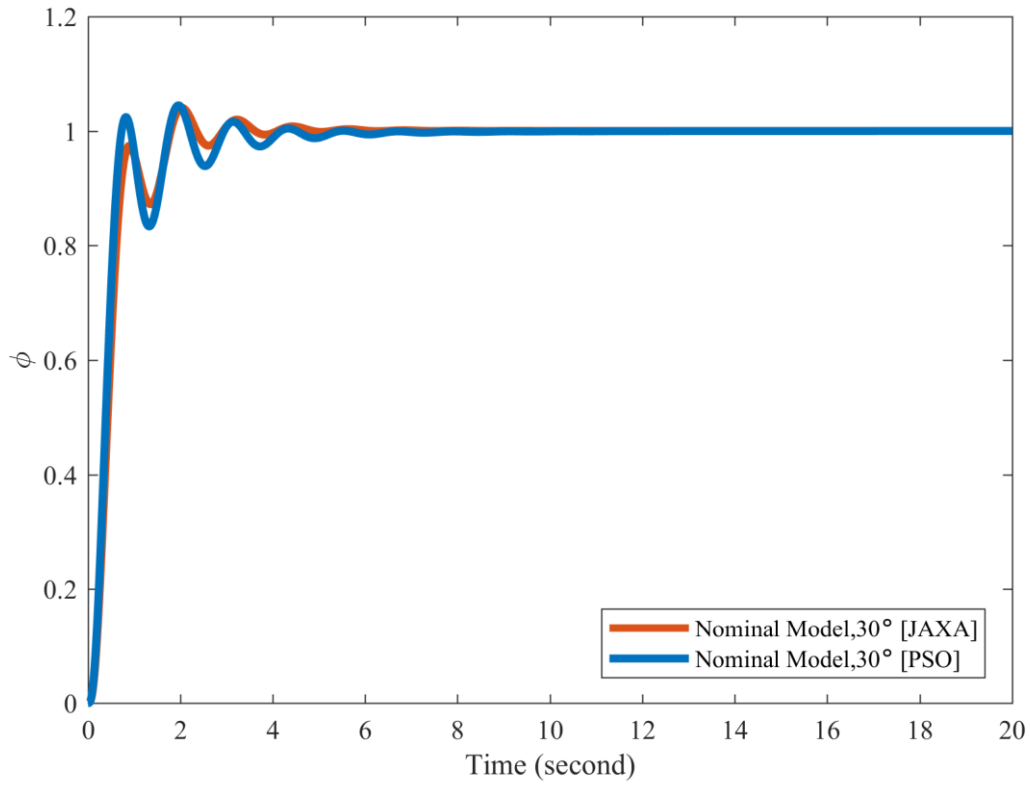


Fig. 7.20. Step responses of ϕ with CAS gains in 3.6), optimized gains in Table 3.1 (b) at $\tau_\omega = 30^\circ$ [lat. motion].

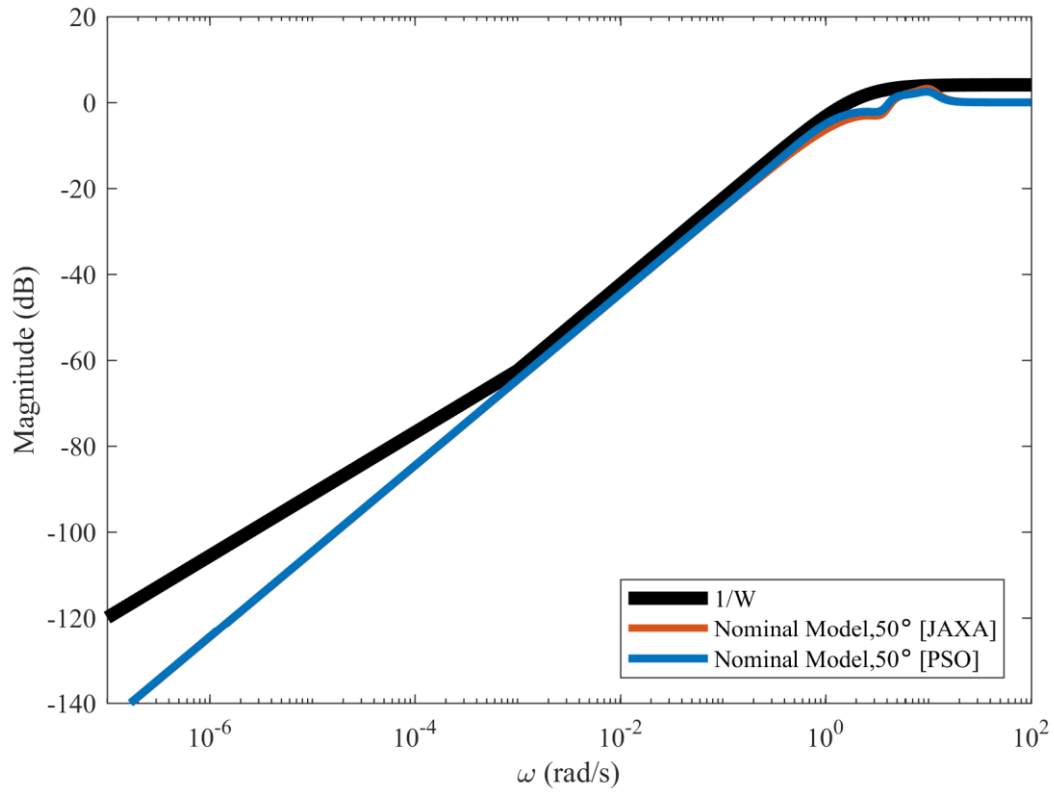


Fig. 7.31. Gain plots of sensitivity functions with CAS gains in 3.6), optimized gains in Table 3.1 (b) and $1/|W(s)|$ at $\tau_\omega = 50^\circ$ [lat. motion].

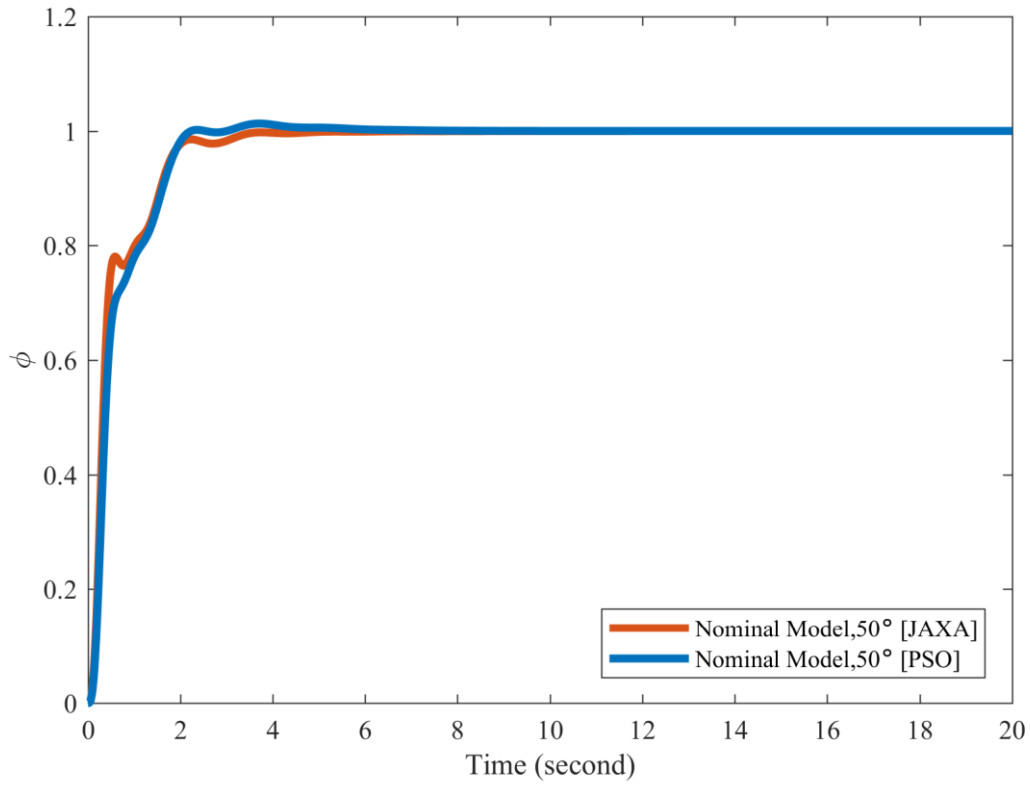


Fig. 7.22. Step responses of ϕ with CAS gains in 3.6), optimized gains in Table 3.1 (b) at $\tau_\omega = 50^\circ$ [lat. motion].

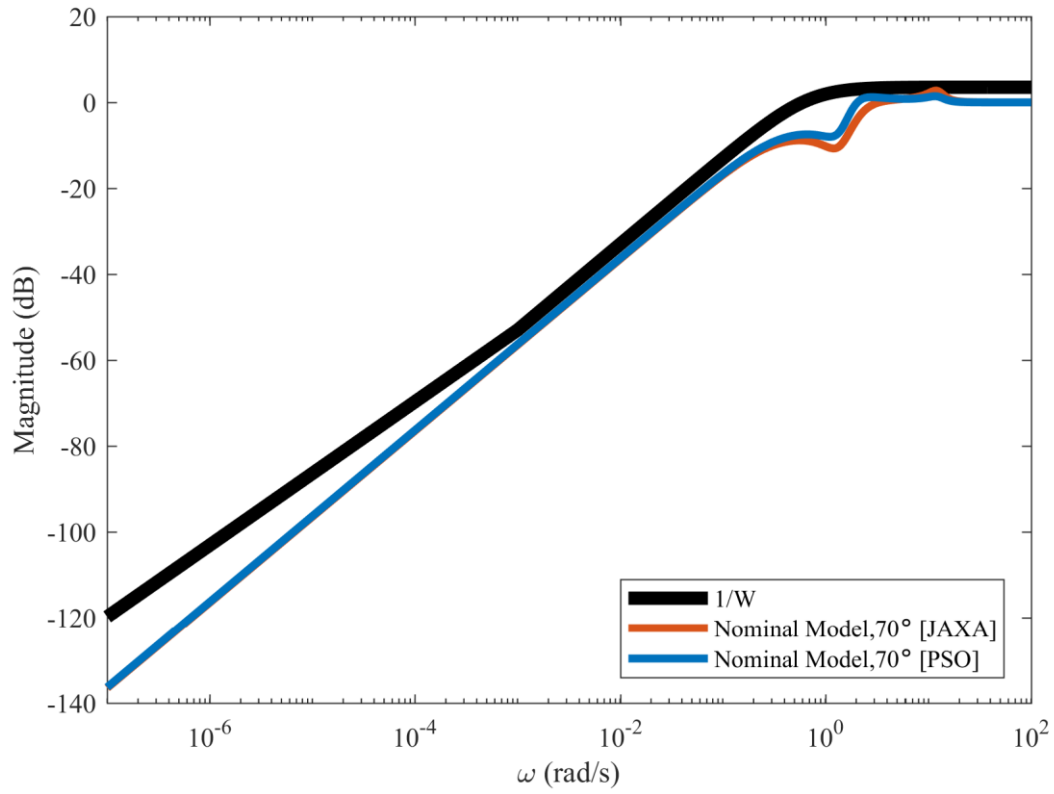


Fig. 7.43. Gain plots of sensitivity functions with CAS gains in 3.6), optimized gains in Table 3.1 (b) and $1/|W(s)|$ at $\tau_\omega = 70^\circ$ [lat. motion].

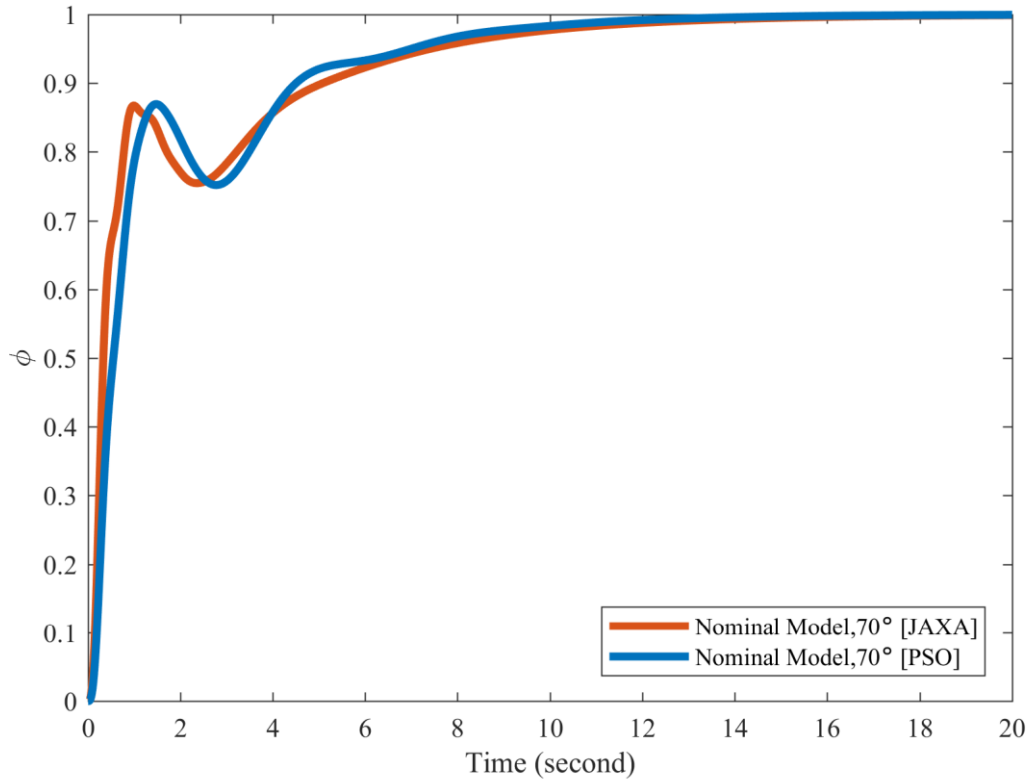


Fig. 7.25. Step responses of ϕ with CAS gains in 3.6), optimized gains in Table 3.1 (b) at $\tau_\omega = 70^\circ$ [lat. motion].

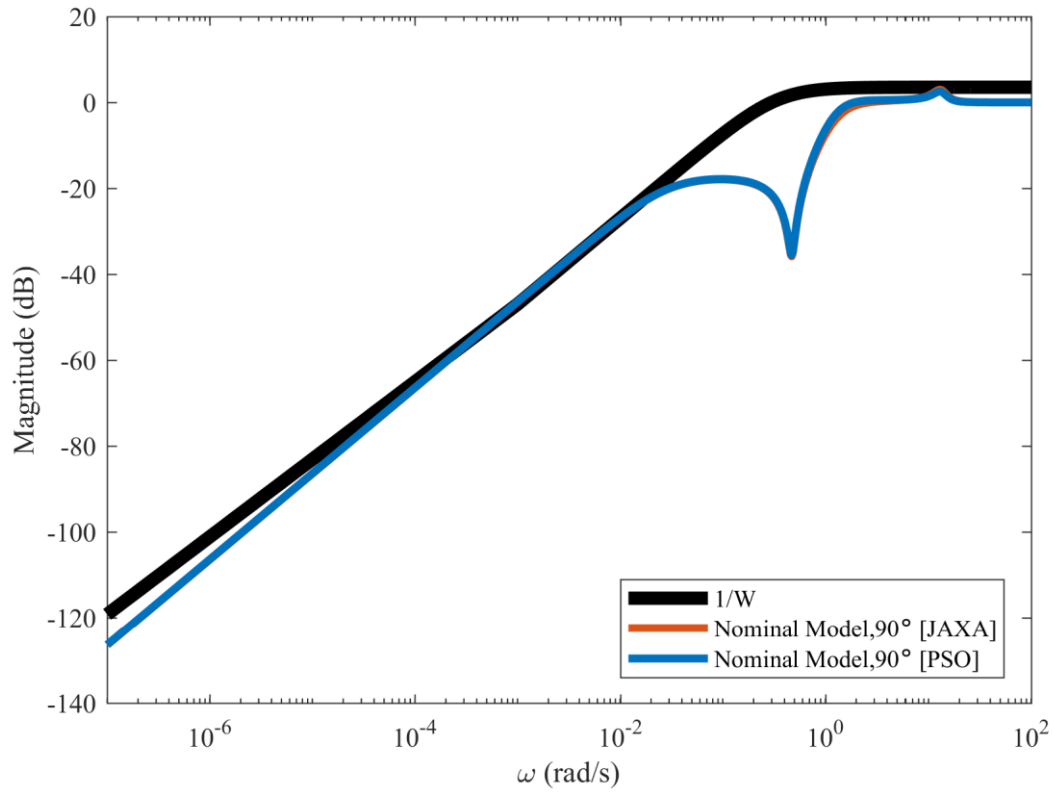


Fig. 7.65. Gain plots of sensitivity functions with CAS gains in 3.6), optimized gains in Table 3.1 (b) and $1/|W(s)|$ at $\tau_\omega = 90^\circ$ [lat. motion].

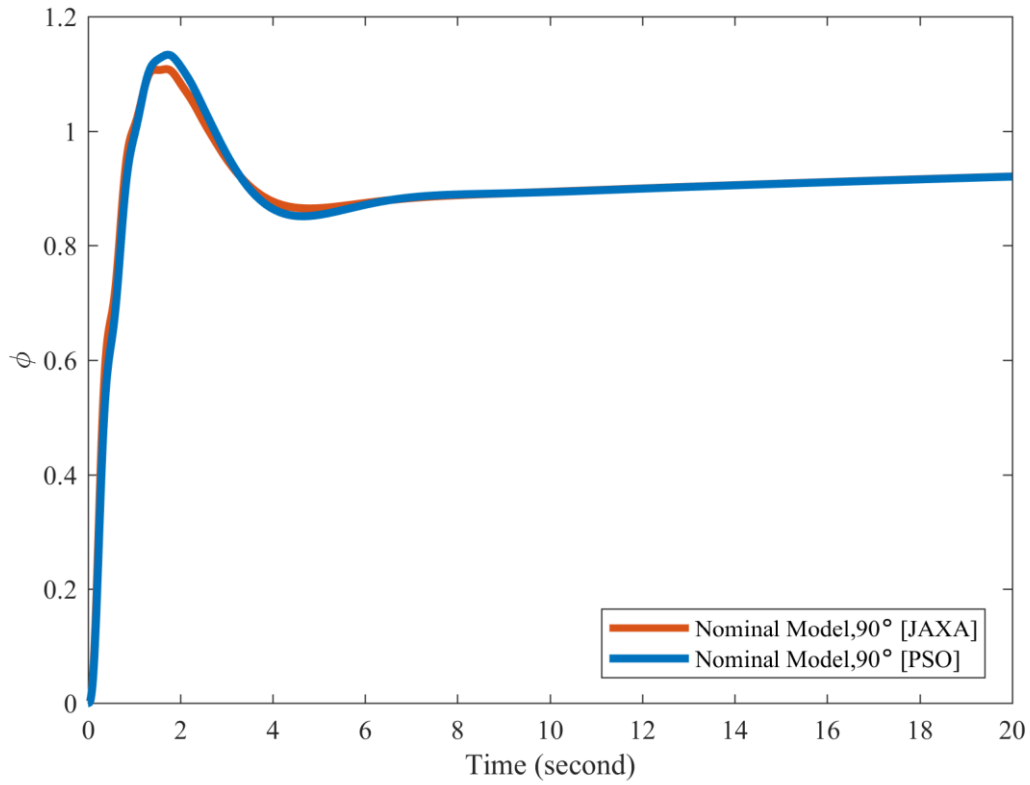


Fig. 7.26. Step responses of ϕ with CAS gains in 3.6), optimized gains in Table 3.1 (b) at $\tau_\omega = 90^\circ$ [lat. motion].

APPENDIX B

In this appendix B, we provide the supplementary results to ensure the applicability of our proposed method for designing the robust CAS gains which contain the ability to suppress the oscillatory motion in lateral-directional motion. The optimized gains in Table 4.2 (c) and $1/|W(s)|$ for multiple models are used to demonstrate the validity of our proposed method.

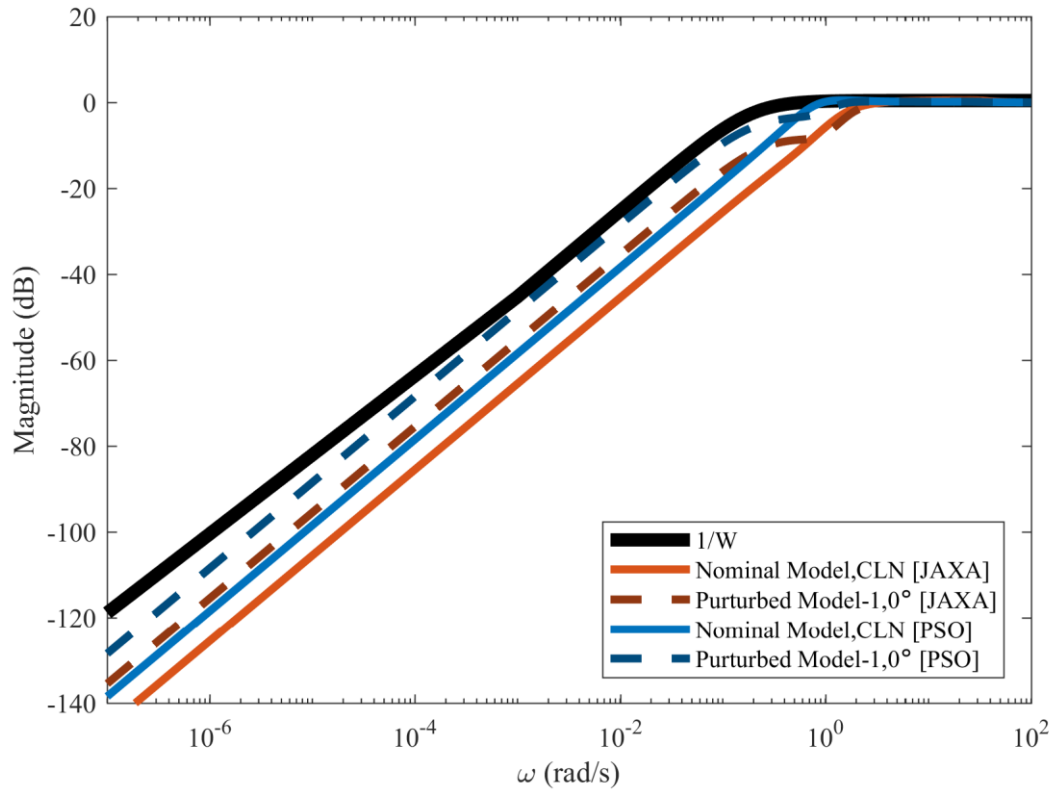


Fig. 7.77. Gain plots of sensitivity functions with CAS gains in 4.6), optimized gains in Table 4.2 (c) and $1/|W(s)|$ at $\tau_\omega = \text{cln}$ [lat. motion].

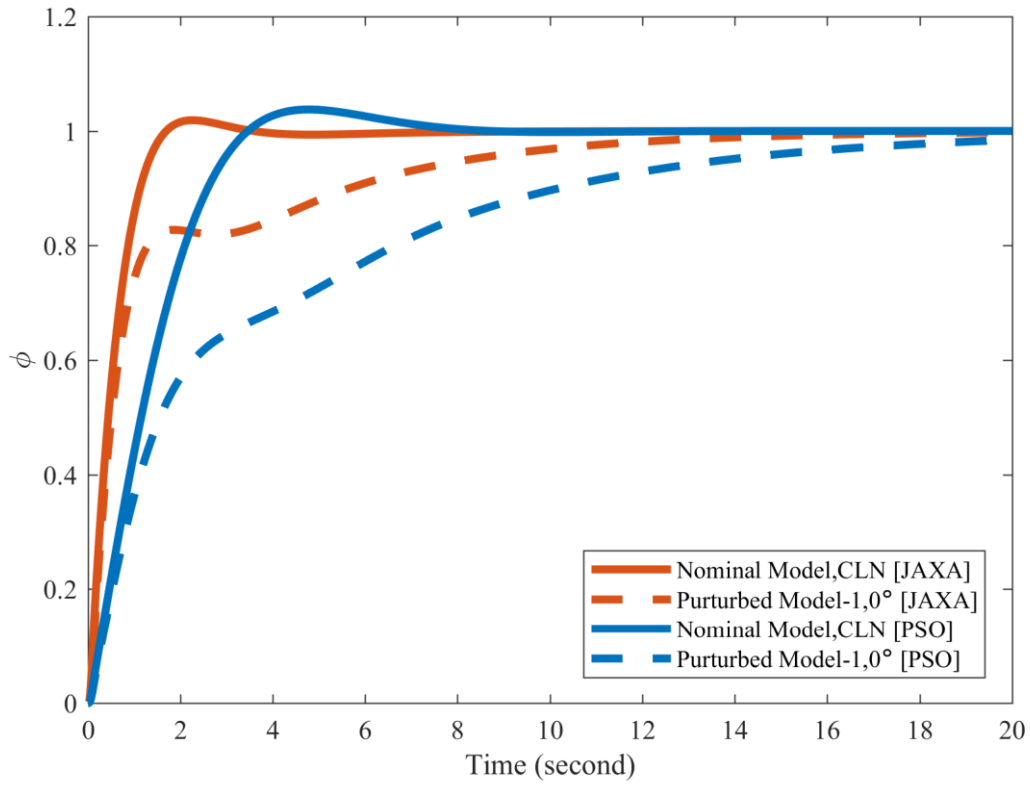


Fig. 7.28. Step responses of ϕ with CAS gains in 4.6), optimized gains in Table 4.2 (c) at $\tau_\omega = \text{cln}$ [lat. motion].

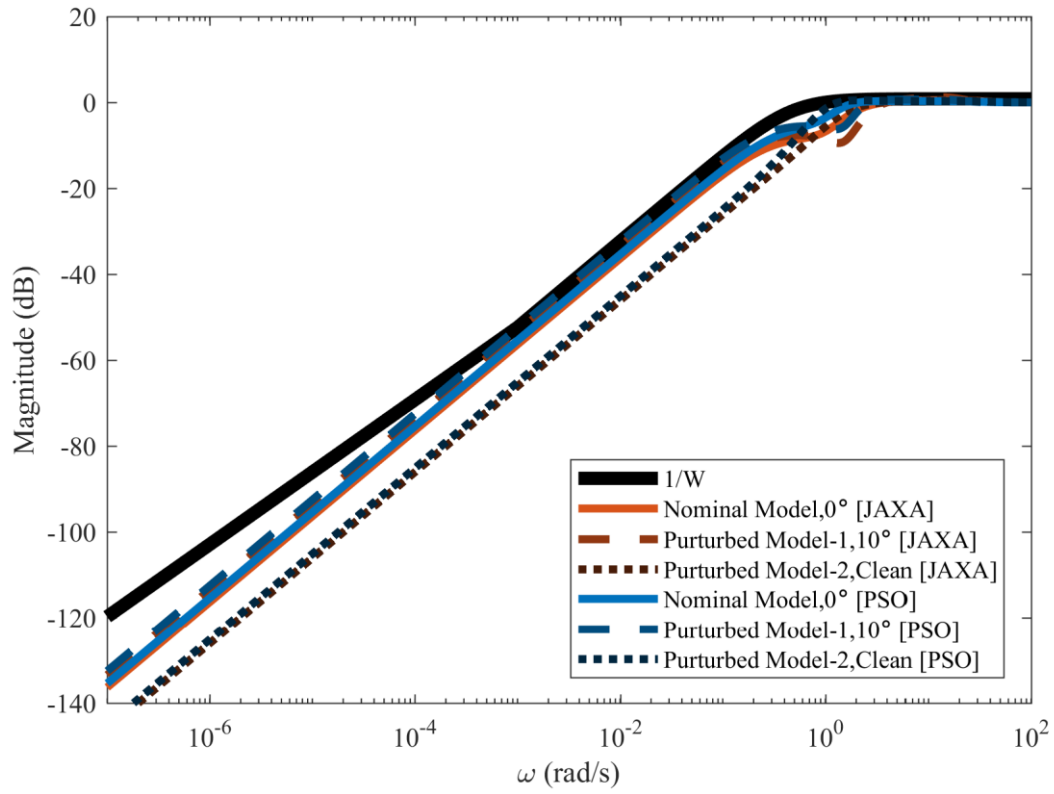


Fig. 7.89. Gain plots of sensitivity functions with CAS gains in 4.6), optimized gains in Table 4.2 (c) and $1/|W(s)|$ at $\tau_\omega = 0^\circ$ [lat. motion].

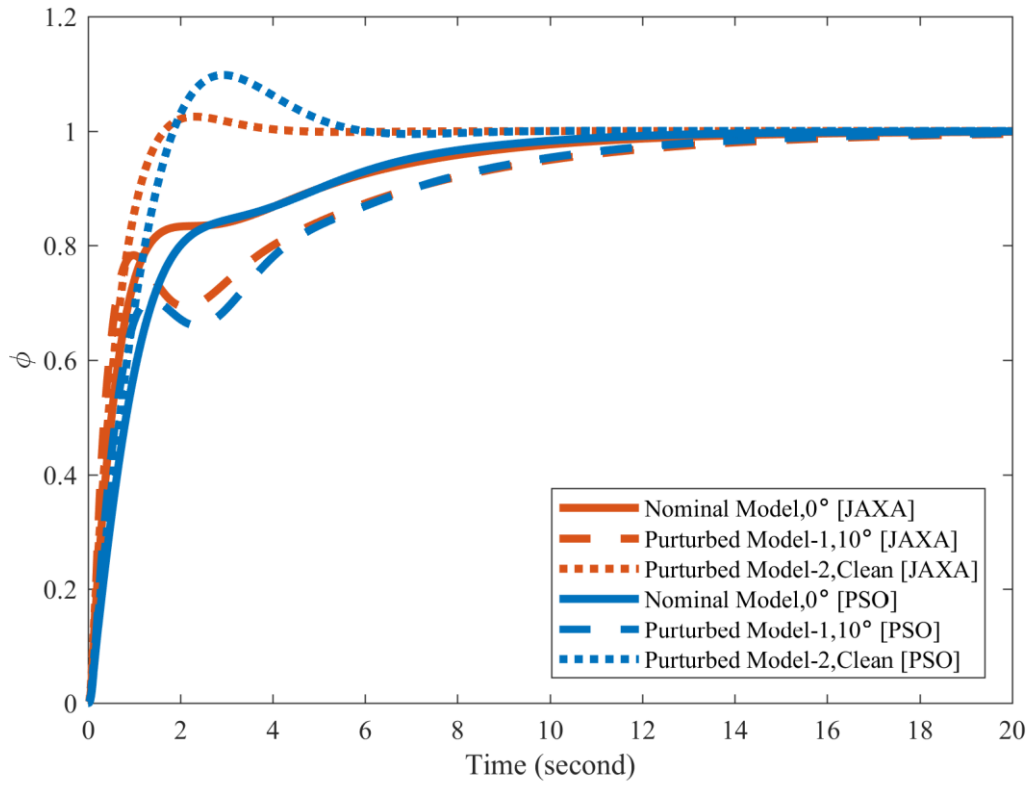


Fig. 7.30. Step responses of ϕ with CAS gains in 4.6), optimized gains in Table 4.2 (c) at $\tau_\omega = 0^\circ$ [lat. motion].

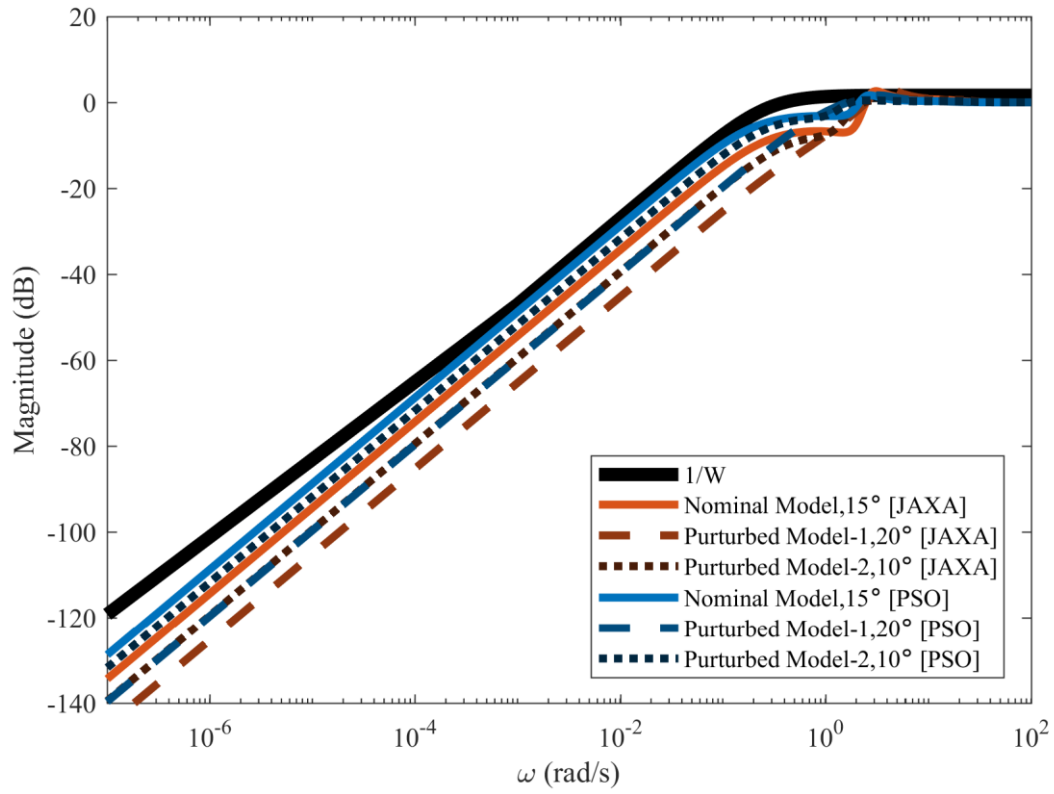


Fig. 7.31. Gain plots of sensitivity functions with CAS gains in 4.6), optimized gains in Table 4.2 (c) and $1/|W(s)|$ at $\tau_\omega = 15^\circ$ [lat. motion].

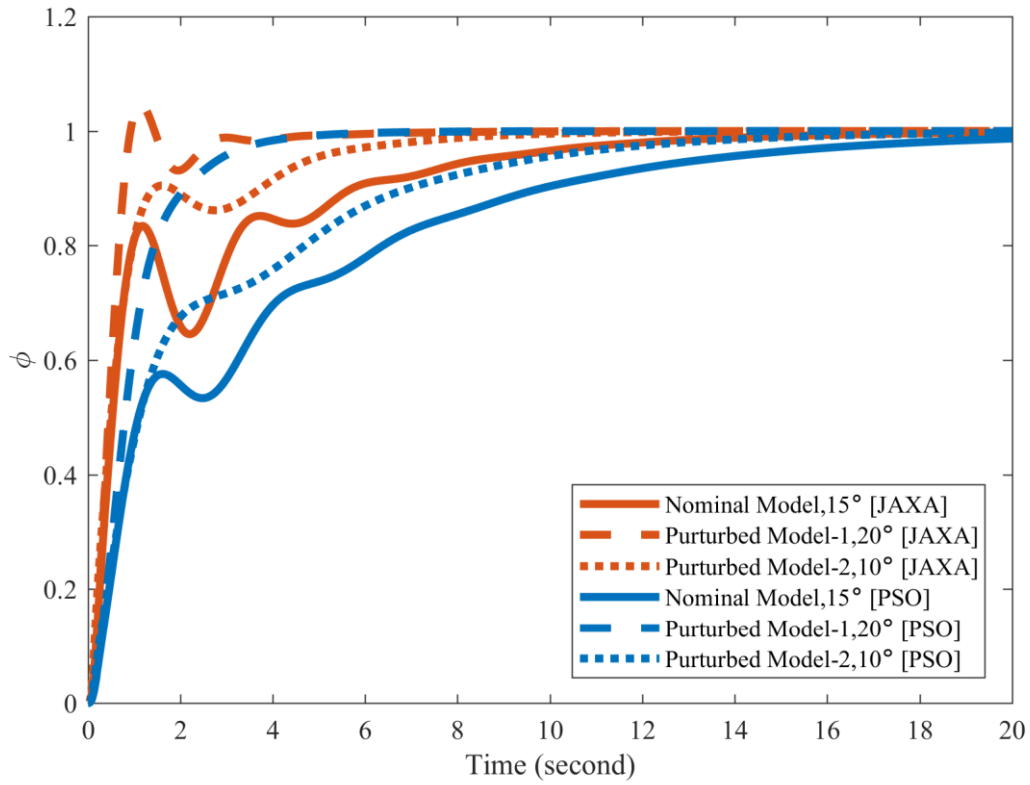


Fig. 7.32. Step responses of ϕ with CAS gains in 4.6), optimized gains in Table 4.2 (c) at $\tau_\omega = 15^\circ$ [lat. motion].

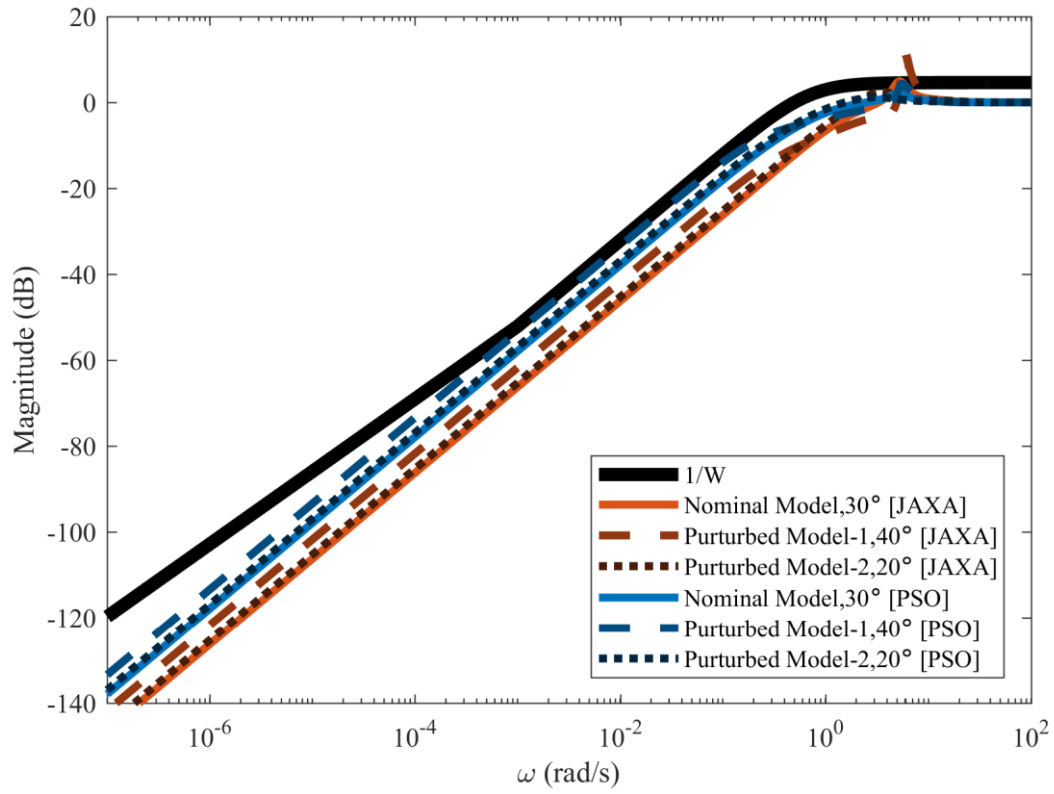


Fig. 7.33. Gain plots of sensitivity functions with CAS gains in 4.6), optimized gains in Table 4.2 (c) and $1/|W(s)|$ at $\tau_\omega = 30^\circ$ [lat. motion].

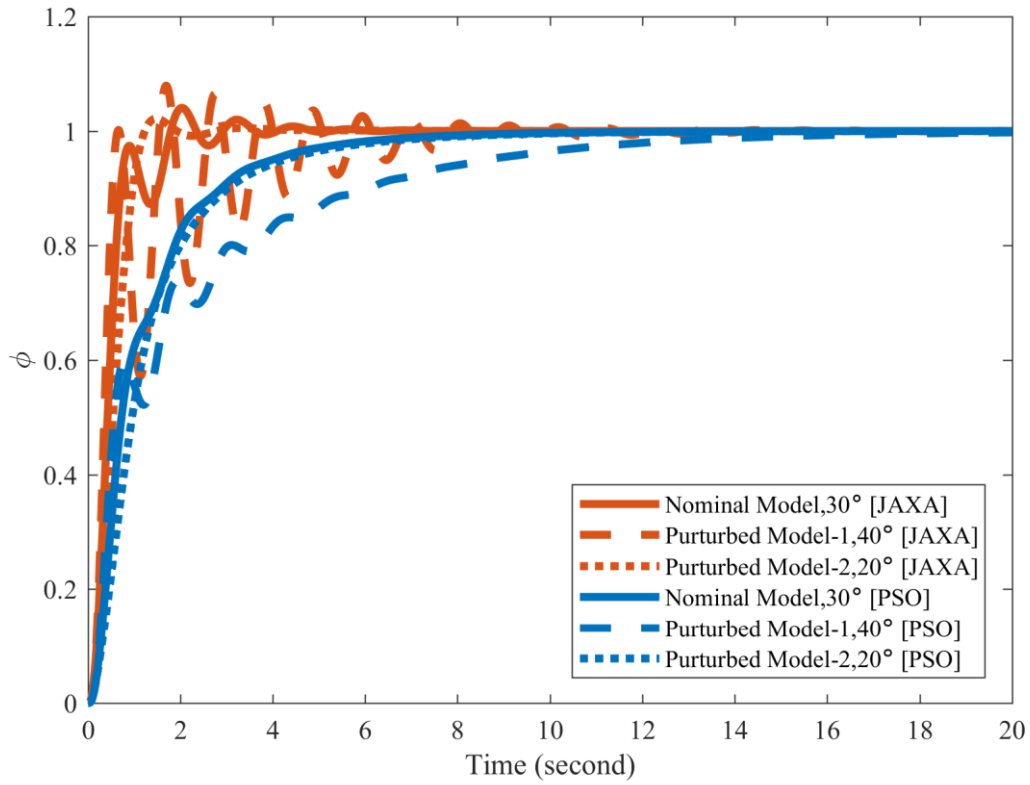


Fig. 7.34. Step responses of ϕ with CAS gains in 4.6), optimized gains in Table 4.2 (c) at $\tau_\omega = 30^\circ$ [lat. motion].

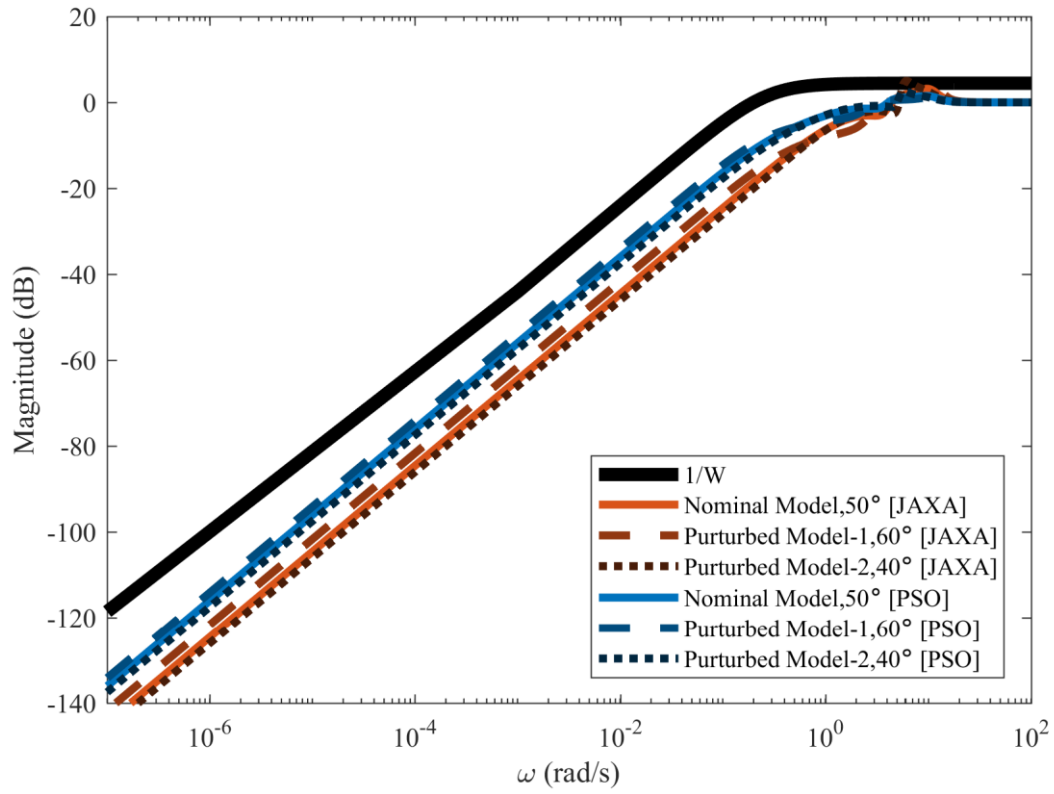


Fig. 7.35. Gain plots of sensitivity functions with CAS gains in 4.6), optimized gains in Table 4.2 (c) and $1/|W(s)|$ at $\tau_\omega = 50^\circ$ [lat. motion].

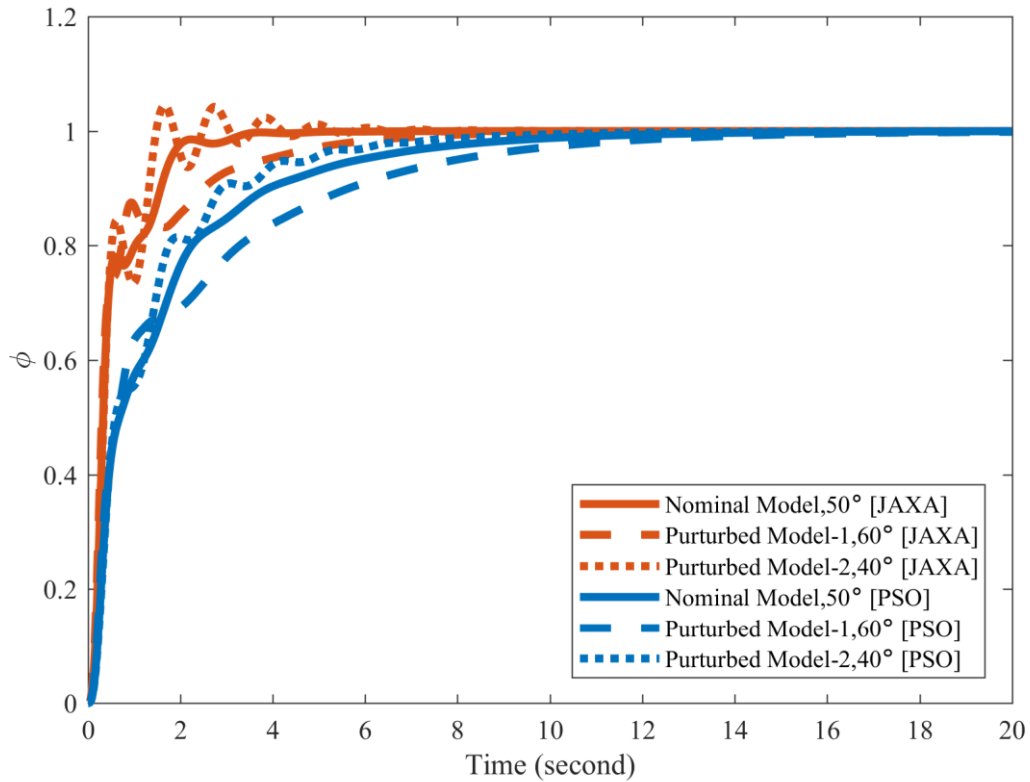


Fig. 7.36. Step responses of ϕ with CAS gains in 4.6), optimized gains in Table 4.2 (c) at $\tau_\omega = 50^\circ$ [lat. motion].

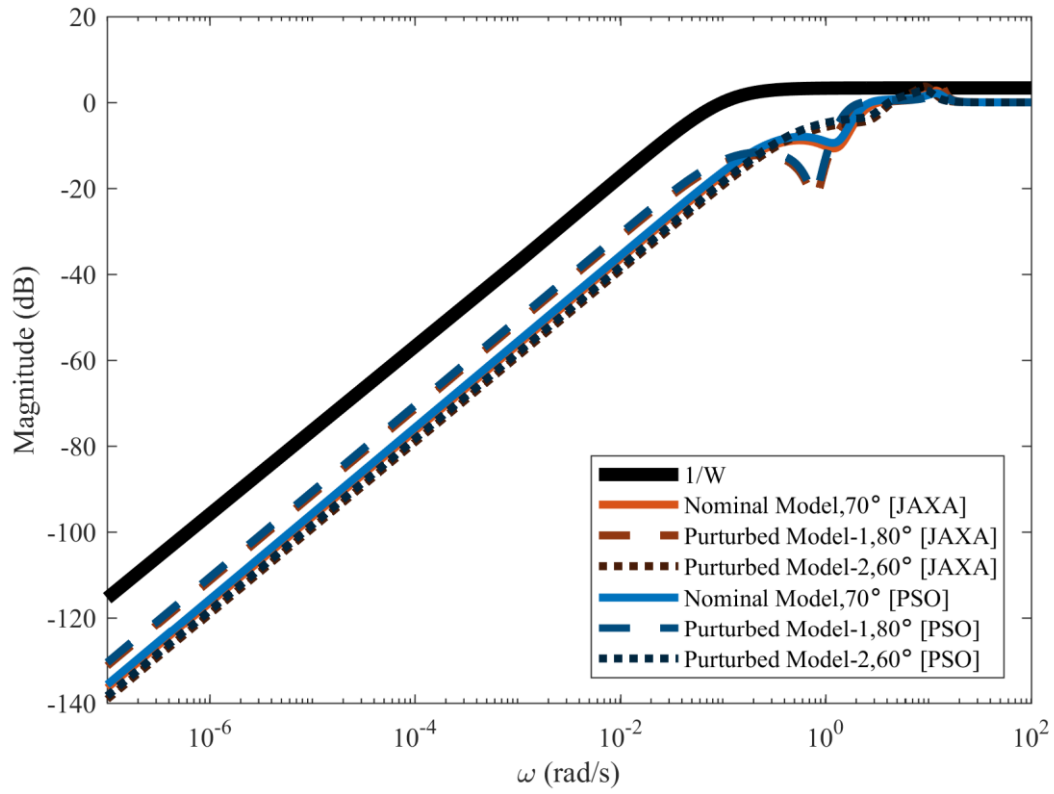


Fig. 7.37. Gain plots of sensitivity functions with CAS gains in 4.6), optimized gains in Table 4.2 (c) and $1/|W(s)|$ at $\tau_\omega = 70^\circ$ [lat. motion].

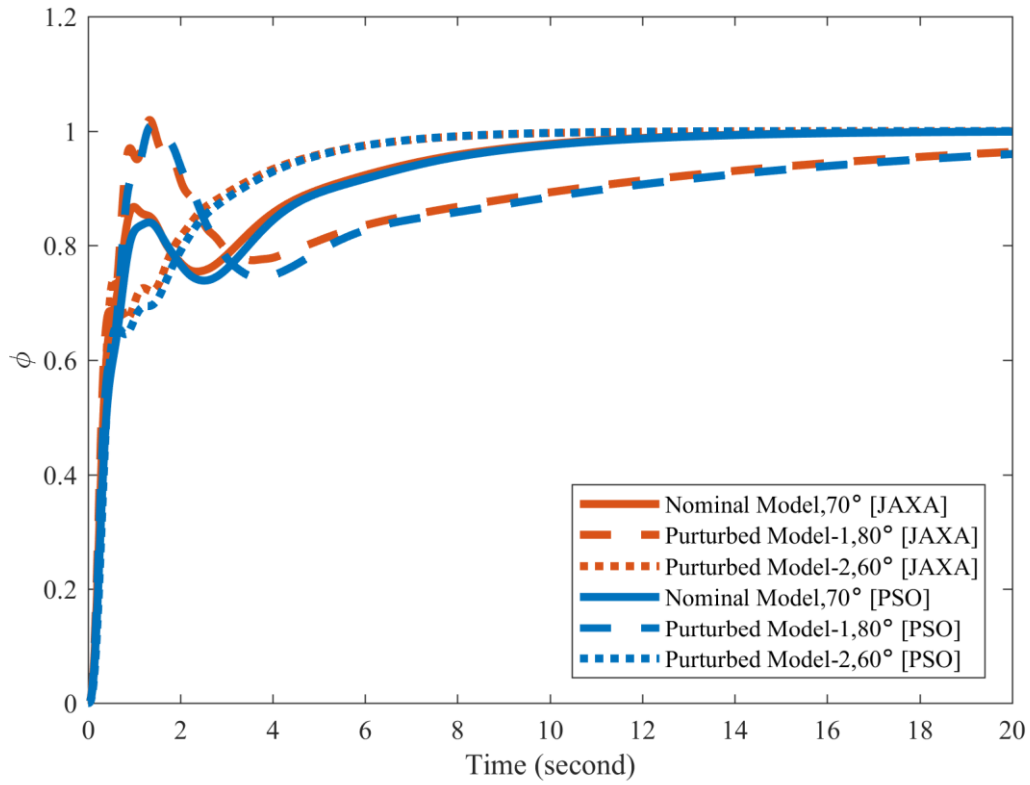


Fig. 7.38. Step responses of ϕ with CAS gains in 4.6), optimized gains in Table 4.2 (c) at $\tau_\omega = 70^\circ$ [lat. motion].

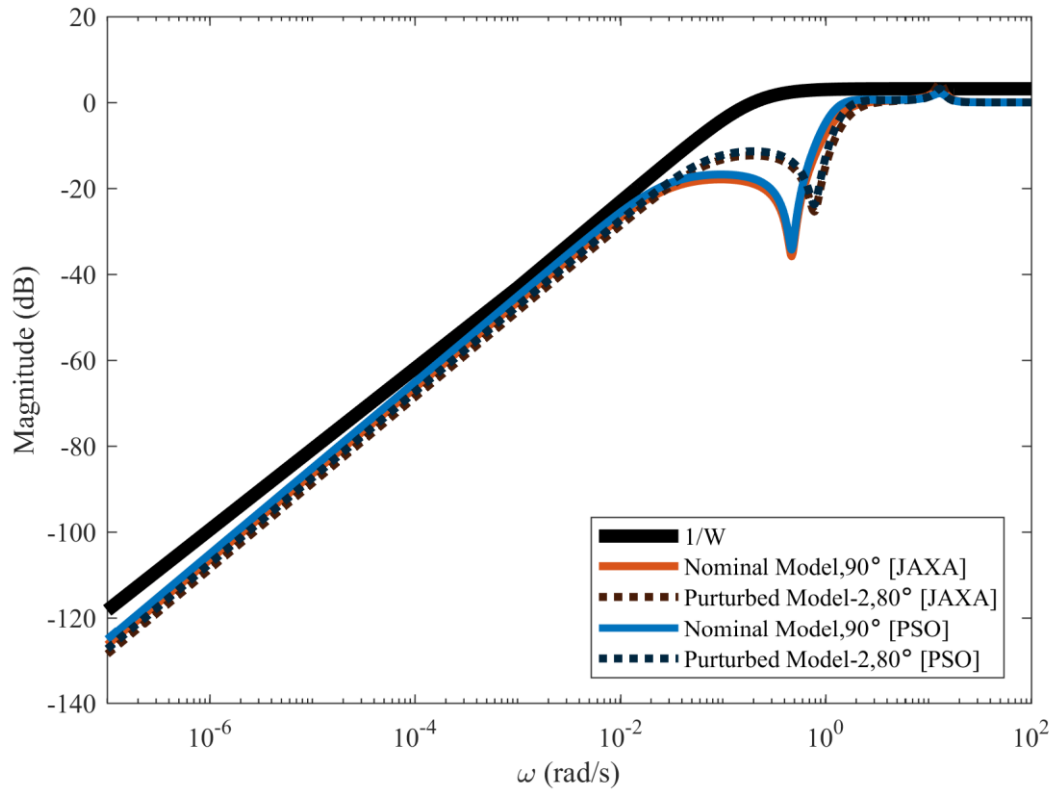


Fig. 7.39. Gain plots of sensitivity functions with CAS gains in 4.6), optimized gains in Table 4.2 (c) and $1/|W(s)|$ at $\tau_\omega = 90^\circ$ [lat. motion].

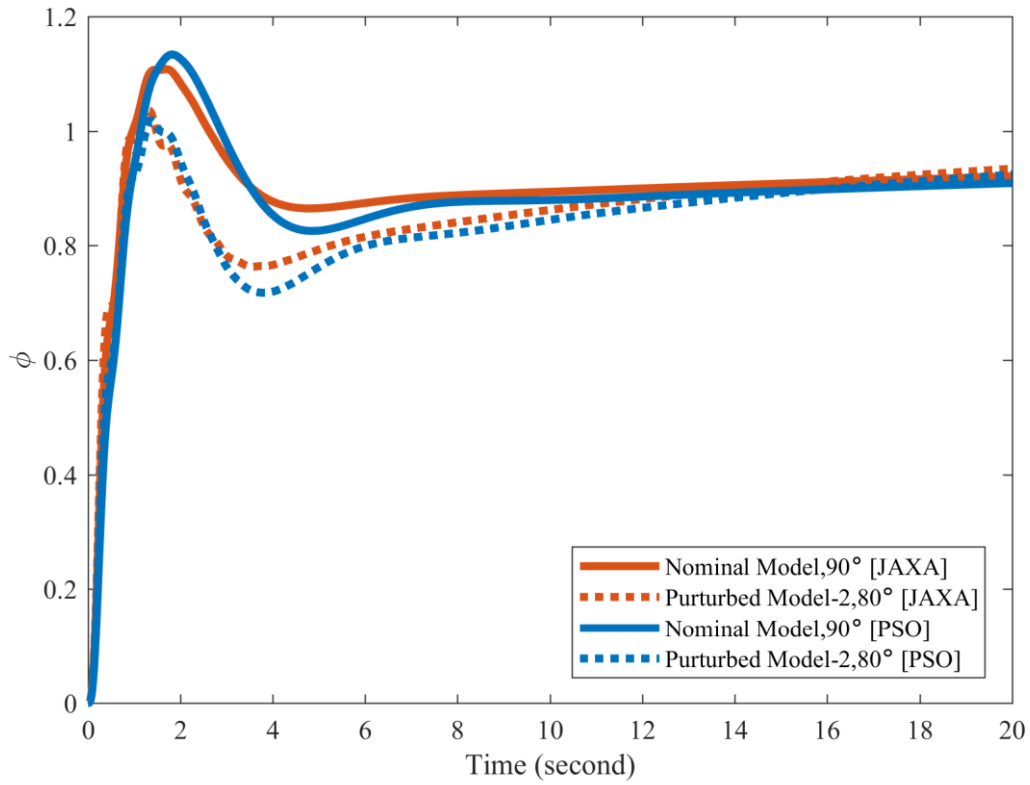


Fig. 7.90. Step responses of ϕ with CAS gains in 4.6), optimized gains in Table 4.2 (c) at $\tau_\omega = 90^\circ$ [lat. motion].